

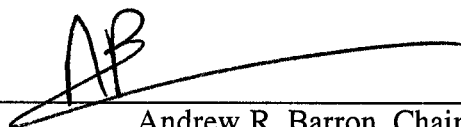
RICE UNIVERSITY

CHARACTERIZATION VIA NUCLEAR MAGNETIC RESONANCE
OF PORTLAND CEMENT AND RELATED MATERIALS

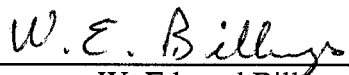
by
CHRISTOPHER LANE EDWARDS

A THESIS SUBMITTED
IN PARTIAL FULFILLMENT OF THE
REQUIREMENTS FOR THE DEGREE
DOCTOR OF PHILOSOPHY

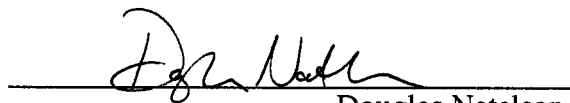
APPROVED, THESIS COMMITTEE



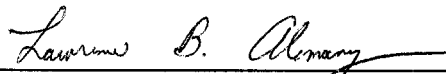
Andrew R. Barron, Chairman
Charles W. Duncan, Jr. – Welch Chair of Chemistry
Professor of Materials Science
and Associate Dean for Industry Interactions and Technology Transfer
Wiess School of Natural Sciences



W. Edward Billups,
Professor of Chemistry



Douglas Natelson,
Associate Professor of Physics and Astronomy
and Associate Professor of Electrical and Computer Engineering



Lawrence B. Alemany,
Senior Research Scientist, NMR Manager, Lecturer

Houston, Texas

May 2007

UMI Number: 3256684

INFORMATION TO USERS

The quality of this reproduction is dependent upon the quality of the copy submitted. Broken or indistinct print, colored or poor quality illustrations and photographs, print bleed-through, substandard margins, and improper alignment can adversely affect reproduction.

In the unlikely event that the author did not send a complete manuscript and there are missing pages, these will be noted. Also, if unauthorized copyright material had to be removed, a note will indicate the deletion.

UMI[®]

UMI Microform 3256684

Copyright 2007 by ProQuest Information and Learning Company.

All rights reserved. This microform edition is protected against unauthorized copying under Title 17, United States Code.

ProQuest Information and Learning Company
300 North Zeeb Road
P.O. Box 1346
Ann Arbor, MI 48106-1346

Abstract

Characterization via Nuclear Magnetic Resonance of Portland Cement and Related Materials

by

Christopher Lane Edwards

The physicochemical and engineering performance properties of several API class G and H ordinary Portland cements (OPCs) from various foreign and domestic sources have been investigated. The engineering performance properties are found to vary from sample to sample, and sources for this variation were sought out and identified. Magic angle spinning (MAS) ^{29}Si nuclear magnetic resonance (NMR) experiments were marked by unusual relaxation behavior due to paramagnetism inherent in OPCs. A model system was created to mimic the paramagnetism of the cements and the system's relaxation behavior was analyzed. The iron in the calcium aluminoferrite (C_4AF) provides the paramagnetism sufficient to substantially increase the relaxation rates of the ^{29}Si in the tricalcium silicate (C_3S) and dicalcium silicate (C_2S) of cement. Several relaxation techniques were evaluated for analyzing cement relaxation, and saturation recovery was identified as the preferred technique. Correlations of data from the saturation recovery experiments with engineering performance properties, especially the strength development of cement pastes, were obtained facily. An error analysis of the NMR and engineering performance testing techniques was conducted, which indicated that NMR measurements produced less error than the engineering performance tests. A best practice, modified from the saturation recovery experiment, is proposed for use in property correlations.

Additionally, ^{13}C MAS NMR was used to characterize various fluorinated single-walled carbon nanotubes (F-SWNTs), which proved surprisingly effective in attenuating

^{13}C - ^{19}F dipolar interactions and quantifying the extent of functionalization present at high degrees of reaction.

The mixed-metal nanocluster known as FeMoC was also characterized by MAS NMR. The impact of the paramagnetic Fe^{3+} in the Keplerate cage on the ^{31}P nuclei in the caged Keggin ion of FeMoC was evident in the greatly reduced relaxation times measured.

Acknowledgements

At this point I would like to thank everyone who assisted and supported me in the preparation of this research.

First and foremost I would like to thank Andy Barron for his support, tutelage, and forbearance over the years I have worked under and with him. Much of what I have learned about science and the scientific world I owe to him, and I am eternally grateful.

Secondly, I'd like to thank the other faculty, staff and students at Rice who have provided support, both intellectual and emotional, during my years of graduate study: Ed Billups, Doug Natelson, Larry Alemany, Bob Hauge, the Late John Margrave, Mary McHale, Virginia Wairegi, and all the Barron Group members from 1999 to the present.

Next, I wish to thank Halliburton Energy Services for funding this work and the many people there who have helped me along the way. Lewis Norman, Ian Robb, Ronnie Morgan, Gary Funkhouser, Rickey Morgan (no relation), Bill Caveny, Dennis Gray, and many others have been instrumental in this achievement.

Finally, I'd like to thank all my family and friends for their constant, heartfelt, and unconditional support and love during this time, especially my parents Lane and Elizabeth, my sister Abby, my best friend Vinh, and my high school science teachers Shannon Evans, Toni Baker, and Louis Mascolo, who first showed me that the that my passion truly lay in the physical sciences.

Table of Contents

Introduction	1
Hydration chemistry of Portland cement	12
References	17
Chapter 1. Basic Considerations for NMR Analysis of Cements	
Introduction	19
Results and Discussion	
^{29}Si NMR of cements	21
^{29}Si NMR of model systems	23
Conclusions	26
Experimental	28
^{29}Si NMR spectroscopy	30
Preparation of $\text{M}(\text{acac})_3$ -coated silicates	30
References	31
Chapter 2. Comparison of Methods of NMR Relaxation Analysis	
Introduction	33
Results and Discussion	
Inversion recovery method	38
Saturation recovery method	40
Bloch decay experiment	50
Conclusions	50
Experimental	52
References	55

Chapter 3. Correlations of NMR Measurements with Cement Performance

Property Measurements

Introduction	56
Results and Discussion	57
Physical measurements	58
NMR measurements	61
Correlations for cement	61
Correlations for cement with retarder	76
Correlations with fluid loss additive	82
Conclusions	87
Experimental	87
References	88

Chapter 4. Error Analysis of Analytical Methods

Introduction	90
Discussion	91
Proposed best practice	95
Conclusions	97
References	97

Chapter 5. Solid State ^{13}C NMR of F-SWNTs

Introduction	98
Results and Discussion	99
Thermal decomposition of F-SWNTs	108
NMR versus Raman for functional group quantification	110

Conclusions	112
Experimental	113
References	113

Chapter 6. ^{31}P NMR Characterization of the Nanocluster



Introduction	119
Results and Discussion	120
Experimental	126
References	127

List of Figures

Introduction

- Figure I.1.** An oil well cementing schematic. Drilling mud is used to assist in the actual drilling. A steel casing runs the length of the hole. The cement is pumped down the steel casing. Displacement fluid follows the cement, pushing it up into the space between the earth and the casing. 2
- Figure I.2.** Limestone quarry face in Midlothian, TX (Halliburton Energy Services). 4
- Figure I.3.** Limestone quarry formation, showing the 45° ripping technique (Halliburton Energy Services). 4
- Figure I.4.** Mobile crusher and XRF unit (Halliburton Energy Services). 5
- Figure I.5.** Covered conveyor belt for limestone transport (Halliburton Energy Services). 5
- Figure I.6.** Exterior view of dome storage unit with conveyor loading port (Halliburton Energy Services). 6
- Figure I.7.** Interior view of dome storage unit, illustrating its radial piling (Halliburton Energy Services). 6
- Figure I.8.** Raking device for reclaiming stored limestone (Halliburton Energy Services). 7
- Figure I.9.** Buffer bin (Halliburton Energy Services). 7
- Figure I.10.** Coarse grinder (Halliburton Energy Services). 8
- Figure I.11.** Two views of wet rotary kiln, emphasizing its length and diameter (Halliburton Energy Services). 9
- Figure I.12.** Interior view of an operational wet kiln (Halliburton

Energy Services).	10
Figure I.13. Cross-section of a typical cement grain. Adapted from Cement Microscopy, Halliburton Services, Duncan, OK.	11
Figure I.14. Schematic representation of Tobermorite, viewed along a polysilicate chain. Silicate ions either share oxygen atoms with a central CaO_2 core or bridge silicate tetrahedra. Interlayer calcium ions and water molecules are omitted for clarity.	13
Figure I.15. Hydration of C_3S over time: (a) the preinduction period, (b) the induction, (c) period the acceleratory period, and (d) the deceleratory period.	14
Figure I.16. Ettringite columns (a) consisting of octahedral aluminum, tetrahedral oxygen, and 8-coordinate calcium. The coordination sphere of each calcium is filled by water and sulfate ions. The packing of the columns (b) represented by large circles, the smaller circles represent channels containing with water and sulfate ions.	16

Chapter 1

Figure 1.1. Standard Bloch decay spectrum of a Texas Lehigh cement.	22
Figure 1.2. Schematic representation of partially $\text{M}(\text{acac})_3$ -coated silicate.	24
Figure 1.3. ^{29}Si NMR of C_3S (a) with $\text{Fe}(\text{acac})_3$, (b) with $\text{Cr}(\text{acac})_3$, and (c) without paramagnetic material added.	24
Figure 1.4. ^{29}Si NMR of C_2S (a) with $\text{Fe}(\text{acac})_3$, (b) with $\text{Cr}(\text{acac})_3$, and (c) without paramagnetic material added.	25

Figure 1.5. ^{29}Si NMR of fumed silica (a) with $\text{Fe}(\text{acac})_3$, (b) with $\text{Cr}(\text{acac})_3$, and (c) without paramagnetic material added.	26
Figure 1.6. Inversion recovery spectrum of C_3S (a) with $\text{Fe}(\text{acac})_3$, (b) with $\text{Cr}(\text{acac})_3$, and (c) without paramagnetic material added.	27
Figure 1.7. Inversion recovery spectrum of C_2S (a) with $\text{Fe}(\text{acac})_3$, (b) with $\text{Cr}(\text{acac})_3$, and (c) without paramagnetic material added.	28
Figure 1.8. Inversion recovery spectrum of fumed silica (a) with $\text{Fe}(\text{acac})_3$, (b) with $\text{Cr}(\text{acac})_3$, and (c) without paramagnetic material added.	29

Chapter 2

Figure 2.1. Left: portion of particle studied by X-ray fluorescence and X-ray diffraction. Right: portions of cement potentially evaluated by NMR relaxation analysis.	33
Figure 2.2. Schematic diagram of the inversion recovery experiment.	35
Figure 2.3. Graphical representation of the impact of the variable mixing period (τ) on the intensity of a given peak in an inversion recovery experiment for a typical diamagnetic, homogeneous material.	36
Figure 2.4. Graphical representation of the impact of τ on the intensity of a given peak in a saturation recovery experiment for a typical diamagnetic, homogeneous material.	37
Figure 2.5. Inversion recovery spectrum of cement sample CAP.	39
Figure 2.6. Sub-spectrum of the inversion recovery data above illustrating the superposition of positive C_3S signal and negative C_2S signal.	39

- Figure 2.7.** Graphic representation of spectrum subtraction for estimation of C_3S and C_2S content. 40
- Figure 2.8.** Saturation recovery spectrum of cement sample CAP. 41
- Figure 2.9.** Sub-spectra of the saturation recovery data for sample CAP at τ of (a) 100 μs , (b) 300 μs , (c) 700 μs , (d) 1 ms, (e) 3 ms, (f) 7 ms, (g) 10 ms, (h) 30 ms, (i) 70 ms, (j) 100 ms, (k) 300 ms, (l) 1 s, and (m) 3 s, illustrating the superposition of the fitted peaks forming the C_3S and C_2S contributions resulting from deconvolution. 43
- Figure 2.10.** Sub-spectra of the saturation recovery data for sample CAP at τ of (a) 300 μs , (b) 700 μs , (c) 1 ms, (d) 3 ms, (e) 7 ms, (f), 10 ms, (g) 1 s, (h) 3 s, (i) 7 s, (j) 10 s, (k) 30 s, and (l) 70 s, illustrating the superposition of the fitted peaks forming the C_3S and C_2S contributions resulting from deconvolution. 46
- Figure 2.11.** Plot showing rescaled extreme τ data sets combined with the intermediate τ data. The three series are shape coded for short (■), medium (■), and long (■) τ data for C_3S and C_2S . 50
- Figure 2.12.** Derivative analysis of the C_3S component for the medium- τ regime of sample CAP. The three series are shape coded for the intensities of the base function (■), first derivative (■), and second derivative (■). 51
- Figure 2.13.** Derivative analysis of the C_2S component for the medium- τ regime of sample CAP. The three series are shape coded for the intensities of the base function (■), first derivative (■), and second derivative (■). 51
- Figure 2.14.** Variable delay Bloch decay spectrum of cement sample CAP. 52

Chapter 3

- Figure 3.1.** World map labeled with approximate locations of origin for cements studied. 58
- Figure 3.2.** Atmospheric consistometer (Halliburton Energy Services). 59
- Figure 3.3.** High temperature high pressure (HTHP) consistometer (Halliburton Energy Services). 60
- Figure 3.4.** Ultrasonic cement analyzer (UCA) (Halliburton Energy Services). 60
- Figure 3.5.** Plot of time for strength development (min.) as a function of C_3S/C_2S ratio as determined from MAS ^{29}Si NMR for 50 psi (■, $R = 0.878$) and 500 psi (□, $R = 0.673$). 72
- Figure 3.6.** Plot of time for strength development (min.) as a function of (a) C_3S and (b) C_2S ($R = 0.603$) peak intensity as determined from MAS ^{29}Si NMR for 50 psi. 73
- Figure 3.7.** Plot of compressive strength (psi) development as a function of C_3S/C_2S ratio as determined from MAS ^{29}Si NMR at 24 h (■, $R = 0.837$), 48 h (□, $R = 0.734$), and 72 h (●, $R = 0.743$). 74
- Figure 3.8.** Plot of time for 72 hour crush strength (psi) as a function of C_3S/C_2S ratio as determined from MAS ^{29}Si NMR ($R = 0.445$). 74
- Figure 3.9.** Plot of time for 72 hour crush strength (psi) as a function of C_3S peak intensity as determined from MAS ^{29}Si NMR ($R = 0.532$). 75
- Figure 3.10.** Plot of time for 72 hour crush strength (psi) as a function of C_3S characteristic relaxation time as determined from MAS ^{29}Si NMR ($R = 0.714$). 75

Figure 3.11. Plot of Young's modulus (psi) as a function of C_3S characteristic relaxation time as determined from MAS ^{29}Si NMR ($R = 0.621$).

76

Figure 3.12. Plot of time for strength development (min.) in the presence of 0.5% lignosulfonate retarder bwoc as a function of C_3S/C_2S ratio as determined from MAS ^{29}Si NMR for 50 psi (\blacksquare , $R = 0.697$) and 500 psi (\square , $R = 0.743$).

80

Figure 3.13. Plot of time for strength development (min.) in the presence of 0.5% lignosulfonate retarder bwoc as a function of C_3S characteristic relaxation time as determined from MAS ^{29}Si NMR for 50 psi (\blacksquare , $R = 0.524$) and 500 psi (\square , $R = 0.592$).

80

Figure 3.14. Plot of compressive strength development (psi) in the presence of 0.5% lignosulfonate retarder bwoc as a function of C_3S/C_2S ratio as determined from MAS ^{29}Si NMR at 24 h (\blacksquare , $R = 0.501$), 48 h (\square , $R = 0.436$), and 72 h (\bullet , $R = 0.667$).

81

Figure 3.15. Plot of time for 72-hour crush strength (psi) in the presence of 0.5% lignosulfonate retarder bwoc as a function of C_3S/C_2S ratio as determined from MAS ^{29}Si NMR.

81

Figure 3.16. Plot of thickening time (min.) in the presence of 0.5% fluid loss additive bwoc as a function of C_3S characteristic relaxation time for as determined from MAS ^{29}Si NMR for 50 Bc (\circ , $R = 0.507$), 70 Bc (\blacksquare , $R = 0.476$), and 100 Bc ($+$, $R = 0.484$).

86

Figure 3.17. Plot of time for strength development (min.) in the presence of 0.15 % fluid loss additive bwoc as a function of C_3S/C_2S ratio as determined from MAS ^{29}Si NMR for 50 psi (\blacksquare , $R = 0.740$) and 500 psi (\square , $R = 0.696$).

86

Figure 3.18. Plot of time for compressive strength (psi) in the presence of 0.15% fluid loss additive bwoc as a function of C_3S/C_2S ratio as determined from MAS ^{29}Si NMR for 24 h (■, $R = 0.505$), 48 h (□, $R = 0.381$), and 72 h (●, $R = 0.378$).

87

Chapter 4

Figure 4.1. Plot of “active” C_3S/C_2S ratio (as determined by MAS ^{29}Si NMR) versus “classical” C_3S/C_2S ratio (as determined by XRF).

89

Figure 4.2. Plot of time to 50 psi (min.) versus C_3S/C_2S ratio from NMR (×) and C_3S/C_2S ratio from XRF (○).

93

Figure 4.3. Plot of time for strength development (min.) in the presence of 0.5% lignosulfonate retarder bwoc as a function of C_3S/C_2S ratio as determined from MAS ^{29}Si NMR for 50 psi ($R = 0.697$) showing the anomalously large value for the JOP sample.

93

Figure 4.4. Conceptual plot of error in measurement of a given performance property via both NMR and direct physical strength/consistometry measurements.

94

Chapter 5

Figure 5.1. ^{13}C MAS NMR spectrum of F-SWNTs obtained at 50.3 MHz ^{13}C (4.7 T) and 15 kHz spinning.

100

Figure 5.2. ^{13}C MAS NMR spectra of F-SWNTs obtained at 50.3 MHz ^{13}C with a 4mm OD rotor (left, 56.9 mg) and at 125.8 MHz ^{13}C with a 2.5mm OD rotor (right, 5.4 mg) at the spinning speeds indicated (in kHz).

104

Figure 5.3. Calculated ^{13}C NMR shifts for (a) $\text{C}_{80}\text{H}_{20}$ fragment of the 5,5 (armchair) conformation, and as a result of (b) 1,2-addition by 2 fluorine atoms, (c) 1,4-addition by 2 fluorine atoms, (d) 1,2-addition by 4 fluorine atoms, and (e) 1,4-addition by 4 fluorine atoms. 106

Figure 5.4. ^{13}C MAS NMR spectra of F-SWNTs obtained at 50.3 MHz ^{13}C (a) as prepared at 150 °C (parameters as in Figure 5.1), after heating to (b) 400, (c) 450, and (d) 550 °C, with 11 kHz MAS used for the heated samples. 109

Figure 5.5. Plot of $\text{C}(\text{sp}^2):\text{C-F}(\text{sp}^3)$ ratio (■) and Raman G-band:D-band ratio (▣) as a function of the C:F ratio from XPS. 112

Chapter 6

Figure 6.1. Computer representation of FeMoC based upon single crystal data showing the ‘cluster-within-a-cage’ structure. 120

Figure 6.2. ^{31}P NMR spectra of (a) $\text{H}_3[\text{P}(\text{Mo}_3\text{O}_{10})_4]$ and (b) FeMoC-EtOH. 123

Figure 6.3. Pseudo-2D inversion recovery data set for ^{31}P NMR of FeMoC-EtOH. 124

Figure 6.4. The height of the center band ($\delta = -5.5$ ppm) for the ^{31}P NMR spectrum of FeMoC-EtOH versus τ ($T_1 = 35$ ms). 124

Figure 6.5. Pseudo 2D CPMG data set (T_2 isolation by spin echo) for FeMoC-EtOH. 125

Figure 6.6. The height of the center band ($\delta = -5.5$ ppm) for the ^{31}P NMR spectrum of FeMoC-EtOH versus τ ($T_2 = 8$ ms). 125

List of Tables

Chapter 1

Table 1.1. Comparison of NMR-active isotopes for common elements in cement.	20
Table 1.2. Inversion recovery measurements of T_1 (s) for C_3S , C_2S , and SiO_2 with and without $M(acac)_3$ ($M = Fe, Cr$).	29

Chapter 2

Table 2.1. Raw data from deconvolution of saturation recovery subspectrum CAP (3 s).	42
Table 2.2. Processed deconvolution data from CAP saturation recovery experiments.	49
Table 2.3. Summary of data analysis methodologies.	53

Chapter 3

Table 3.1. Processed deconvolution data from TXI saturation recovery experiments.	62
Table 3.2. Processed deconvolution data from THA saturation recovery experiments.	63
Table 3.3. Processed deconvolution data from SDN saturation recovery experiments.	64
Table 3.4. Processed deconvolution data from RUS saturation recovery experiments.	65
Table 3.5. Processed deconvolution data from JOP saturation recovery experiments.	66

Table 3.6. Processed deconvolution data from ELT saturation recovery experiments.	67
Table 3.7. Processed deconvolution data from BRZ saturation recovery experiments.	68
Table 3.8. Characteristic relaxation times from derivative analysis.	69
Table 3.9. Consistometry data for cements without additives.	70
Table 3.10. Ultrasonic data for cements without additives.	71
Table 3.11. Destructive mechanical testing data for cements without additives.	72
Table 3.12. Consistometry data for cements with retarder.	77
Table 3.13. Ultrasonic data for cements with retarder.	78
Table 3.14. Destructive mechanical testing data for cements with retarder.	79
Table 3.15. Consistometry data for cements with fluid loss additive.	83
Table 3.16. Ultrasonic data for cements with fluid loss additive.	84
Table 3.17. Destructive mechanical testing data for cements with fluid loss additive.	85

Chapter 5

Table 5.1. Analysis of F-SWNTs as a function of thermolysis temperature.	108
---	-----

Chapter 6

Table 6.1. XPS elemental ratio analysis for the products from FeMoC synthesis.	122
---	-----

Introduction: An Overview of Cement Production

Portland Cement (or simply “cement” in the remainder of this work) is the single most commonly used building material in the world today. The manufacture of cement in the United States was in 2002 a 103.8 million metric ton, \$8.6 billion industry.¹ The origins of cement date back to well over 5000 years ago when the Egyptians developed mortars composed of lime (CaO) and gypsum ($\text{CaSO}_4 \cdot 2\text{H}_2\text{O}$) to hold together the enormous stone blocks of the pyramids.² Three thousand years later, between 300 BC and 476 AD, the Romans developed the first durable concrete, with a cementitious matrix of lime and volcanic ash (chiefly SiO_2) from Mount Vesuvius (the first pozzolanic material of known use³), and used it to build the Coliseum and the huge Basilica of Constantine.⁴

The use of natural cement, consisting of mixtures of lime and clay (aluminum silicates), emerged in England in the late 18th century. Joseph Aspdin obtained the first patent on cement manufacture in 1824.⁵ Aspdin carefully proportioned amounts of lime and clay, then pulverized the mixture and burned it in a furnace. He named his mixture Portland Cement, because the color of the powder resembled the color of the rock quarries on the Isle of Portland. The United States began producing its own Portland Cement in the 1870's. Technological developments such as the rotary kiln enhanced production capabilities and allowed cement to become one of the most widely used construction materials.

Cement production may be classified by application into two primary groups: construction and energy services. The construction applications for cementing consume the lion's share of cement manufactured world-wide, but the cement produced for energy services applications is an integral part of meeting the world's energy needs and requires tighter quality control standards to meet that industry's higher demands on control of the rheological properties of the fluid slurry state, the solid state, and especially the transition

from the former state to the latter, or the setting process. Applications relating to the energy services industry are the primary focus of this work. Additionally, cement may also become central to efforts in nuclear waste management by locking radioactive material within the cementitious matrix, where rates of diffusion of waste out of the cement serve as the dominant concern.⁶

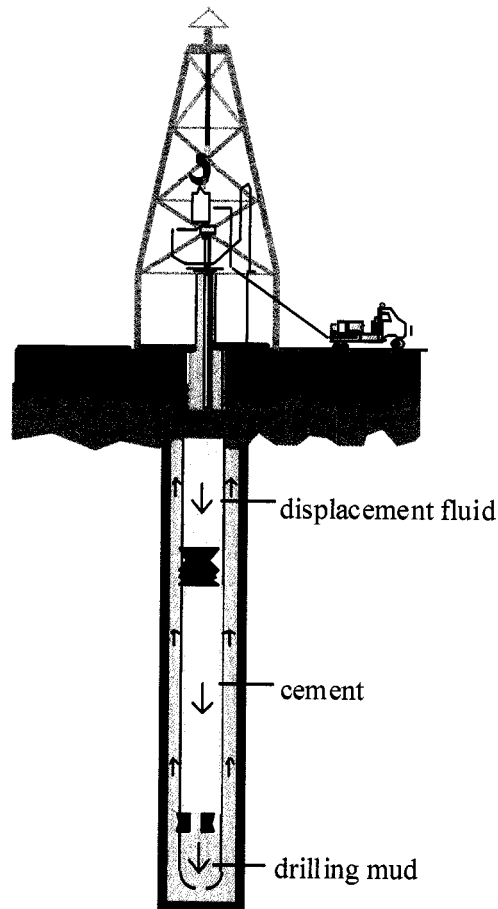


Figure I.1. A schematic of the oil well cementing process. A steel casing runs the length of the hole. The cement is pumped down the steel casing. Displacement fluid follows the cement, pushing it up into the space between the earth and the casing.

Portland Cement was first used in the energy services industry in 1903 to isolate the oil-containing region of the earth from downhole water, a process modernly referred to as zonal isolation.⁷ The technique of oil well cementing was soon developed (Figure I.1).⁸ After the primary hole is drilled, a steel casing, through which the oil will later flow, is placed inside. The cement is pumped down the steel casing to the bottom of the well

and then back up through the free annular space between the casing and the well, where it serves to bond the casing to the rock formation and to prevent fluids from moving from one formation to another (hence the term zonal isolation). Displacement fluids, such as fresh water, sea water, and weak acid solutions, are used to push the cement out of the casing. To avoid damage to the pumping equipment used to place the cement slurry, the cement must remain a fluid state for several hours while it is pumped into place; to avoid wasting valuable rig time, which can cost up to \$200,000 per day on some offshore rigs,⁹ the cement should set shortly after being placed.

In order to gain a greater understanding of the causes of variability in cements from plant to plant, or even from batch to batch, it is instructive to consider the manufacturing process and its inherent sources of variability. To this end, one may consider an actual cement plant and its manufacturing operations as an exemplar.

TXI's Midlothian, Texas cement plant produces various grades of cement by two processes, referred to as either the wet or dry process. The dry process uses a pneumatic kiln system which uses superheated air to convert raw materials to cement, whereas the wet process slurries the raw materials in water in preparation for conversion to cement. The dry process is generally favored by cement manufacturers due to its higher energy efficiency, but the wet process tends to produce cement with properties more palatable to the energy services industry. The American Petroleum Institute (API) Class H cement used in energy service applications is produced by the wet process, and thus will be the focus of the following discussion.

The cement manufacturing process begins at the quarry (Figure I.2), where limestone formations are ripped and crushed in two crushers to a mean particle size of 4 inches. The quarry formation is not entirely limestone, and no attempt is made to isolate the limestone from the other minerals. On the contrary, the rippers act to blend in the "impurity" minerals as evenly as is feasible while still maintaining an acceptable limestone content so as not to "waste" the formation. This is accomplished by ripping the

formation face at a 45 degree angle (Figure I.3). The rock is quality controlled via mobile X-ray fluorescence (XRF) spectroscopy (Figure I.4) at the starting point of a mobile covered conveyor belt system (Figure I.5), which transports the material to a dome storage unit (Figure I.6).

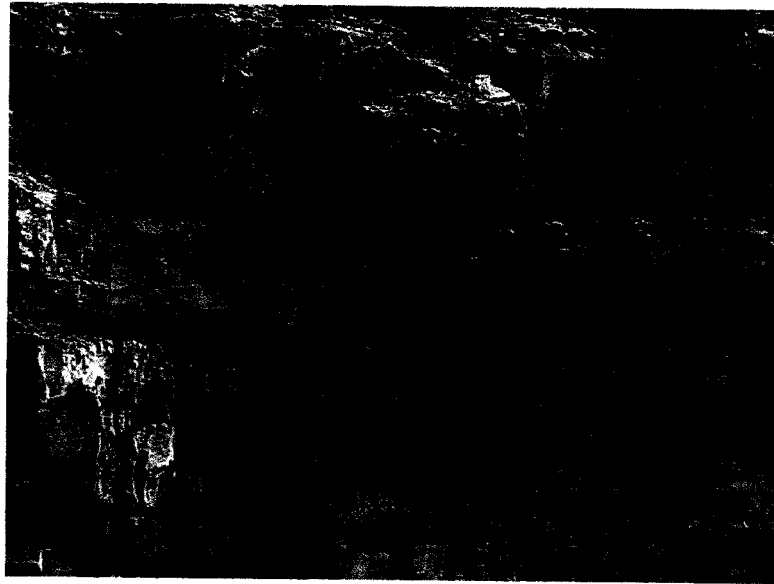


Figure I.2. Limestone quarry face in Midlothian, TX (Halliburton Energy Services).



Figure I.3. Limestone quarry formation, showing the 45° ripping technique (Halliburton Energy Services).

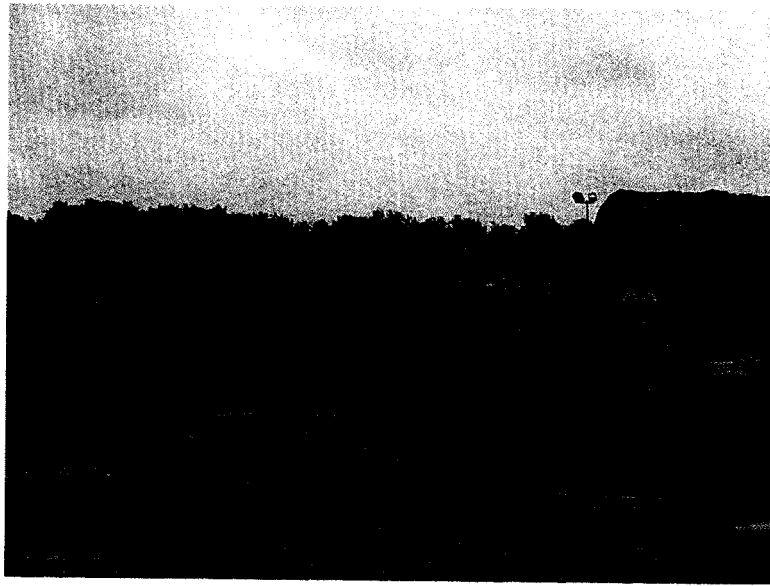


Figure I.4. Mobile crusher and XRF unit (Halliburton Energy Services).

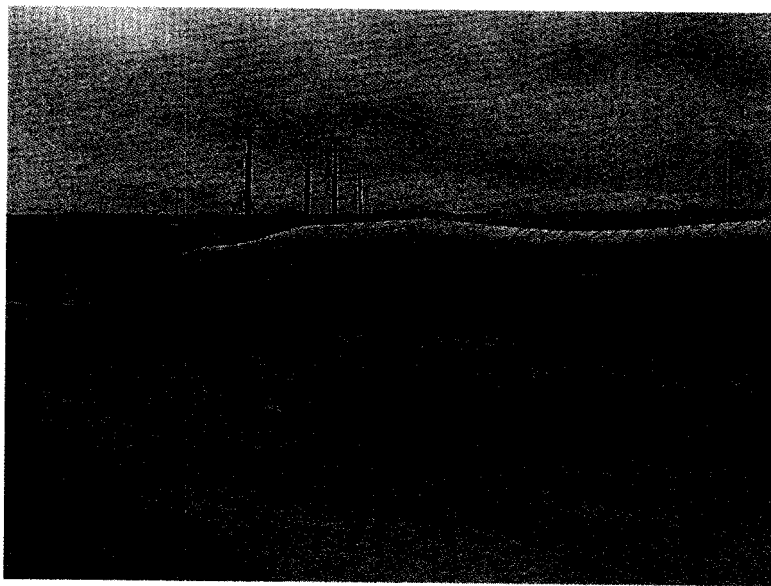


Figure I.5. Covered conveyor belt for limestone transport (Halliburton Energy Services).

The dome storage unit has a capacity of 60 kilotons, and is filled by dispensing the rock from the conveyor at the top of the dome into a pile built in a circular pattern (Figure I.7). The rock is reclaimed from storage *via* a raking device (Figure I.8) that grates over the pile at the natural angle of material slide. The raked material slides to the

base of the raking unit, where a second conveyor system transfers material to either of two limestone buffer bins (Figure I.9), each of which is dedicated to a particular kiln process. There is an additional buffer bin for mill scale from a nearby steel plant, as well

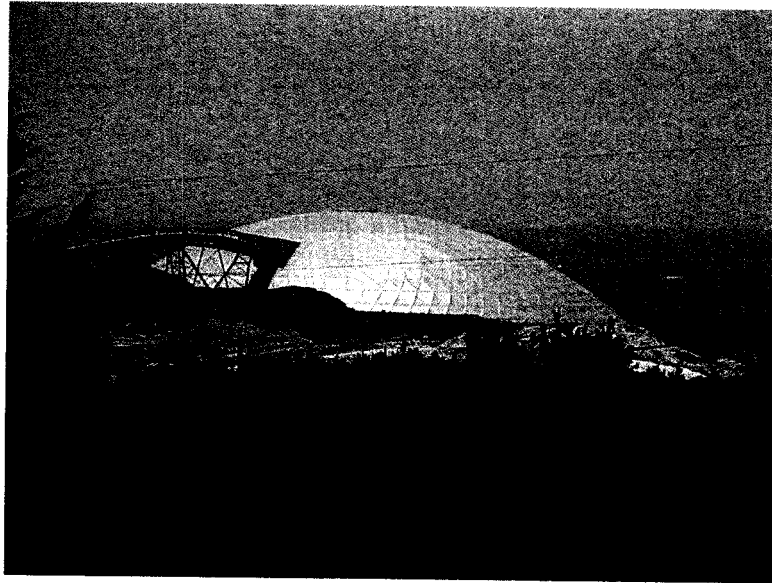


Figure I.6. Exterior view of dome storage unit with conveyor loading port (Halliburton Energy Services).

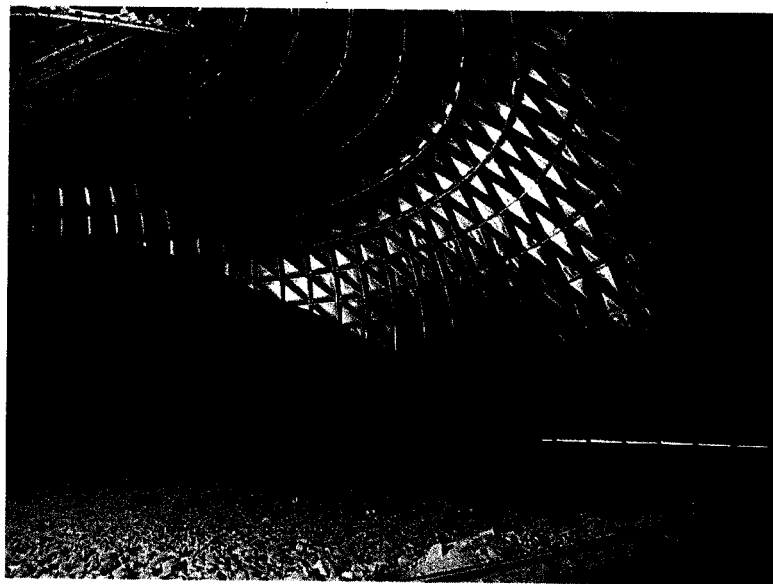


Figure I.7. Interior view of dome storage unit, illustrating its radial piling (Halliburton Energy Services).

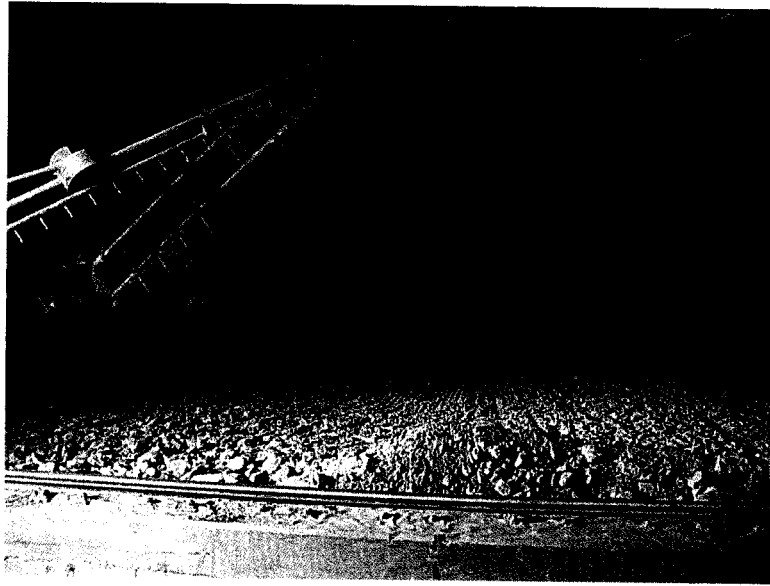


Figure I.8. Raking device for reclaiming stored limestone (Halliburton Energy Services).

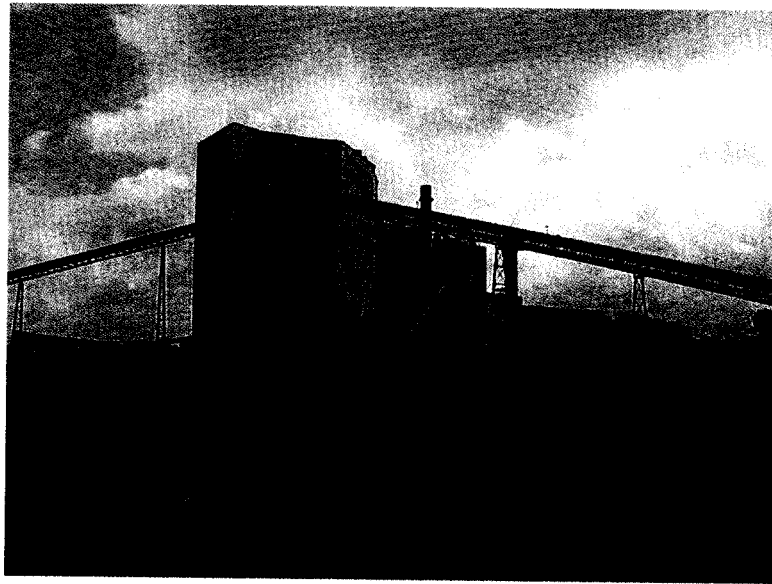


Figure I.9. Buffer bin (Halliburton Energy Services).

as a buffer bin for sand. It is worth noting at this point that the mill scale from the steel plant contains significant levels of boron, which acts as an innate retarder and seems to affect adversely, though not overly severely, the early compressive strength development when compared to cement from other plants.

Material leaving the buffer bins is monitored for elemental composition *via* XRF and feed rates are adjusted for maintaining proper flow of calcium, silicon, aluminum, and iron. The raw materials are carried to ball mills (Figures I.10) for grinding to fine powder, which is then mixed with water. The resulting slurry is then sent to the rotary kiln for burning, or transformation into cement clinker.

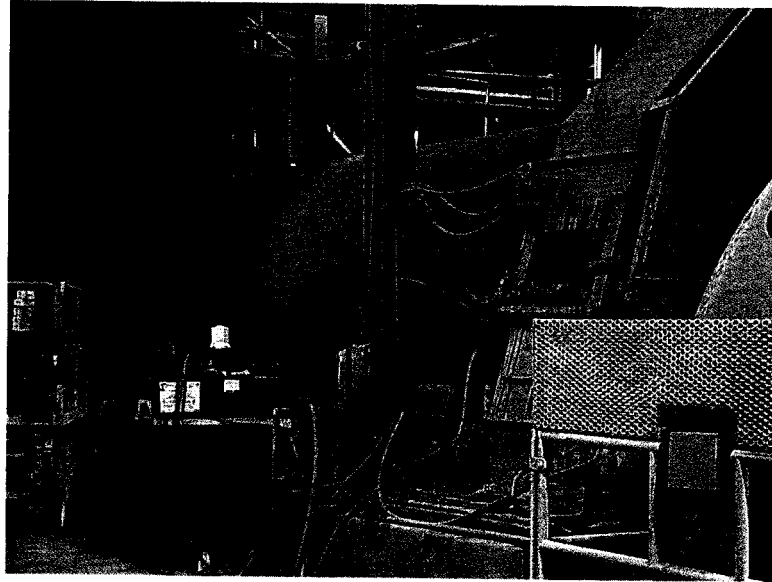


Figure I.10. Coarse grinder (Halliburton Energy Services).

TXI has four 450-foot long, twelve-foot diameter wet rotary kilns (Figures I.11), though no more than two are in operation at a given time. The kilns are fired to an internal material temperature of 2700 °F (Figure I.12) with a fuel of finely ground coal, natural gas, and/or various waste materials. Around fifty percent of the energy expenditure in the wet kiln process is dedicated to evaporating the water from the slurry, in contrast to the dry process, which spends most of its energy on the calcining process. Since the dry process only requires approximately half the energy of the wet process, it is generally more attractive to cement manufacturers. Unfortunately, the dry process in current use produces poor API Class H cement. A fuller understanding of the differences

in cement synthesis via the two processes could lead to the development of a more effective dry synthesis of Class H cements, but that is beyond the scope of this work.

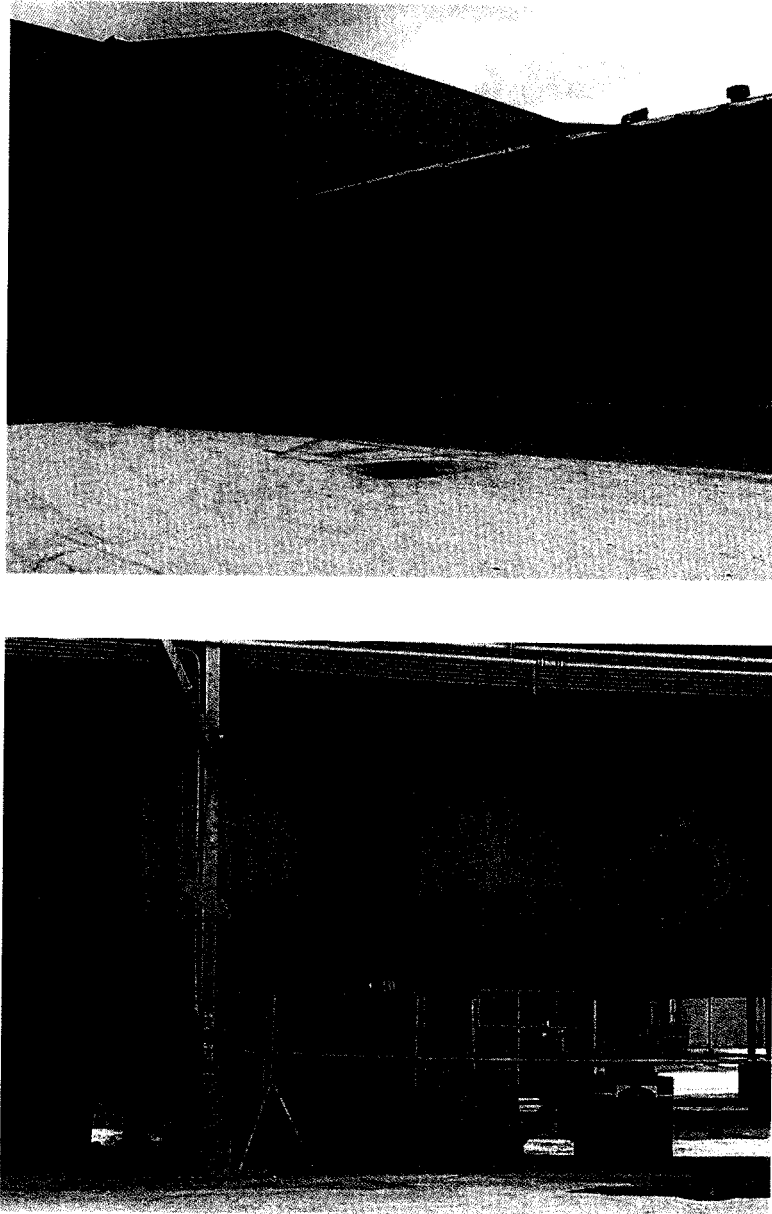


Figure I.11. Two views of wet rotary kiln, emphasizing its (a) length and (b) diameter (Halliburton Energy Services).

After the clinker leaves the kiln, it enters a cooler that uses pressurized air to cool the clinker. The energy absorbed by the air in the cooler serves to pre-heat the air for feed

into the kiln. The cooled clinker is then taken to storage to await final grinding with approximately five percent gypsum by weight. After grinding to the specified fineness, the final cement powder is pneumatically transferred to storage silos until it is shipped to the customer.

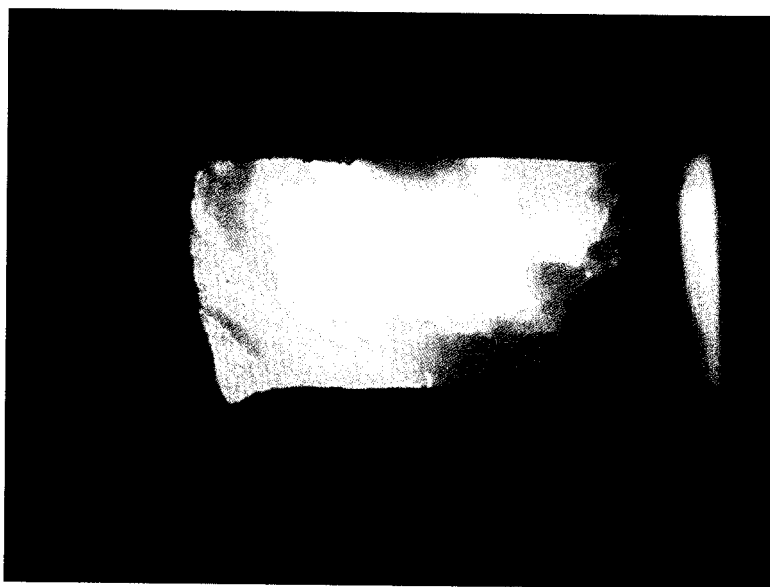


Figure I.12. Interior view of an operational wet kiln (Halliburton Energy Services).

Quality control of the clinker and final powder is handled via an automated X-ray diffraction/X-ray fluorescence (XRD/XRF) system, simple wet chemical analyses, simple optical microscopy, and periodic performance tests, including compressive strength and thickening time.

This entire process results in the heterogeneous nanocomposite of calcium silicate and aluminate particles, among other materials, which make up a typical cement grain. There are four chief minerals present in a cement grain: tricalcium silicate (C_3S),¹⁰ dicalcium silicate (C_2S), tricalcium aluminate (C_3A) and calcium aluminoferrite (C_4AF), which is more accurately considered a solid solution of dicalcium aluminate (C_2A) and dicalcium ferrite (C_2F).¹¹ The calcium aluminoferrite forms a continuous phase around the other mineral crystallites, as the iron containing species act as a fluxing agent in the

rotary kiln and are the last to solidify around the others. Figure I.13 shows a typical cement grain.

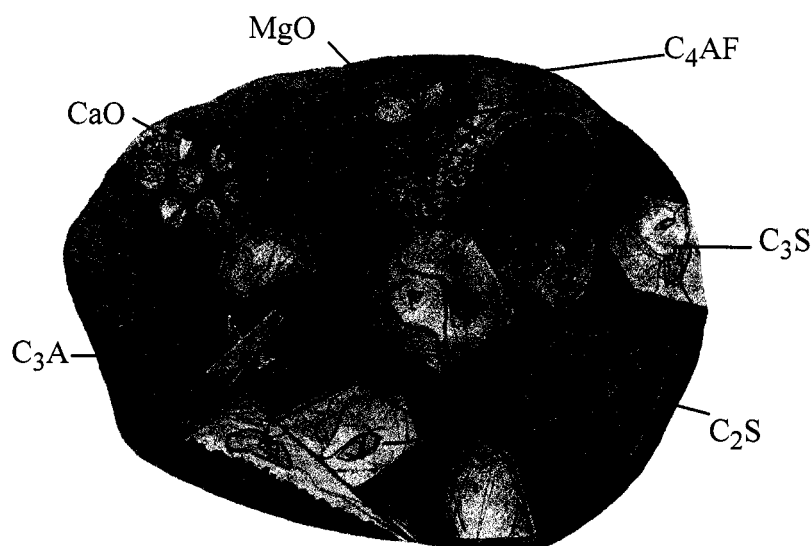


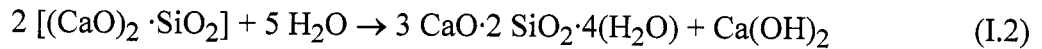
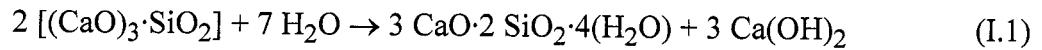
Figure I.13. Cross-section of a typical cement grain. Adapted from *Cement Microscopy*, Halliburton Services, Duncan, OK.

The composition of cement is varied depending on the application. The ratio of C_3S to C_2S helps to determine how fast the cement will set, with faster setting occurring with higher C_3S contents.¹¹ Lower C_3A content promotes resistance to sulfates.⁷ Higher amounts of ferrite lead to slower hydration. The ferrite phase causes the brownish gray color in cements, so that “white cements” (i.e., those that are low in C_4AF) are often used for aesthetic purposes. A typical example of cement contains 50–70% C_3S , 15–30% C_2S , 5–10% C_3A , 5–15% C_4AF , and 3–8% other additives. It is the hydration of these minerals that causes the hardening, or setting, of cement.

It is worth noting that a given cement grain will not have the same size or even necessarily contain all the same minerals as the next grain. The heterogeneity exists not only within a given particle, but extends from grain to grain, batch to batch, plant to plant. Developing a means of even partially characterizing as heterogeneous a material as this is the objective of this work.

Hydration chemistry of Portland cement. The addition of water to dry cement powder results in a thin cement slurry that can be easily manipulated and cast into different shapes. In time, the slurry sets and develops strength through a series of hydration reactions.¹¹ Hydration of cement is not linear through time, it proceeds very slowly at first, allowing the thin mixture to be properly placed before hardening. The chemical reactions that cause the delay in hardening are not completely understood, however they are critical to developing a rational methodology for the control of cement setting.

The tri- and di-calcium silicates (C_3S and C_2S , respectively) comprise over 80% by weight of most cements. It is known that C_3S is the most important phase in cement for strength development during the first month, while C_2S reacts much more slowly, and contributes to the long-term strength of the cement. Both the silicate phases react with water as shown below to form calcium hydroxide and a rigid calcium-silicate hydrate gel, C-S-H (Eq. I.1 and I.2).



The detailed structure of C-S-H is not completely known, however it is generally agreed upon that it consists of condensed silicate tetrahedra sharing oxygen atoms with a central, calcium hydroxide-like CaO_2 layer.¹² Taylor has proposed that the structure is most similar to either Tobermorite or Jennite, both of which share a skeletal silicate chain structure (Figure I.14).¹³

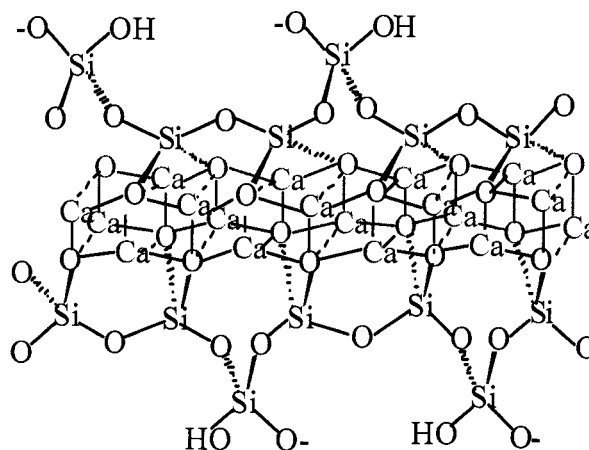


Figure I.14. Schematic representation of Tobermorite, viewed along a polysilicate chain. Silicate ions either share oxygen atoms with a central CaO_2 core or bridge silicate tetrahedra. Interlayer calcium ions and water molecules are omitted for clarity.

Although the precise mechanism of C_3S hydration is unclear, the kinetics of hydration is well known.¹⁴ The hydration of the calcium silicates proceeds *via* four distinct phases (Figure I.15). The first 15 - 20 minutes, termed the pre-induction period (Figure 1.15a), is marked by rapid heat evolution. During this period calcium and hydroxyl ions are released into the solution. The next, and perhaps most important, phase is the induction period (Figure 1.15b), which is characterized by very slow reactivity. During this phase, calcium oxide continues to dissolve producing a pH near 12.5. The chemical reactions that cause the induction period are not precisely known; however, it is clear that some form of an activation barrier must be overcome before hydration can continue. It has been suggested that in pure C_3S , the induction period may be the length of time it takes for C-S-H to begin nucleation, which may be linked to the amount of time required for calcium ions to become supersaturated in solution. Alternatively, the induction period may be caused by the development of a small amount of an impermeable calcium-silicon-hydrate (C-S-H) gel at the surface of the particles, which

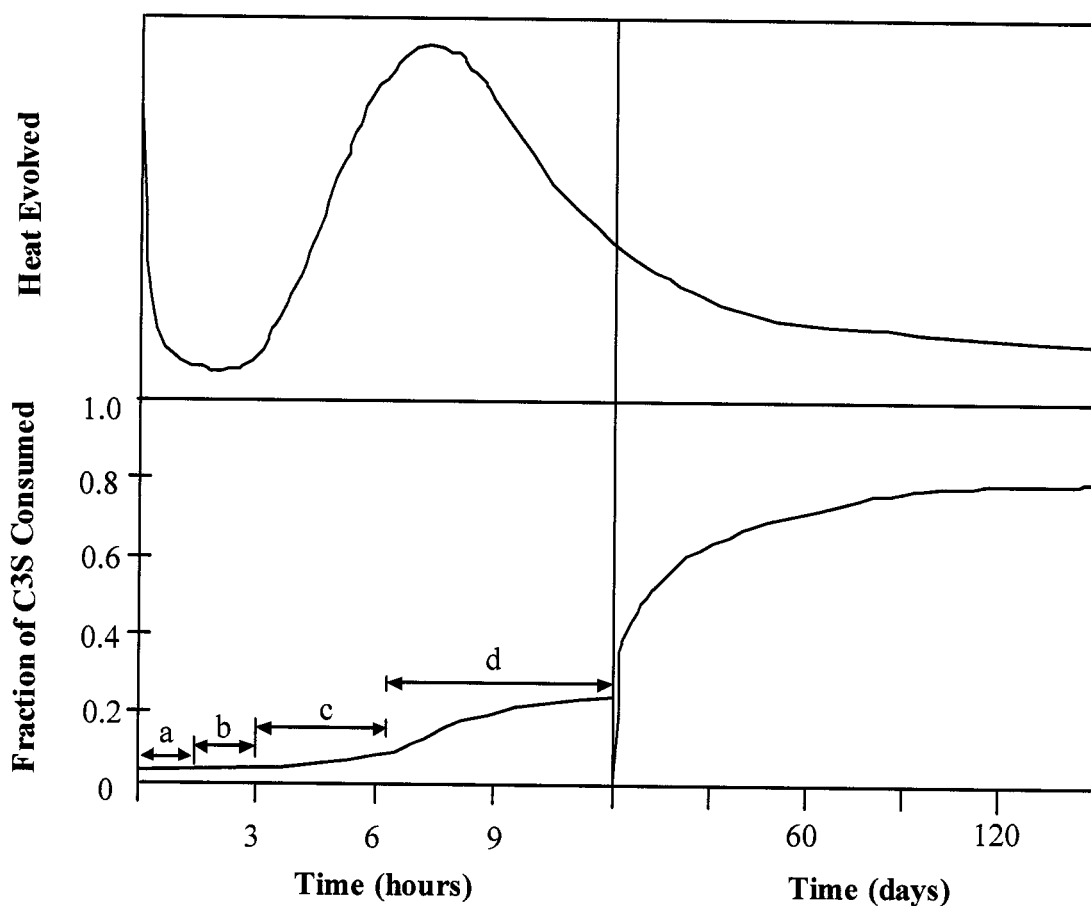


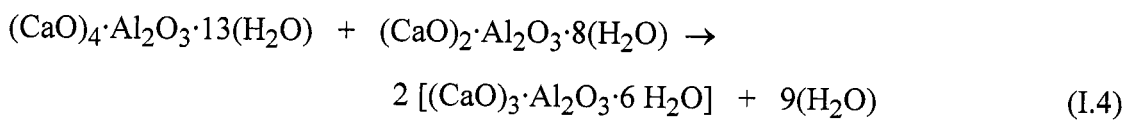
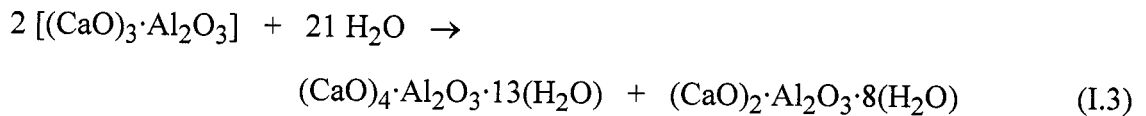
Figure I.15. Hydration of C3S over time: (a) the preinduction period, (b) the induction, (c) period the acceleratory period, and (d) the deceleratory period.

slows down the migration of water to the inorganic oxides. The initial Ca/Si ratio at the surface of the particles is near 3.¹⁵ As calcium ions dissolve out of this C-S-H gel, the Ca/Si ratio in the gel becomes 0.8-1.5. This change in Ca/Si ratio corresponds to a change in gel permeability, and may indicate an entirely new mechanism for C-S-H formation.¹⁶ As the initial C-S-H gel is transformed into the more permeable layer, hydration continues and the induction period gives way to the third phase of hydration, the acceleratory period (Figure I.15c).

After *ca.* 3 hours of hydration, the rate of C-S-H formation increases with the amount of C-S-H formed. Solidification of the paste, called setting, occurs near the end of the third period. The fourth stage (Figure I.15d) is the deceleratory period in which

hydration slowly continues hardening the solid cement until the reaction is complete. The rate of hydration in this phase is determined either by the slow migration of water through C-S-H to the inner, unhydrated regions of the particles, or by the migration of H^+ through the C-S-H to the anhydrous CaO and SiO_2 , and the migration of Ca^{2+} and Si^{4+} to the OH^- ions left in solution.

In spite of the fact that the aluminate and ferrite phases comprise less than 20% of the bulk of cement, their reactions are very important in cement and dramatically affect the hydration of the calcium silicate phases, see below. Relative to C_3S , the hydration of C_3A is very fast. In the absence of any additives, C_3A reacts with water to form two intermediate hexagonal phases, C_2AH_8 and C_4AH_{13} (Eq. I.3). The structure of C_2AH_8 is not precisely known, but structures containing $[Ca_2Al(OH)_6][Al(OH)_4] \cdot nH_2O$ or $[Ca_2Al(OH)_6][Al(OH)_3(H_2O)_3]OH$ have been proposed. C_4AH_{13} has a layered structure based on the calcium hydroxide structure, in which one out of every three Ca^{2+} is replaced by an Al^{3+} or Fe^{3+} with an OH^- anion in the interlayer space to balance the charge.¹¹ All of the aluminum in C_4AH_{13} is octahedral. C_2AH_8 and C_4AH_{13} are metastable phases that spontaneously transform into the fully hydrated, thermodynamically stable cubic phase, C_3AH_6 (Eq. I.4). In C_3A , aluminum coordination is tetrahedral. The structure consists of rings of aluminum tetrahedra linked through bridging oxygen atoms, which slightly distorts the aluminum environment. In C_3AH_6 , aluminum exists as highly symmetrical, octahedral $Al(OH)_6$ units.



If the very rapid and exothermic hydration of C_3A is allowed to proceed unhindered in cement, then the setting occurs too quickly and the cement does not develop strength. Therefore, gypsum [calcium sulfate dihydrate, $CaSO_4 \cdot 2(H_2O)$] is added to slow down the C_3A hydration. In the presence of gypsum, tricalcium aluminate forms ettringite, $[Ca_3Al(OH)_6 \cdot 12(H_2O)]_2 \cdot (SO_4)_3 \cdot 2(H_2O)$ (Eq. I.5), which can also be written as $C_3A \cdot 3(CaSO_4) \cdot 32(H_2O)$. Ettringite grows as columns of calcium, aluminum and oxygen surrounded by water and sulfate ions, as shown in Figure I.16.

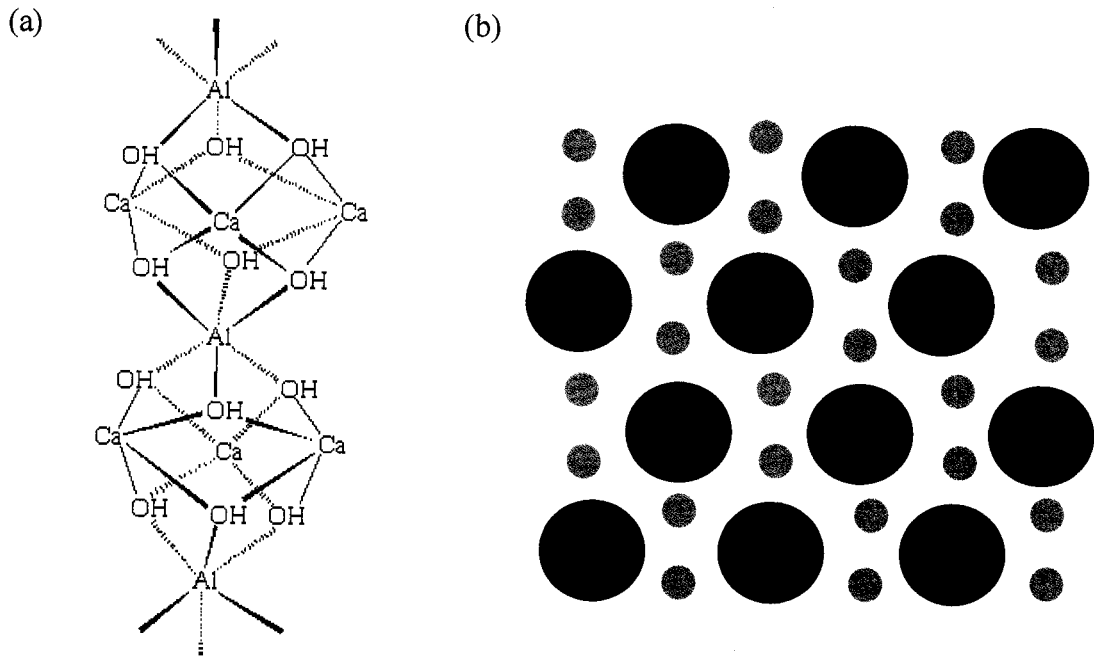
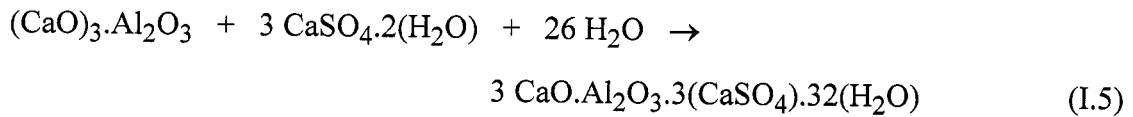


Figure I.16. Ettringite columns (a) consisting of octahedral aluminum, tetrahedral oxygen, and 8-coordinate calcium. The coordination sphere of each calcium is filled by water and sulfate ions. The packing of the columns (b) represented by large circles, the smaller circles represent channels containing with water and sulfate ions.

Tetracalcium aluminoferrite (C_4AF) reacts much like C_3A , i.e., forming ettringite in the presence of gypsum. However, hydration the ferrite phase is much slower than hydration of C_3A , and water is observed to bead up on the surface of C_4AF particles.¹⁷ This may be due to the fact that iron is not as free to migrate in the pastes as aluminum,¹⁸ which may cause the formation of a less permeable iron rich layer at the surface of the C_4AF particles and isolated regions of iron hydroxide.¹¹ In cement, if there is insufficient gypsum to convert all of the C_4AF to ettringite, then an iron-rich gel forms at the surface of the silicate particles which is proposed to slow down their hydration.¹⁹

References

- 1 Industry Overview, Portland Cement Association.
<http://www.cement.org/econ/industry.asp>. Accessed December 2005.
- 2 M. Gadalla, *Pyramid Illusions*, Bastet Publishing, Erie, Pennsylvania, 1997.
- 3 Pozzolanic materials, or pozzolans, are silica- or alumina-based substances which in and of themselves have no cementitious character, but when mixed with lime, may take on cementitious properties when hydrated.
- 4 J. Adam, *Roman Building: Materials and Techniques*, Bloomington, Indiana, University Press, 1994.
- 5 R. W. Lesley, J. Lober, G. Bartlett, *History of the Portland Cement Industry in the United States*, Ayer Company Publishers, Inc., 1972
- 6 *Mater. Res. Soc. Symp. Proc: Scientific Basis for Nuclear Waste Management Vol 212*, Ed's J. Bates and W. Seefeldt, Materials Research Society, Pittsburg, PA, 1991.
- 7 D. K. Smith, *Cementing*, Society of Petroleum Engineers, Richardson, Texas, 1990.

- 8 R. Baker, *A Primer of Oil Well Drilling, 5th Edition*, Petroleum Extensions Service, Austin, Texas, 1996.
- 9 Lewis Norman, Halliburton Energy Services. Personal communication.
- 10 Cement chemists use abbreviated nomenclature based on oxides of various elements to indicate chemical formulae of relevant species. C = CaO, S = SiO₂, A = Al₂O₃, F = Fe₂O₃.
- 11 H. F. W. Taylor, *Cement Chemistry*, Thomas Telford Publishing, London, 1997.
- 12 Calcium hydroxide consists of hexagonal layers of octahedrally coordinated calcium atoms and tetrahedrally coordinated oxygen atoms.
- 13 H. F. W. Taylor, *J. Am. Ceram. Soc.*, 1986, **69**, 464.
- 14 V. S. Ramachandran, R.F. Feldman, and J. J. Beaudoin, *Concrete Science*, Heyden and Son Ltd., Philadelphia, PA, 1981.
- 15 H. N. Stein and J. Stevels, *J. App. Chem.*, 1964, **14**, 338.
- 16 M. Grutzeck, S. Kwan, J. Thompson, and A. Benesi, *J. Mater. Sci. Lett.*, 1999, **18**, 217.
- 17 S. Mehta, R. Jones, B. Caveny, J. Chatterji, and G. McPherson, "Environmental Scanning Electron Microscope (ESEM) examination of individually hydrated Portland Cement phases," Halliburton Research Center, Duncan, OK.
- 18 H. F. W. Taylor and D. E. Newbury, *Cem. Concr. Res.*, 1984, **14**, 565.
- 19 V. S. Ramachandran, *Concrete Admixtures Handbook, 2nd Edition*, Noyes Publications, New Jersey, USA, 1995.

Chapter 1

Basic Considerations for NMR Analysis of Cements

Introduction

Over the years, solid-state nuclear magnetic resonance (NMR) has been used in a wide variety of ways to characterize cements and related materials.¹ Given the major components of cement, it would be expected that it should lend itself to solid-state NMR investigation (Table 1.1); however, despite the presence of NMR active isotopes, there are significant challenges to the use of NMR for characterization of cements. While ^{29}Si and ^{57}Fe are non-quadrupolar nuclei (i.e., spin $1/2$) and should therefore provide relatively sharp, well-resolved spectra, the natural abundance of ^{57}Fe , and hence sensitivity is extremely low. In contrast, ^{17}O , ^{27}Al , and ^{43}Ca have large quadrupole moments resulting in broad resonances with irregular lineshapes. Furthermore, ^{17}O and ^{43}Ca have very low natural abundance, further reducing the ease of data collection.^{2,3,4,5} Studies of ^{17}O , ^{57}Fe and ^{43}Ca suffer further still from the nuclei's exceptionally low magnetogyric ratios, the latter two especially so. As a consequence of these factors, the two main thrusts of the field focus on either ^{27}Al or ^{29}Si NMR, but there are also studies that focus on combined rotation and multipulse spectroscopy (CRAMPS) ^1H NMR^{6,7} and MRI.⁸

Studies in ^{27}Al NMR of cements fall into two general categories: those that observe the aluminum impurities in C-S-H,^{9,10,11} and those that focus on the pure calcium aluminate phases.¹² Work in ^{29}Si NMR bifurcates along analogous lines, with studies tending to focus on either observing the C-S-H hydration product^{13,14} or the unreacted calcium silicates.¹⁵ Research from the Barron group has previously reported the use of a combination of ^{27}Al and ^{29}Si NMR spectroscopy to investigate the interactions of cements with a range of setting retarders.^{16,17}

Table 1.1. Comparison of NMR active isotopes for common elements in cement.

Isotope	Spin	Natural abundance (%)	Magnetogyric ratio (10^{-7} rad T s $^{-1}$)	Quadrupole moment (10^{-28} m 2)	Relative sensitivity	Absolute sensitivity
^{17}O	5/2	0.037	-3.63	-0.026	2.91×10^{-2}	1.08×10^{-5}
^{27}Al	5/2	100	6.98	0.149	0.21	0.21
^{29}Si	1/2	4.7	-5.32	0	7.84×10^{-3}	3.69×10^{-4}
^{43}Ca	7/2	0.145	-1.80	-0.05	6.40×10^{-3}	9.28×10^{-6}
^{57}Fe	1/2	2.19	0.869	0	3.37×10^{-5}	7.83×10^{-7}

One important element of cement NMR that has received little attention is the presence of paramagnetic Fe^{3+} ions in the C_4AF matrix. The impact of paramagnetism on NMR spectra is well known, causing signal loss (though specialized techniques may be employed to observe the disappearing signal nearest the paramagnetic centers¹⁸), line broadening, and/or chemical shift alteration, as well as (in many cases dramatically) decreasing longitudinal (T_1) relaxation times. On occasion, researchers have added paramagnetic species to their samples to maximize the signal-to-noise ratio achievable per unit time.¹⁹ Given the inherent presence of paramagnetic centers in cement (i.e., the Fe^{3+} ions in the C_4AF matrix, see Figure I.15) this work acts on an interest in the potential for obtaining signal-enhanced ^{29}Si NMR data from cements as compared to the pure mineral and using this data as a predictive tool in understanding cement kinetics. This signal enhancement does not come without a price, however. Paramagnetism not only increases possible pulse repetition rates, but also broadens the resonances by forcing

down the transverse relaxation time T_2 and the apparent transverse relaxation time, T_2^* , which is inversely proportional to the halfwidth of a resonance.

The present chapter focuses on the application of ^{29}Si NMR to the systems relating to cements, taking steps to exploit the paramagnetism present where possible. The impact of the paramagnetism on the T_1 relaxation curve is further discussed further in Chapter 2, and the use of ^{29}Si NMR as a predictive tool are presented in Chapters 3 and 4.

Results and Discussion

^{29}Si NMR of cement. A basic ^{29}Si NMR MAS spectrum of a cement sample from Texas Lehigh Cement Company, LP is shown in Figure 1.1a. The spectrum consists of a single peak with complex lineshape, arising from the overlapping resonances of the C_3S and C_2S silicate moieties, broadened by the paramagnetic C_4AF matrix. This particular spectrum was collected for 10240 scans with a relaxation delay of 60 seconds, a typical relaxation delay for a spectrum that would be collected for a standard diamagnetic silicate. The total acquisition time was 7 days, 2 hours, 49 minutes, and 14 seconds; practical maintenance considerations prohibit collecting spectra for longer durations.

Figure 1.1b shows the ^{29}Si NMR spectrum of the same Texas Lehigh cement sample as shown in Figure 1.1, but collected with no relaxation delay whatsoever. The lack of use of such a delay allows the sample to relax only during FID acquisition. Were the sample diamagnetic, the resonance would saturate after a handful of scans and the spectrum collected would rapidly lose signal-to-noise as noise built up but no signal would be generated in subsequent scans. As is apparent from the spectra, the lineshape is virtually identical to that in Figure 1.1a, but in this spectrum ten times as many scans were collected, and all in a mere 1 hour, 31 minutes, 46 seconds.

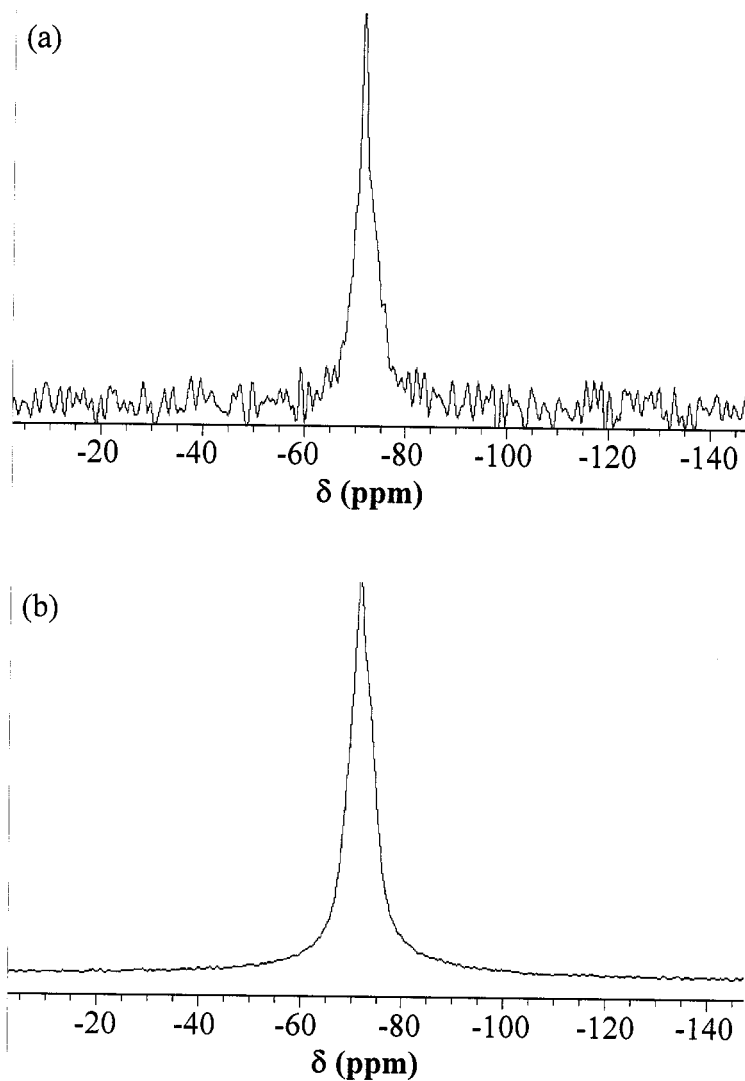


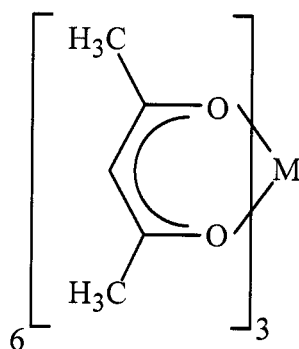
Figure 1.1. Standard Bloch decay NMR spectrum of a Texas Lehigh cement. (a) 10240 scans with a relaxation delay of 60 s. Signal to noise ratio: 25.5. (b) 102400 scans with no relaxation delay. Signal to noise ratio: 1336.3.

The surprisingly high degree of similarity between the spectra in Figure 1.1 was the catalyst for the interest in NMR as a potentially novel tool for cement analysis. Firstly, it suggests that ^{29}Si NMR spectra of cements can be collected rapidly with no relaxation delay, which would go a long way toward overcoming ^{29}Si 's mediocre magnetogyric ratio and poor natural abundance. Secondly, since the Fe^{3+} is present in the C_4AF matrix

ratio and poor natural abundance. Secondly, since the Fe^{3+} is present in the C_4AF matrix that surrounds the C_3S and C_2S mineral particles, these minerals will feel the effects of the paramagnetic centers.

The ramifications of the paramagnetism present due to the C_4AF in cements ultimately come down to a reduction of the longitudinal relaxation time, T_1 . This reduction in T_1 , which is normally quite long for a typical diamagnetic solid when compared to comparable solution state relaxation times, allows for a far more rapid pulse repetition rate, which in turn builds signal at a much faster rate, thereby allowing for a greater acquisition of signal-to-noise ratio per unit time. Experiments that might otherwise take weeks or even months, as shown in Figure 1.1, now take mere hours.

^{29}Si NMR of model systems. In order to verify the impact of the paramagnetism on the silicates within cements, we have prepared a series of model samples by the addition of a paramagnetic additive to the surface of silicates that are not inherently paramagnetic. Samples of fumed silica (SiO_2), C_3S , and C_2S were coated via evaporation deposition of $\text{M}(\text{acac})_3$ (I, $\text{M} = \text{Fe}^{3+}$, Cr^{3+}) at a loading of approximately 1% by mass. Iron(III) and chromium(III) were chosen for M for their high paramagnetism,



(I)

ease of dissolution, and low cost. Iron(III) in an octahedral coordination environment has a d^5 valence shell and is almost invariably high spin, resulting in five unpaired electrons;

chromium(III) is also in a high spin state in this coordination environment, producing a more modest three unpaired electrons from its d^3 valence. The compounds were dissolved in acetone, and the silicate powder substrates were coated with the $M(\text{acac})_3$ solution. The solution was allowed to evaporate, which deposited the $M(\text{acac})_3$ on silicate powders. A schematic representation of the particles is shown in Figure 1.2.

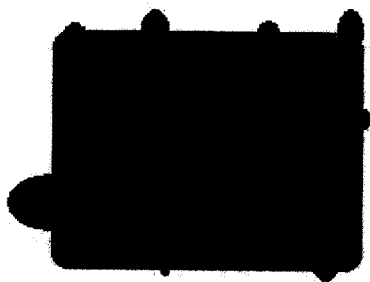


Figure 1.2. Schematic representation of partially $M(\text{acac})_3$ -coated silicate.

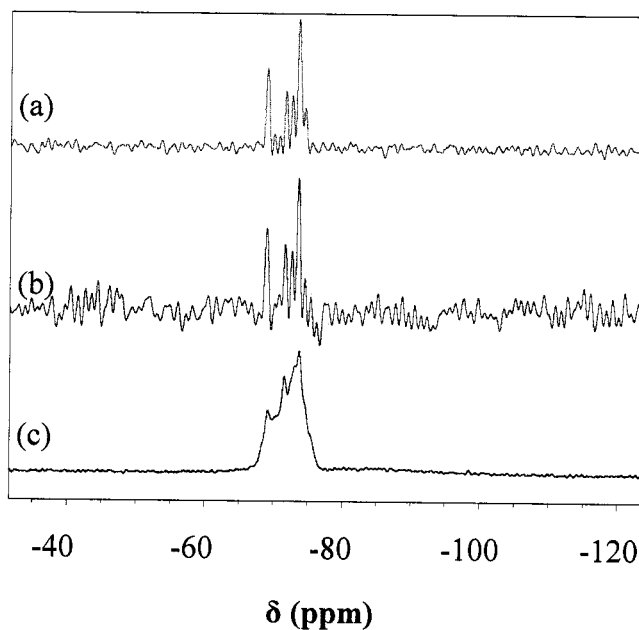


Figure 1.3. ^{29}Si NMR of C_3S (a) with $\text{Fe}(\text{acac})_3$, (b) with $\text{Cr}(\text{acac})_3$, (c) without paramagnetic material added.

Figures 1.3, 1.4, and 1.5 show the ^{29}Si MAS spectra of the coated and uncoated C_3S , C_2S , and fumed silica, respectively. As is evident in the graphs, the resonances of all the silicates broaden in the presence of the paramagnetic relaxation agent, with the inexplicable exception of the C_3S , which seem to sharpen upon introduction of paramagnetic character.

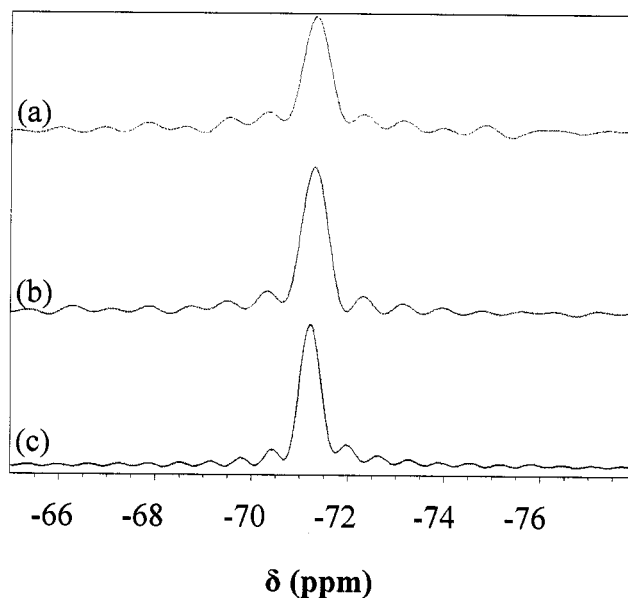


Figure 1.4. ^{29}Si NMR of C_2S (a) with $\text{Fe}(\text{acac})_3$, (b) with $\text{Cr}(\text{acac})_3$, and (c) without paramagnetic material added.

Additionally, the T_1 values are affected. The T_1 values were measured via the inversion recovery method. The inversion recovery method utilizes a 180° pulse to invert the sample's net magnetization vector in the rotating frame of reference. This inversion pulse is followed by the variable mixing period τ which gives the single varying time to relax back to equilibrium. At a minimal value of τ , the signal is inverted; as τ increases, the negative signal diminishes, reaches a null point, then grows in the positive direction reaching an effective maximum at large values of τ . At the end of the mixing time, an

observation pulse is applied, followed by acquisition. Further considerations of the inversion recovery method are explored in Chapter 2. Figures 1.6, 1.7, and 1.8 show the inversion recovery spectra; the results of the relaxation measurements are contained in Table 1.2. As expected, the T_1 relaxation values decrease, thus permitting expedited signal acquisition. However, the degree of reduction in the T_1 observed was far greater for the fume silica than it was for the other minerals, owing to its higher surface area and consequently greater degree of coverage, bringing more paramagnetism in close proximity to more ^{29}Si nuclei.

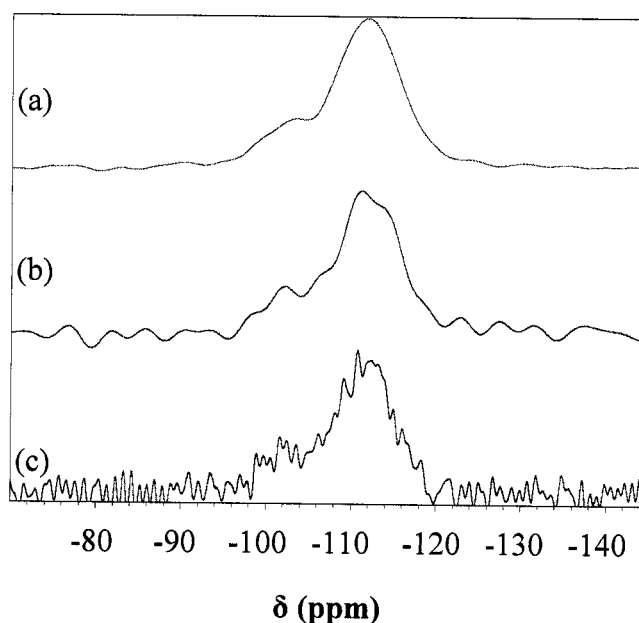


Figure 1.5. ^{29}Si NMR of fumed silica (a) with $\text{Fe}(\text{acac})_3$, (b) with $\text{Cr}(\text{acac})_3$, and (c) without paramagnetic material added.

Conclusions

It has been demonstrated that introduction of paramagnetic species into an otherwise diamagnetic system can dramatically decrease the longitudinal relaxation time T_1 . The T_1 of C_3S and C_2S can change in cement because of the Fe^{3+} present in the

C_4AF matrix that makes intimate contact with the silicate phases. Further exploration of the implications of this signal enhancement and broadening are explored in Chapter 2, where various techniques are applied to evaluate the longitudinal relaxation of an example cement.

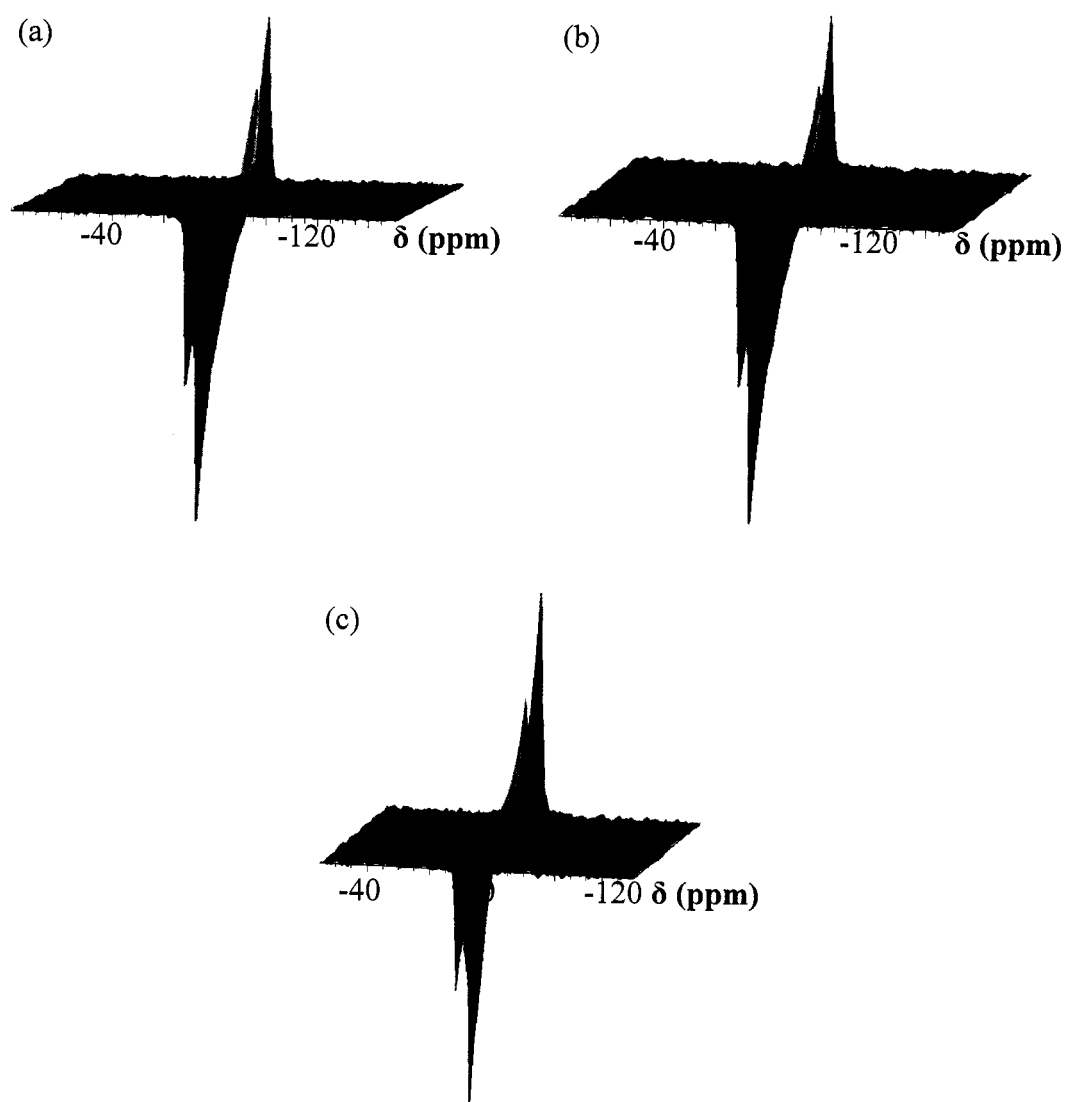


Figure 1.6. Inversion recovery spectrum of C_3S (a) with $Fe(acac)_3$, (b) with $Cr(acac)_3$, and (c) without paramagnetic material added.

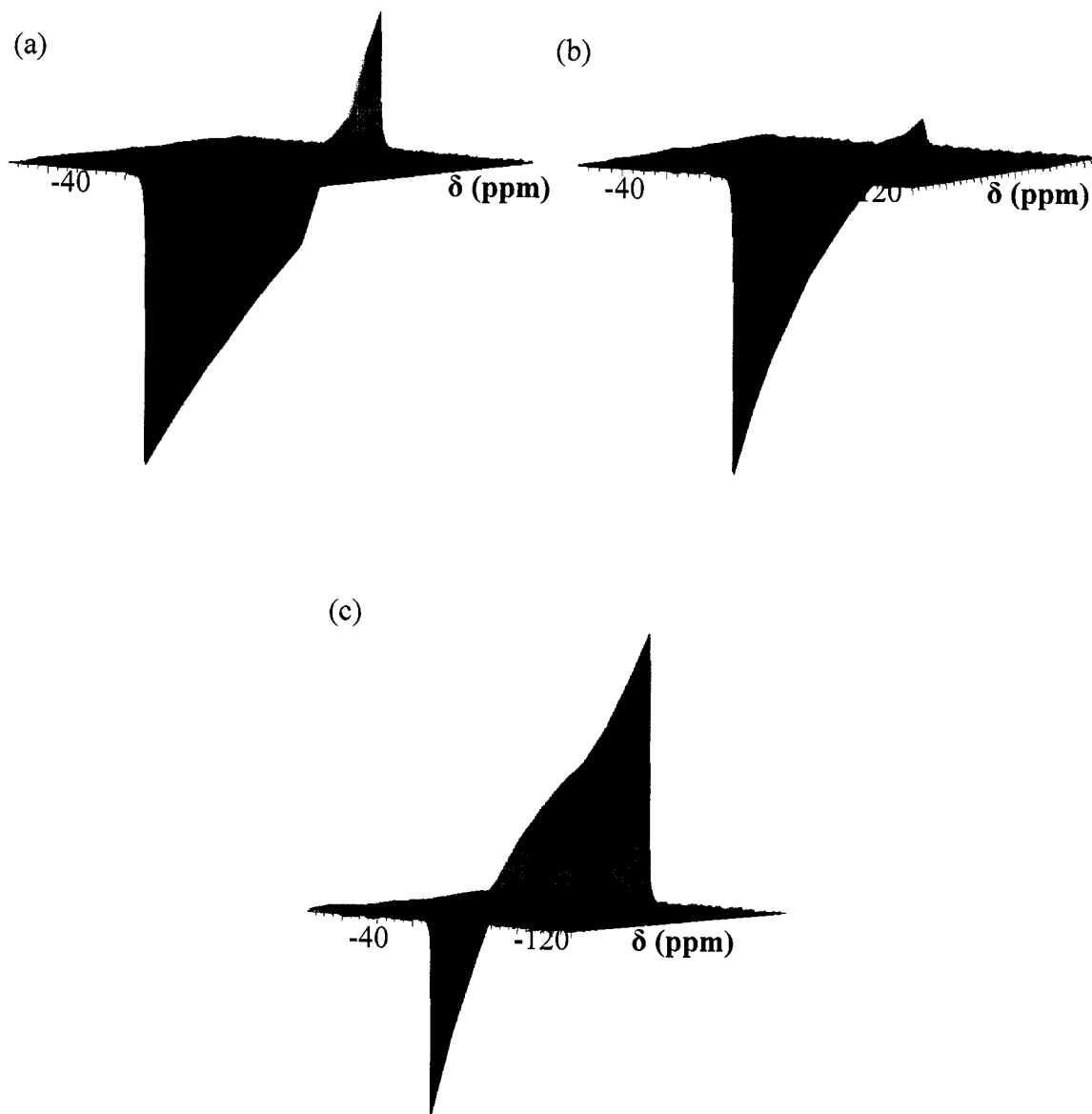


Figure 1.7. Inversion recovery spectrum of C_2S (a) with $Fe(acac)_3$, (b) with $Cr(acac)_3$, and (c) without paramagnetic material added.

Experimental

The fumed silica was obtained from British Petroleum, Inc. The $M(acac)_3$ compounds were obtained from Sigma-Aldrich, Inc. The C_3S and C_2S samples were obtained from Construction Technology Laboratories, Inc., Skokie, Illinois. The Texas

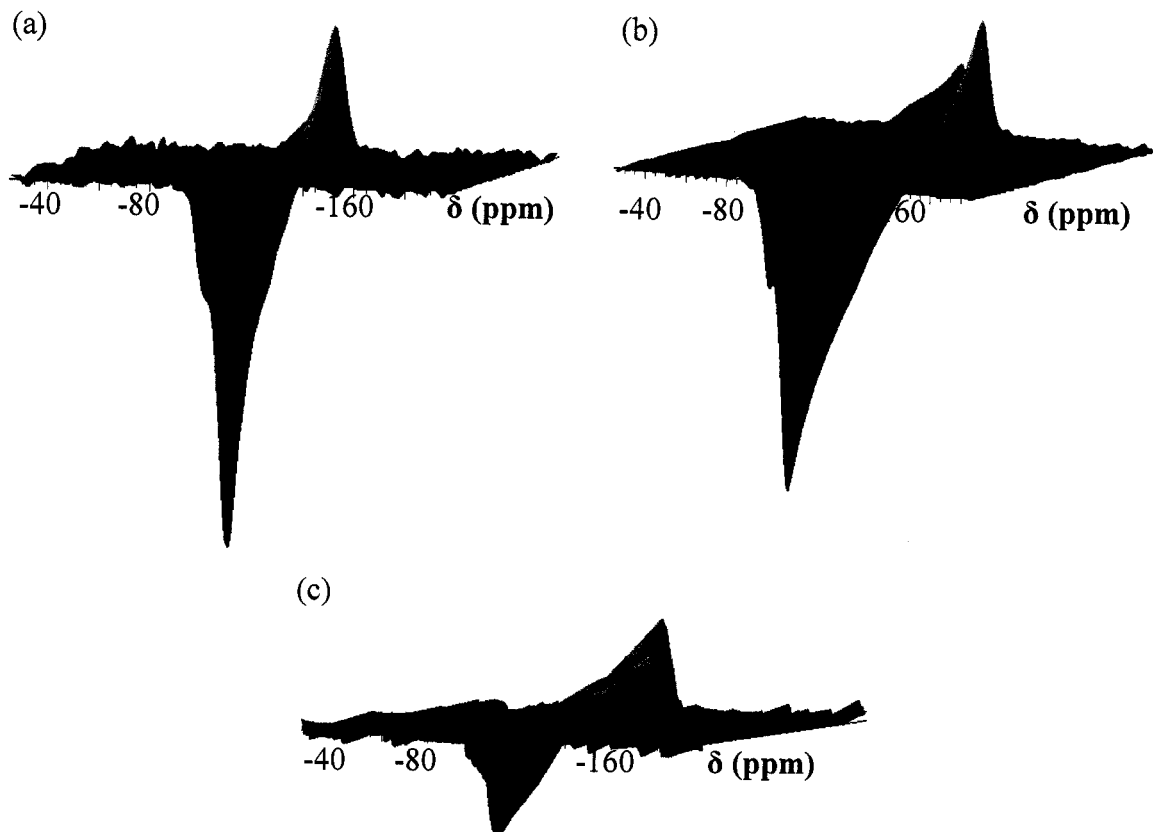


Figure 1.8. Inversion recovery spectrum of fumed silica (a) with $\text{Fe}(\text{acac})_3$, (b) with $\text{Cr}(\text{acac})_3$, and (c) without paramagnetic material added.

Table 1.2. Inversion recovery measurements of T_1 (s) for C_3S , C_2S , and SiO_2 with and without $\text{M}(\text{acac})_3$ ($\text{M} = \text{Fe}, \text{Cr}$).

Sample ID	as received	with $\text{Cr}(\text{acac})_3$	with $\text{Fe}(\text{acac})_3$
C_2S	3.63	2.21	0.83
C_3S	3.04	1.53	1.65
SiO_2	62.72	2.24×10^{-4}	1.74×10^{-4}

Lehigh cement was furnished by Halliburton Energy Services, Duncan, OK. All Materials were used as received.

^{29}Si NMR spectroscopy. Solid state ^{29}Si MAS NMR spectra were collected on a Bruker Avance 200 spectrometer at 39.76 MHz. Samples were measured using a 7 mm extended VT MAS probe with 7 mm long-barrel ZrO_2 rotors and plugs and Kel-F fluoropolymer caps. Chemical shifts are referenced to hexamethylcyclotrisiloxane (δ - 9.66) by sample replacement. All spectra were collected at a magic angle spinning speed of 6.00 kHz without high power ^1H decoupling. Spectra were acquired using a 90° ^{29}Si pulse of 5.75 μs and a spectral width of 14,750 Hz unless otherwise specified. Data was acquired either with Bruker Biospin's XWINNMR v2.6 or TopSpin v1.3.

T_1 relaxation times measured *via* the inversion recovery method were collected initially over a telescoping range of mixing periods (τ). After initial processing of data, the times closest to exhibiting a null-crossing of the C_2S were identified and subsequent inversion recovery runs were carried out over the proper time regime to identify the null-crossing time to the nearest 1 ms. Data was processed with Topspin v1.3. Fourier transforms were applied without line broadening, phase corrections were made manually, and a fifth order polynomial was fit to the baselines across the F_2 dimension.

Preparation of $\text{M}(\text{acac})_3$ -coated silicates. Samples of C_3S , C_2S , and fumed silica (10 g) were loosely poured into a lidless standard glass Petri dish and covered with 1% (m/v) solutions of $\text{M}(\text{acac})_3$ ($\text{M} = \text{Fe}, \text{Cr}$) in acetone to a loading of 1% $\text{M}(\text{acac})_3$ by mass and covered with a KimwipeTM laboratory tissue. The solutions evaporated under ambient laboratory conditions, depositing the $\text{M}(\text{acac})_3$ onto the particles.

References

- 1 W. Wieker, C. Hubert and D. Heidemann. *Proc. Int. Congr. Chem. Cem. 10th*, 1997, **1**, 2.
- 2 J. Emery, D. Massiot, P. Lacorre, Y. Laligant, and K. Conder, *Magn. Reson. Chem.*, 2005, **43**, 366.
- 3 A. Trokiner, L. Le Noc, A. Yakubovskii, K. N. Mykhalyov, and S. V. Verkhovskii, *Z. Naturforsch.*, 1993, **49a**, 373.
- 4 Z. J. Lin, M. E. Smith, F. E. Sowrey, and R. J. Newport, *Phys. Rev. B*, 2004, **69**, 224107/1.
- 5 R. Dupree, A. P. Howes, and S. C. Kohn, *Chem. Phys. Lett.*, 1997, **276**, 399.
- 6 B. Bresson, H. Zanni, and S. Masse, *J. Mater. Sci.*, 1997, **32**, 4633.
- 7 P. S. Wang, M. M. Ferguson, G. Eng, D. P. Bentz, C. F. Ferraris, and J. R. Clifton, *J. Mater. Sci.*, 1998, **3**, 3065.
- 8 P. J. Prado, B. J. Balcom, S. D. Beyea, T. W. Bremner, R. L. Armstrong, and P. E. Grattan-Bellew, *Cem. Conc. Res.*, 1998, **28**, 261.
- 9 J. Schneider, M. Cincotto and H. Panepucci. *Cem. Conc. Res.*, 2001, **31**, 993.
- 10 P. Faucon, T. Charpentier, D. Bertrandie, A. Nonat, J. Virlet, and J. C. Petit. *Inorg. Chem.*, 1998, **37**, 3626.
- 11 P. Faucon, T. Charpentier, A. Nonat, and J. C. Petit, *J. Am. Chem. Soc.*, 1998, **120**, 12075.
- 12 J. Skibsted, E. Henderson and H. Jakobsen. *Inorg. Chem.*, 1993, **32**, 1013.
- 13 K. Haga, M. Shibata, M. Hironaga, S. Tanaka, and S. Nagasaki, *J. Nuc. Sci. Tech.*, 2002, **39**, 540.
- 14 K. Johansson, C. Larsson, O. N. Antzutkin, W. Forsling, H. R. Kota, and V. Ronin, *Cem. Conc. Res.*, 1999, **29**, 1575.

- 15 J. Skibsted, H. Jakobsen, and C. Hall, *J. Chem. Soc. Faraday Trans.*, 1995, **91**(24), 4423.
- 16 M. Bishop, S. G. Bott, and A. R. Barron, *Chem. Mater.*, 2003, **15**, 3074.
- 17 M. Bishop and A. R. Barron, *Ind. Eng. Chem. Res.*, 2006, **45**, 702.
- 18 G. B. Furman and S. D. Goren, *J. Phys.: Condens. Matter*, 2002, **14**, 873.
- 19 Fujiu and M. Ogino, *J. Non-Crystalline Solids*, 1984, **64**, 287.

Chapter 2

Comparison of Methods of NMR Relaxation Analysis

Introduction

In Chapter 1 it was demonstrated that the presence of a paramagnetic species in intimate (physical) contact with a silicon-containing mineral allows for the rapid data collection of the ^{29}Si MAS NMR spectrum. Additionally, the paramagnetic material can potentially act as a probe of the heterogeneity of the intermingled silicate system. While paramagnetic species are known to wipe out the Zeeman interaction within *ca.* 1 nm, it is also known to influence the relaxation behavior of nearby nuclei outside the 1 nm “dead zone” with an inverse r^3 dependence.¹ While techniques such as X-ray fluorescence and X-ray diffraction effectively measure the content of the entire particle, NMR relaxation analysis can potentially focus on the collective surfaces of the silicates, whose hydration forms the backbone of solidified and hardened cements. Figure 2.1 provides a graphical representation of the relative portions of a particle studied in a paramagnetic matrix.



Figure 2.1. Detection fractions of a particle (dark green) versus the remainder of the particle (light green) when (a) studied by X-ray fluorescence and X-ray diffraction, and (b) when evaluated by NMR relaxation analysis, allowing for more relaxation to occur from left to right.

In this Chapter the focus will be on exploring the nuclear spin relaxation behavior of the C_2S and C_3S present in cement particles by means of several different NMR spectroscopic techniques in order to ascertain the methodology most appropriate to enable a comparison of data from a series of cement samples with physical measurements. Since the early formation of C-S-H, the primary dictator of solidification and strength development, depends predominantly on the quantity of C_3S available for reaction (see Introduction), gaining useful information about the amount of C_3S able to hydrate is of value. Since cement manufacturing is controlled primarily by regulation of silicon content and the ultimate fate of silicon is in either C_3S or C_2S , knowledge of the C_3S/C_2S ratio puts the amount of C_3S alone in the context of the whole cement.

Based on the premise that an accurate (as well as fast and simple) measurement of the C_3S/C_2S ratio is important in understanding the potential reaction chemistry of cements, there is naturally an interest in determining the optimum methodology for this data collection. Of several alternatives, the inversion recovery and saturation recovery methods as well as variable delay Bloch decay experiments have been chosen for investigation.

The first technique to be considered is the inversion recovery method. Figure 2.2 provides a diagram of the impact of the inversion recovery pulse sequence on the net magnetization vector. This method utilizes a 180° pulse to put the sample's net magnetization vector at equilibrium (Figure 2.2a) onto the $-z$ axis (Figure 2.2b) in the rotating frame of reference. This inversion pulse is followed by the variable delay period (τ) that gives the magnetization varying time to relax back to the $+z$ axis. The signal relaxes back to equilibrium according to the equation $I(\tau) = I_0[1 - 2\exp(-\tau/T_1)]$, where I_0 represents the maximum signal intensity. Figure 2.3 shows a graphical representation of the impact of τ on the intensity of a given peak. At very short values of τ , the net magnetization vector is inverted (Figure 2.2d); as τ increases, the negative magnetization diminishes, reaches a null point when τ equals $T_1\ln(2)$, then grows in the positive

direction (Figure 2.2c) reaching an effective maximum at a τ of *ca.* $5T_1$. At the end of the delay time, a 90° pulse is applied (Figure 2.2e,f) to push the z-component of the net magnetization vector into the xy plane of the rotating frame, allowing for observation and acquisition of a scan (Figure 2.2g,h).

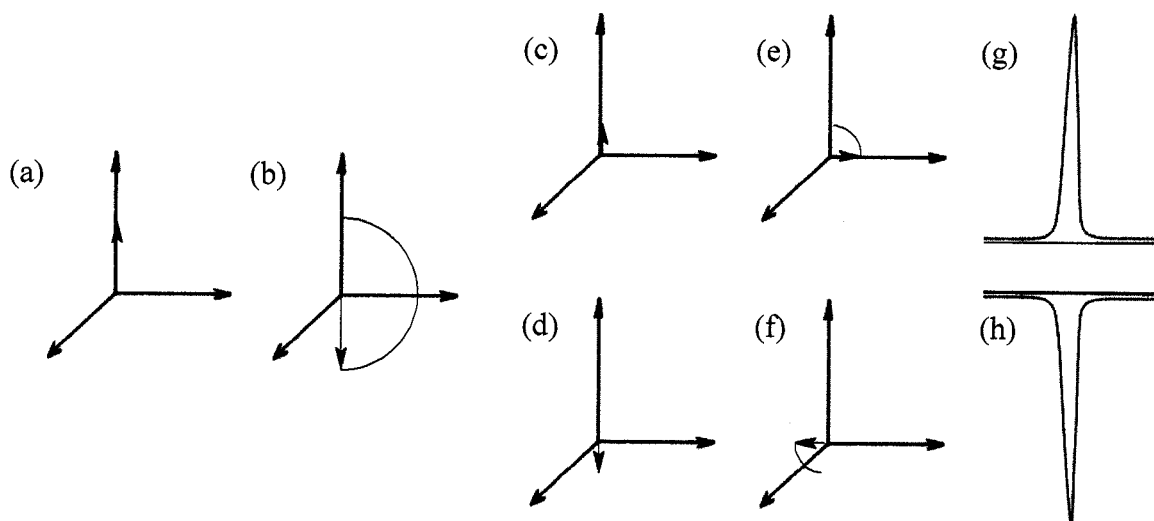


Figure 2.2. Schematic diagram of the inversion recovery experiment. See text.

Inversion recovery is the preferred method for analyzing the T_1 relaxation times of most ordinary (i.e., homogeneous and diamagnetic) samples, as the magnetization vector is under tightest control, and thus tends to give the most accurate measurements. The downside of inversion recovery in the general case comes from the requirement of a relaxation delay of at least five times the expected value of T_1 , resulting in long waiting periods between acquisitions and imposing a practical limit on the amount of signal which may be acquired in a reasonable time frame.

The conventional alternative to inversion recovery for measuring T_1 relaxation times is the saturation recovery method. In this method, the sample signal is saturated by a pulse train, a rapid succession of pulses applied to eliminate the net magnetization vector. The pulse train is then followed by a varying recovery period τ during which the

signal returns to equilibrium on the +z axis. The signal relaxes back to equilibrium according to the equation $I(\tau) = I_0[1 - \exp(-\tau/T_1)]$. Figure 2.4 shows a graphical representation of the impact of τ in a saturation recovery experiment on the intensity of a given peak. At the end of the recovery period, a 90° pulse is applied to put the z component of the net magnetization vector into the xy plane of the rotating frame, allowing for observation and acquisition of a scan.

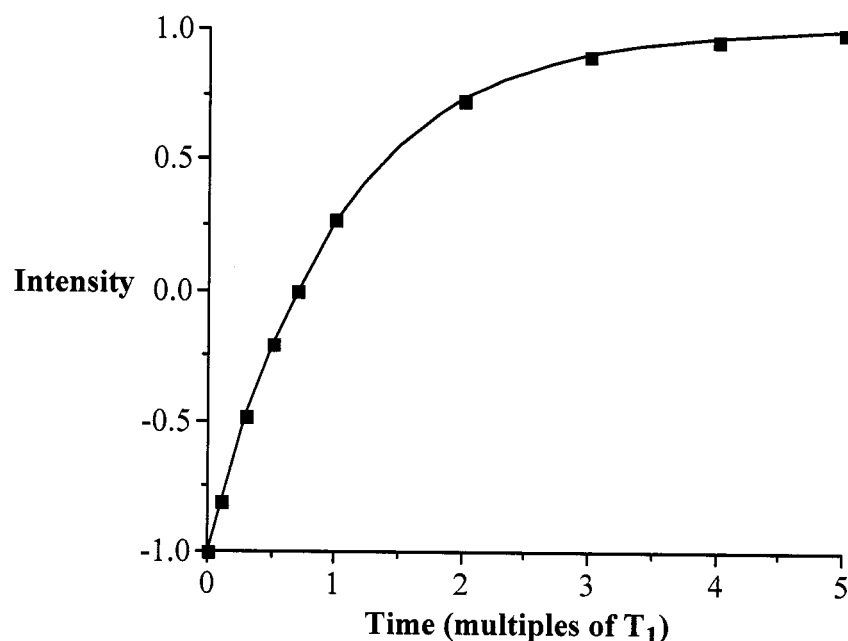


Figure 2.3. Graphical representation of the impact of the variable mixing period (τ) on the intensity of a given peak in an inversion recovery experiment for a typical diamagnetic, homogeneous material.

The saturation recovery method has the advantage of generating peaks of only non-negative intensity. This characteristic becomes particularly advantageous when dealing with overlapping signals, where the guarantee of positive intensity from all observable signals eliminates the complication of overlapping positive and negative

peaks, which often produce undesirably complex lineshapes. Additionally, this method provides a clearer expression of the impact of paramagnetic species on the relaxation behavior of a heterogeneous material, in the same line of analysis as that used by Hunter and co-workers.² The primary disadvantage of this method comes from the difficulty in establishing a pulse train sufficient to completely saturate the net magnetization vector prior to the recovery period.

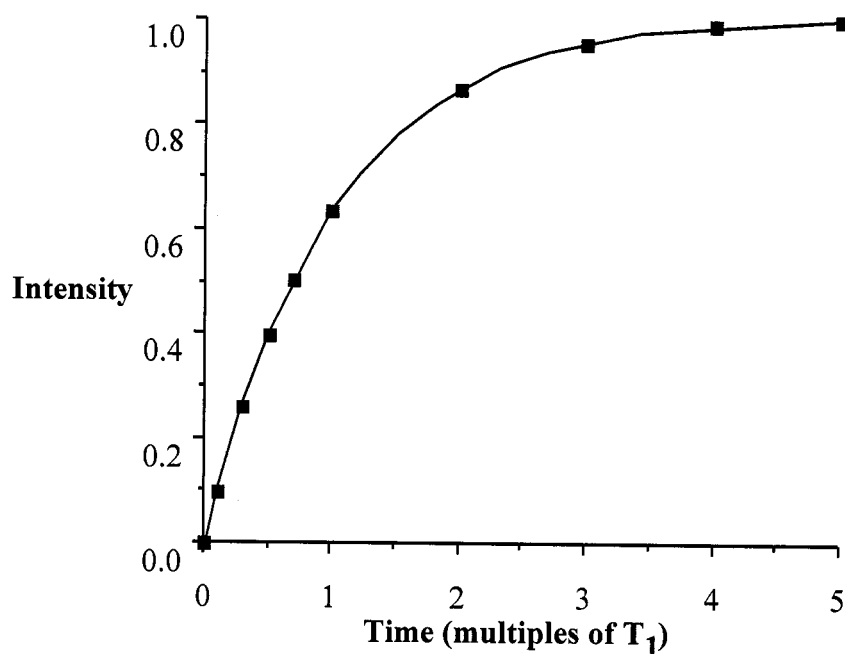


Figure 2.4. Graphical representation of the impact of the variable mixing period (τ) on the intensity of a given peak in a saturation recovery experiment for a typical diamagnetic, homogeneous material.

Relaxation behavior may also be explored more obliquely through a variable delay Bloch decay experiment, wherein standard Bloch decay spectra are acquired (after sufficient dummy scans are run to establish a steady state of spin relaxation) with varying relaxation delays. In this way, the spectra may approximate the data collected in the

saturation recovery runs, with the sum of the relaxation delay and duration of the FID approximately equating to the saturation recovery values of τ . This method has the advantage of acting as a screening tool for streamlined analysis if a given saturation recovery spectrum is found to be particularly effective at predicting hydration behavior. The biggest disadvantage of this method of characterization is its inability to evaluate relaxation values less than the duration of the FID.

This chapter will demonstrate the application of these three relaxation analysis techniques to an exemplar sample of cement: Capitol Aggregates, Ltd.'s Cement Division (CAP). CAP is an API class H cement produced in the San Antonio area, and data by all three methods was available for comparative analysis. Its general relaxation behavior is not unlike any cement, and can readily serve to illustrate the capabilities of these techniques to study cements.

Results and Discussion

Inversion recovery method. Figure 2.5 shows the pseudo-2D inversion recovery spectrum of a sample of CAP cement. The spectrum shows at long and short values of τ the (inverted) signal and typical overlapping lineshape expected of oil well cements (see Chapter 1). However, at intermediate values of τ , the C_3S has begun to pass its null point, while the C_2S remains in the negative intensity regime. The result is a lineshape with both positive and negative intensity simultaneously, greatly complicating further analysis and extraction of useful data. A sub-spectrum illustrating this phenomenon is shown in Figure 2.6. In an effort to overcome this limitation, one may begin with the assumption made by Skibsted *et al.*³ that at the point when the C_2S signal is nulled, the C_3S has fully relaxed. From this assumption, one may isolate the spectrum at the null-crossing point for the C_2S (which will be representative of the C_3S content) and subtract it from the fully relaxed spectrum in order to estimate the C_2S present in the sample. Figure 2.7 provides an illustration of this process. This method, while ingenious in concept, is ultimately

flawed, however, as the C_2S is nulled at a point prior to the C_3S component's full relaxation, as seen in Figure 2.6.

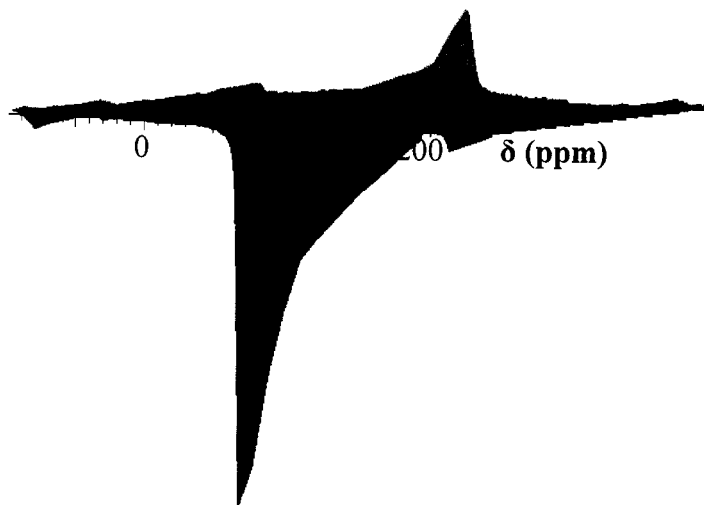


Figure 2.5. Inversion recovery spectrum of cement sample CAP.

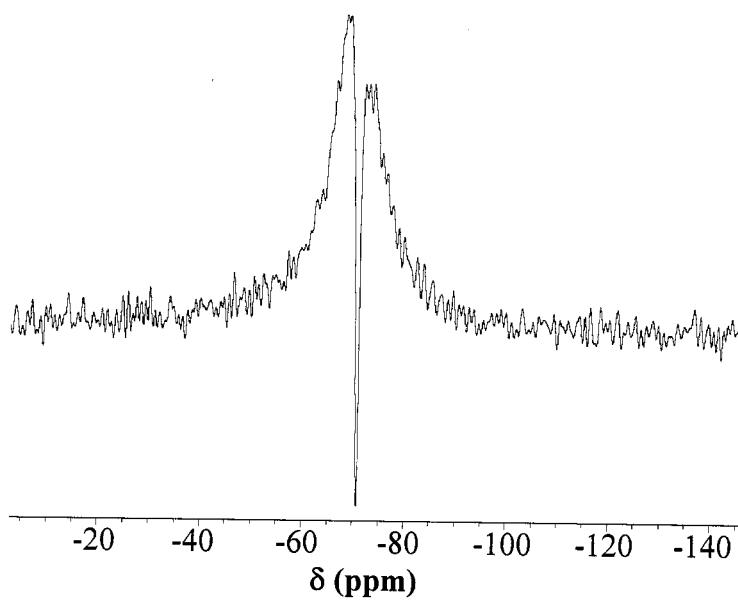


Figure 2.6. Sub-spectrum of the inversion recovery data above illustrating the superposition of positive C_3S signal and negative C_2S signal.

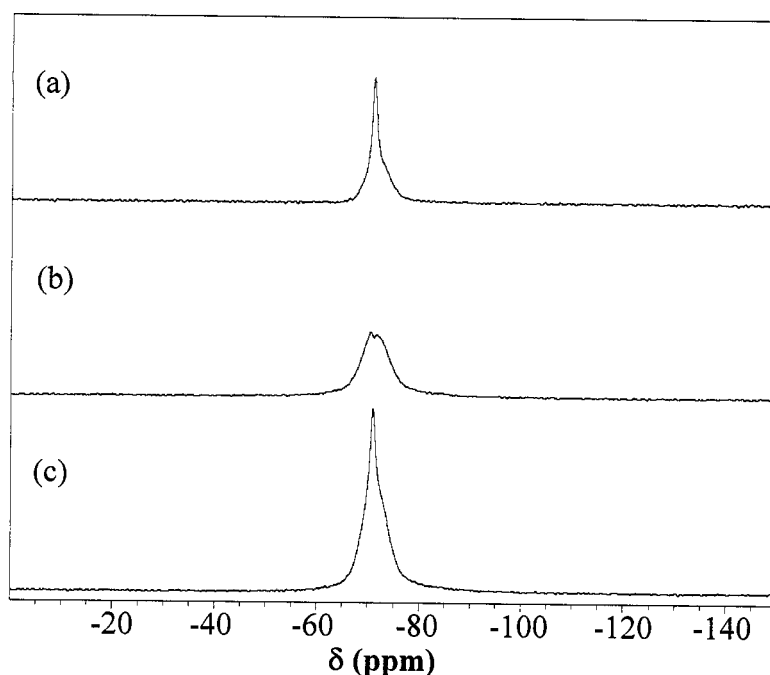


Figure 2.7. Sub-spectrum subtraction for estimation of C_3S and C_2S content. (c) Fully relaxed sub-spectrum; (b) C_2S -nulled sub-spectrum; and (a) difference, showing C_2S and residual C_3S .

In summary, inversion recovery is an unacceptable model for relaxation analysis of cements in the general case. Overlapping positive and negative peaks in sub-spectra make deconvolution extremely difficult at best and impossible at worst. Methods to work around the need for deconvolution by exploitation of differential relaxation times of the C_2S and C_3S are unreliable at best.

Saturation recovery method. In light of the complications observed in the inversion recovery spectra, consideration now moves to the method of saturation recovery. Figure 2.8 shows the pseudo-2D saturation recovery spectrum of CAP. It is noteworthy that the sub-spectra contains only non-negative peaks and that the lineshape changes as the relative contributions of the C_3S and C_2S change with increasing recovery

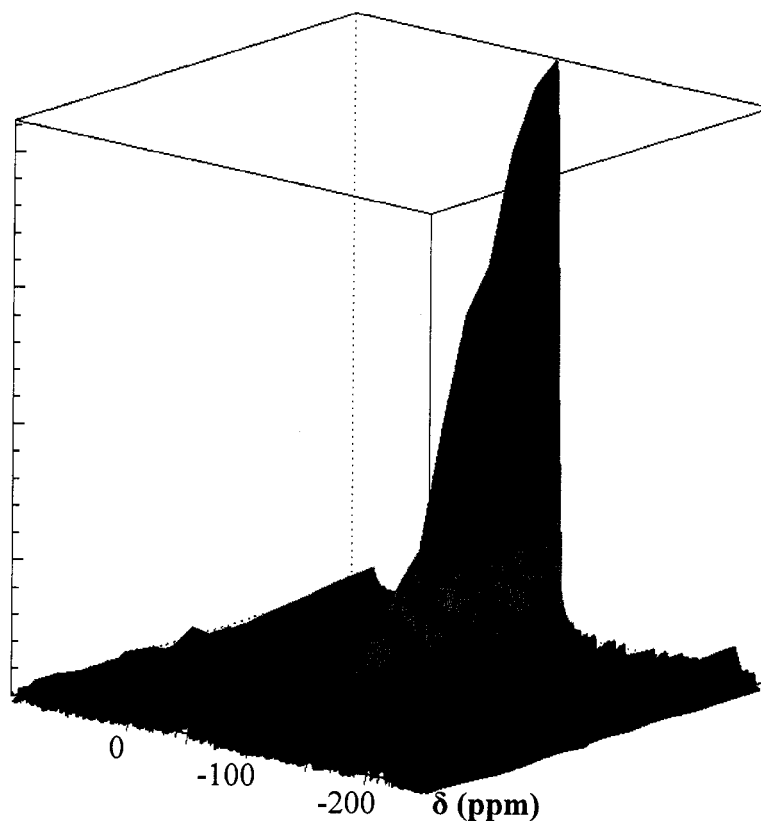


Figure 2.8. Saturation recovery spectrum of cement sample CAP.

period τ . As this data is relatively well behaved compared to the inversion recovery data, a more detailed analysis becomes readily accessible. To this end, deconvolution analysis is applied to each sub-spectrum to isolate the C_2S signal from the C_3S signal. While Skibsted *et al.* used deconvolution analysis to fully relaxed cement samples and observed correlation with quantification via XRD;³ this work applies deconvolution throughout the saturation recovery analysis to track the separate relaxation regimens of the two minerals. Table 2.1 contains an example of the output of the deconvolution optimization used in further processing. Figure 2.9 shows the sub-spectra of the saturation recovery spectrum focused on the region of greatest change in signal.

Owing to practical constraints on time, data corresponding to extremely low values of τ are often too low in signal-to-noise ratio to detect in the same number of scans

Table 2.1. Raw data from deconvolution of saturation recovery sub-spectrum CAP (3 s).

Peak ID	Peak attribution	Chemical Shift (ppm)	Peak intensity (arb. units)	Peak width ^a (Hz)
1	C ₃ S 1	-67.381	27606352	187.56
2	C ₃ S 2	-68.994	35592161	83.28
3	C ₃ S 3	-70.166	59278642	62.99
4	C ₂ S	-71.166	91273950	54.91
5	C ₃ S 4	-72.145	65171374	59.01
6	C ₃ S 5	-73.231	49386078	70.42
7	C ₃ S 6	-74.543	36647253	99.23
8	C ₃ S 7	-76.948	17194682	167.06

^a Halfwidth of Gaussian peak.

as data of intermediate value, and data corresponding to higher, multi-second values of τ are too time-intensive to take the number of scans desired at intermediate values of τ . In order to attempt to collect this data in a practical time frame, the extreme values of τ are collected in their own separate experiments, with values overlapping the intermediate range serving as a rescaling tool to combine the data sets. An example of such data collection is given in Figure 2.10, which shows the saturation recovery data at extreme values of τ for the sample in question.

In Figure 2.10a, the C₂S peak is not shown, due to the deconvolution analysis optimizing the peak to an intensity less than 1% of the next largest peak. This is most likely a consequence of the low signal-to-noise ratio present in virtually all sub-spectra

with sub-millisecond values of τ . As such, all data in this noisier regime should be viewed with greater caution.

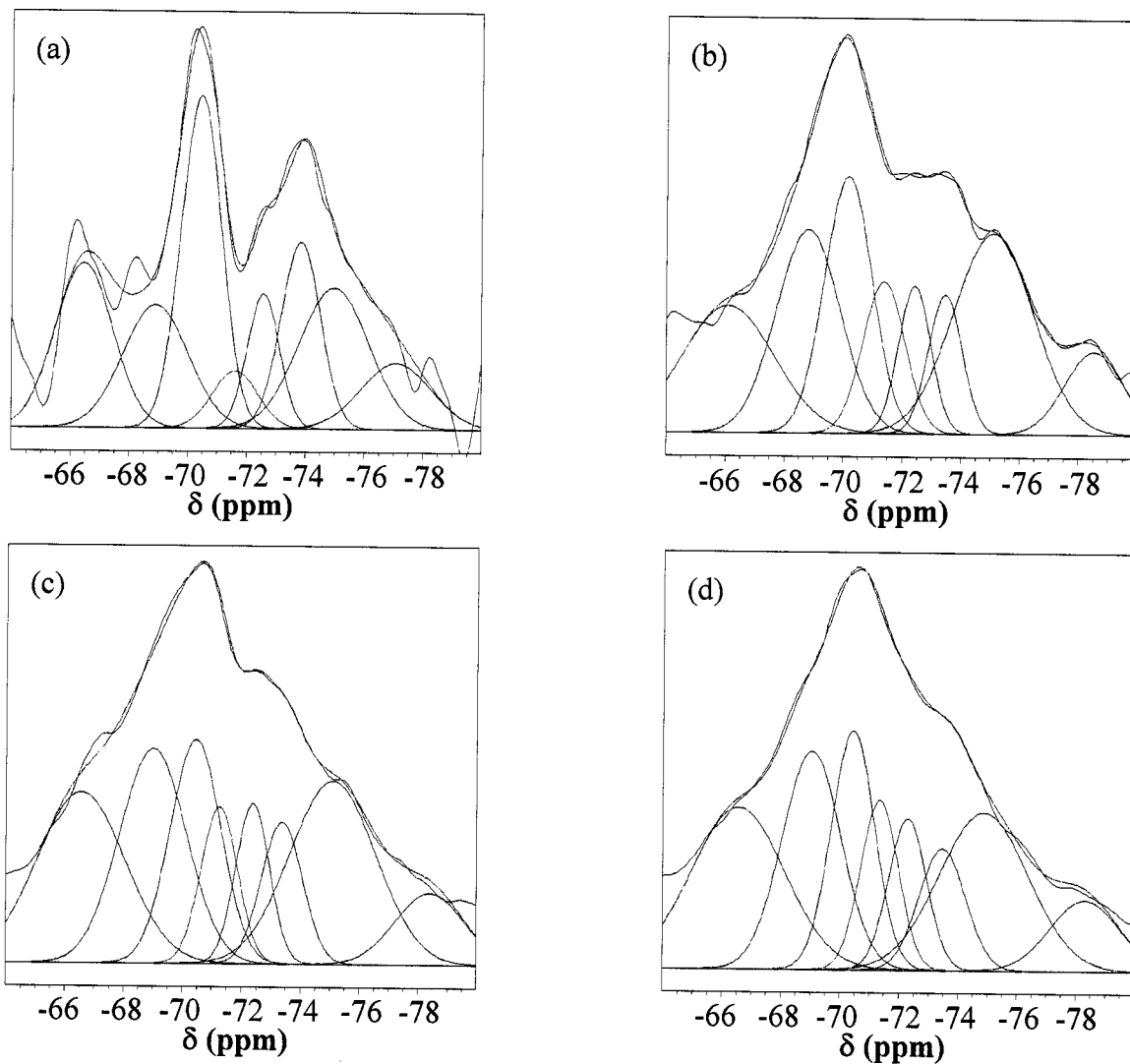


Figure 2.9. Sub-spectra of the saturation recovery data for sample CAP at τ of (a) 100 μ s, (b) 300 μ s, (c) 700 μ s, (d) 1 ms, (e) 3 ms, (f) 7 ms, (g) 10 ms, (h) 30 ms, (i) 70 ms, (j) 100 ms, (k) 300 ms, (l) 1 s, and (m) 3 s, illustrating the superposition of the fitted peaks forming the C_3S (red) and C_2S (green) contributions resulting from deconvolution.

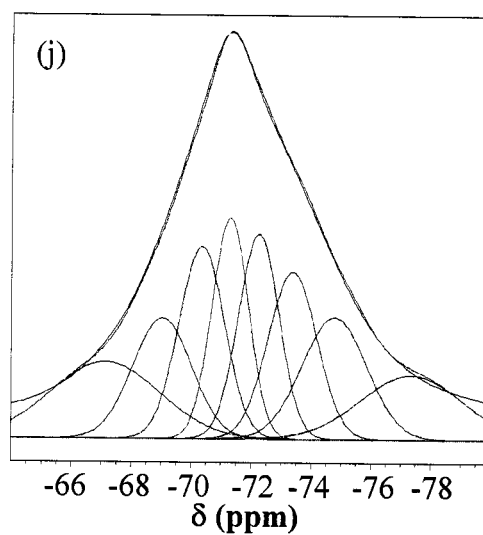
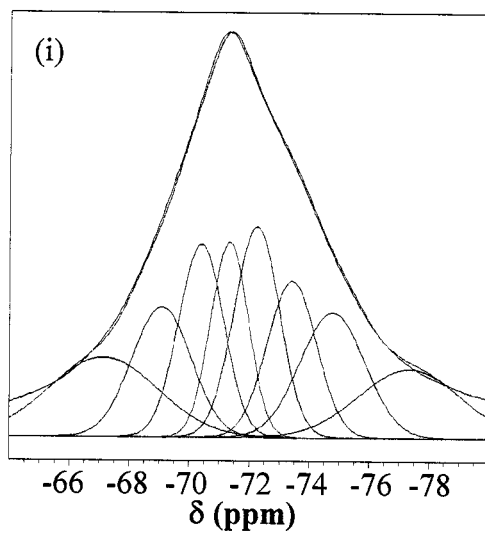
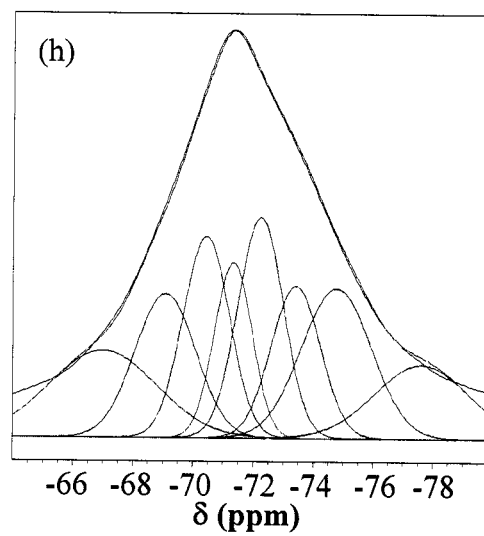
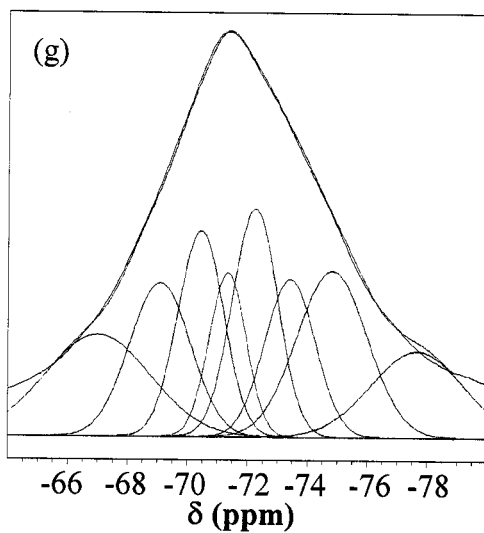
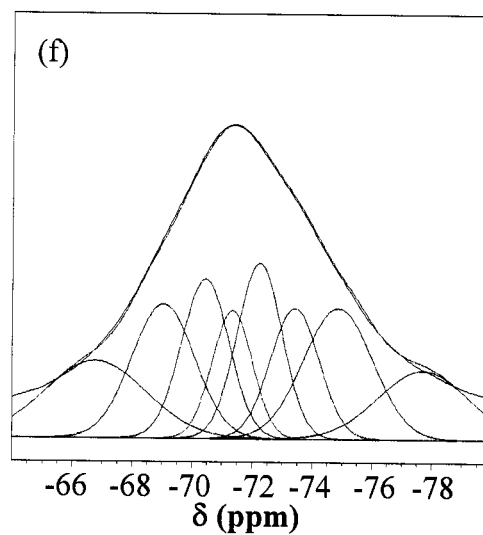
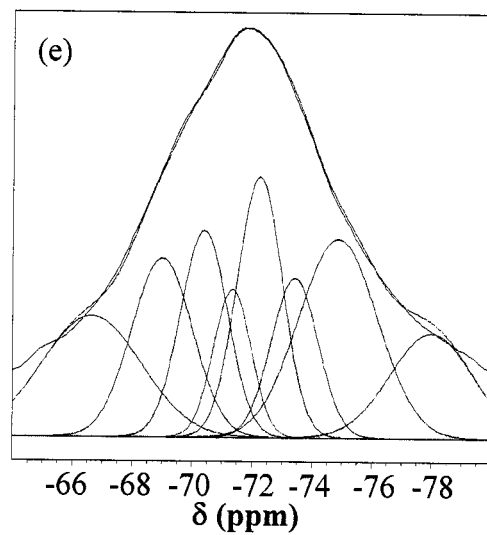
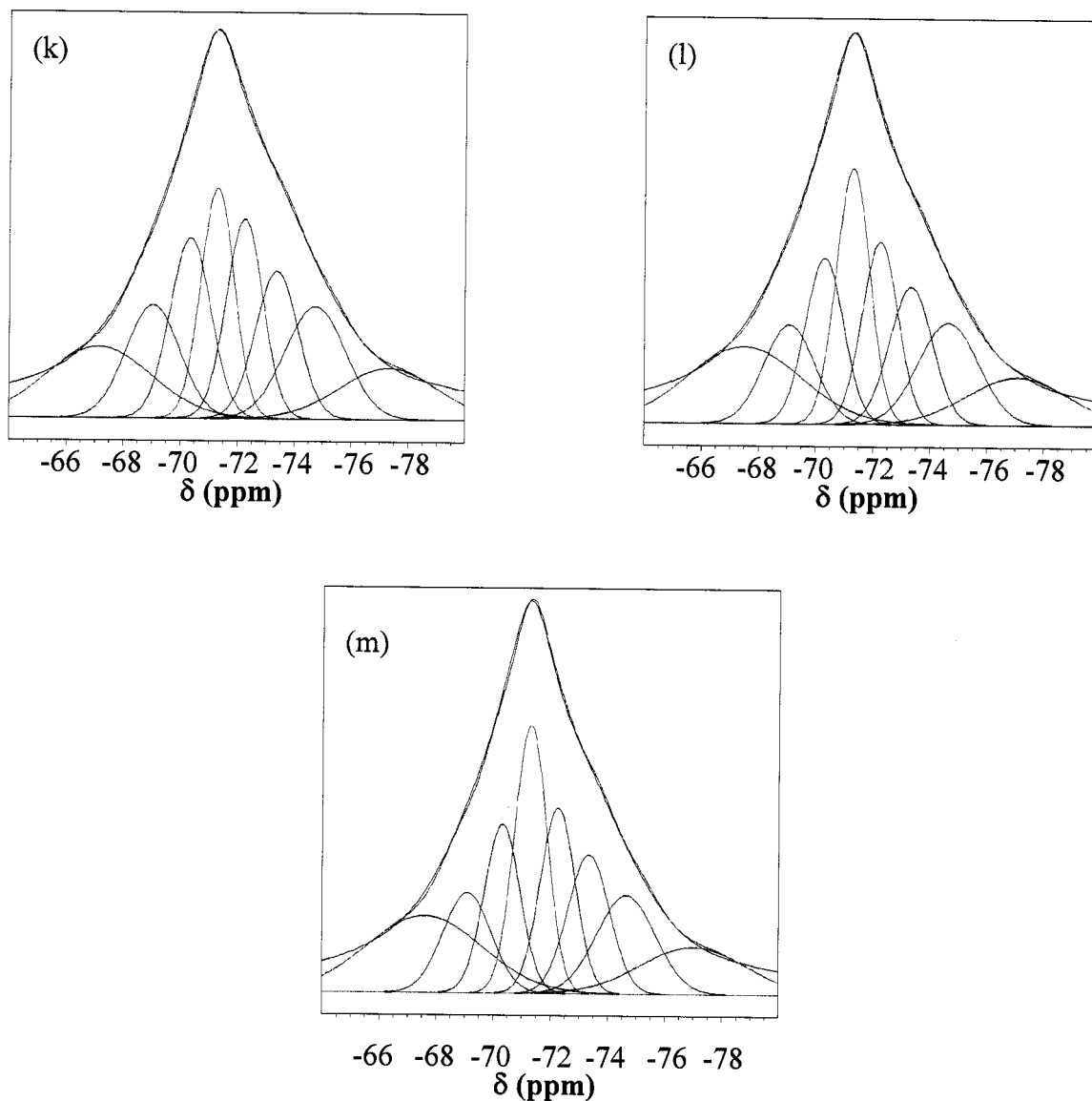
Figure 2.9 cont'd.

Figure 2.9 cont'd.



In order to correlate the data from one set to another, overlapping values of τ are selected and used to find average ratios between extreme and intermediate data sets. The collected data is given in Table 2.2. Figure 2.11 shows a plot of the rescaled data illustrating the unification of the series.

Though the disparate time regimes afford a better chance at observation of relaxation behavior, the region of greatest change is found ultimately to be in the

medium- τ regime, where τ is on the order of single to hundreds of milliseconds. Derivative analysis may be applied to this region to identify critical points on the graph, subject to the limits of resolution of the curve. To this end, simple first and second derivatives with respect to the common logarithm of τ may be estimated at a given value of τ by calculating the average of the slopes leading left and right of said point in the next lowest order graph. The x-intercept of the second derivative curve corresponding to the global maximum of the first derivative curve identifies the point of greatest change in the initial intensity function, τ_{char} . Figures 2.12 and 2.13 show the derivative curves for the medium- τ regime of the exemplar sample for the C_3S and C_2S components, respectively. Applying the above standard to the data in Figures 2.12 and 2.13 yields characteristic times of 36 ms for C_3S and 74 ms for C_2S after taking the antilogarithms of the intercepts.

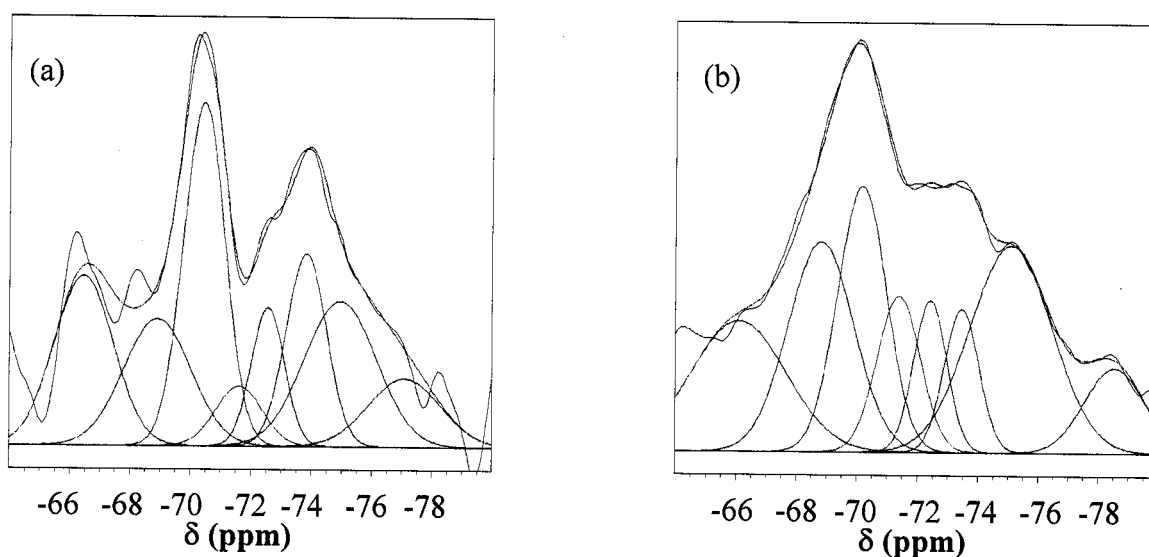


Figure 2.10. Sub-spectra of the saturation recovery data for sample CAP at τ of (a) 300 μs , (b) 700 μs , (c) 1 ms, (d) 3 ms, (e) 7 ms, (f) 10 ms, (g) 1 s, (h) 3 s, (i) 7 s, (j) 10 s, (k) 30 s, and (l) 70 s, illustrating the superposition of the fitted peaks forming the C_3S (red) and C_2S (green) contributions resulting from deconvolution.

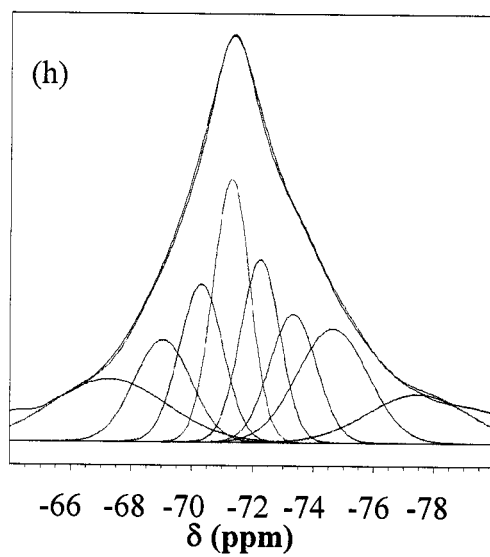
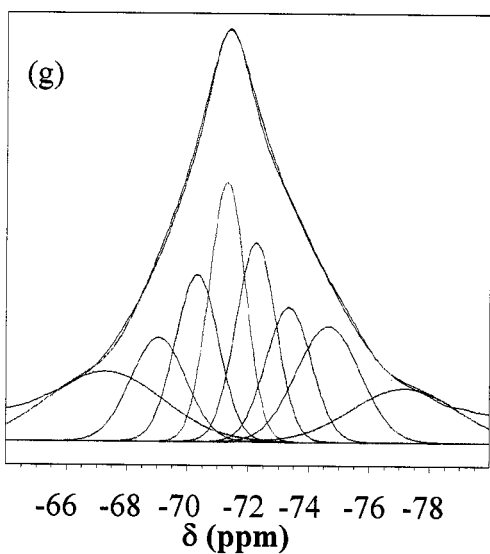
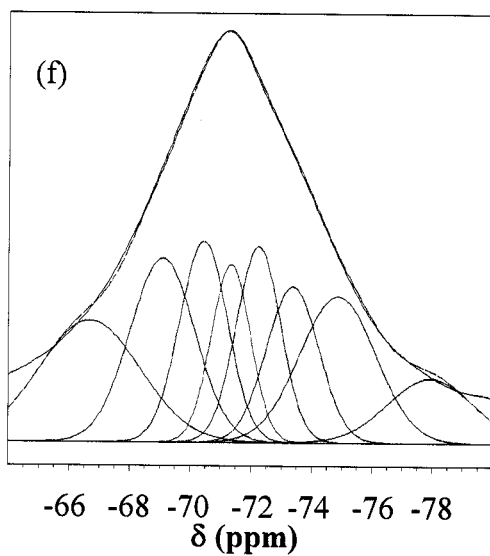
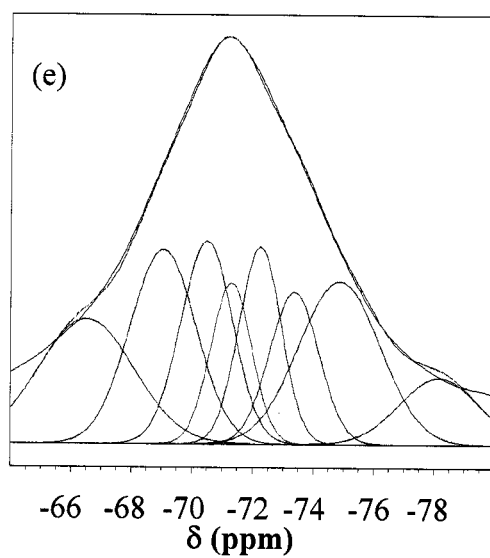
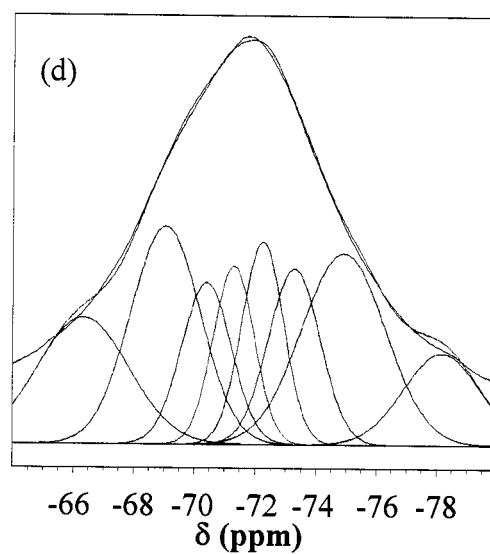
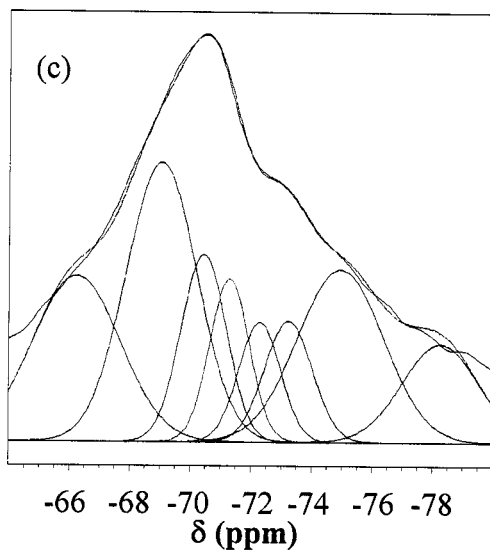
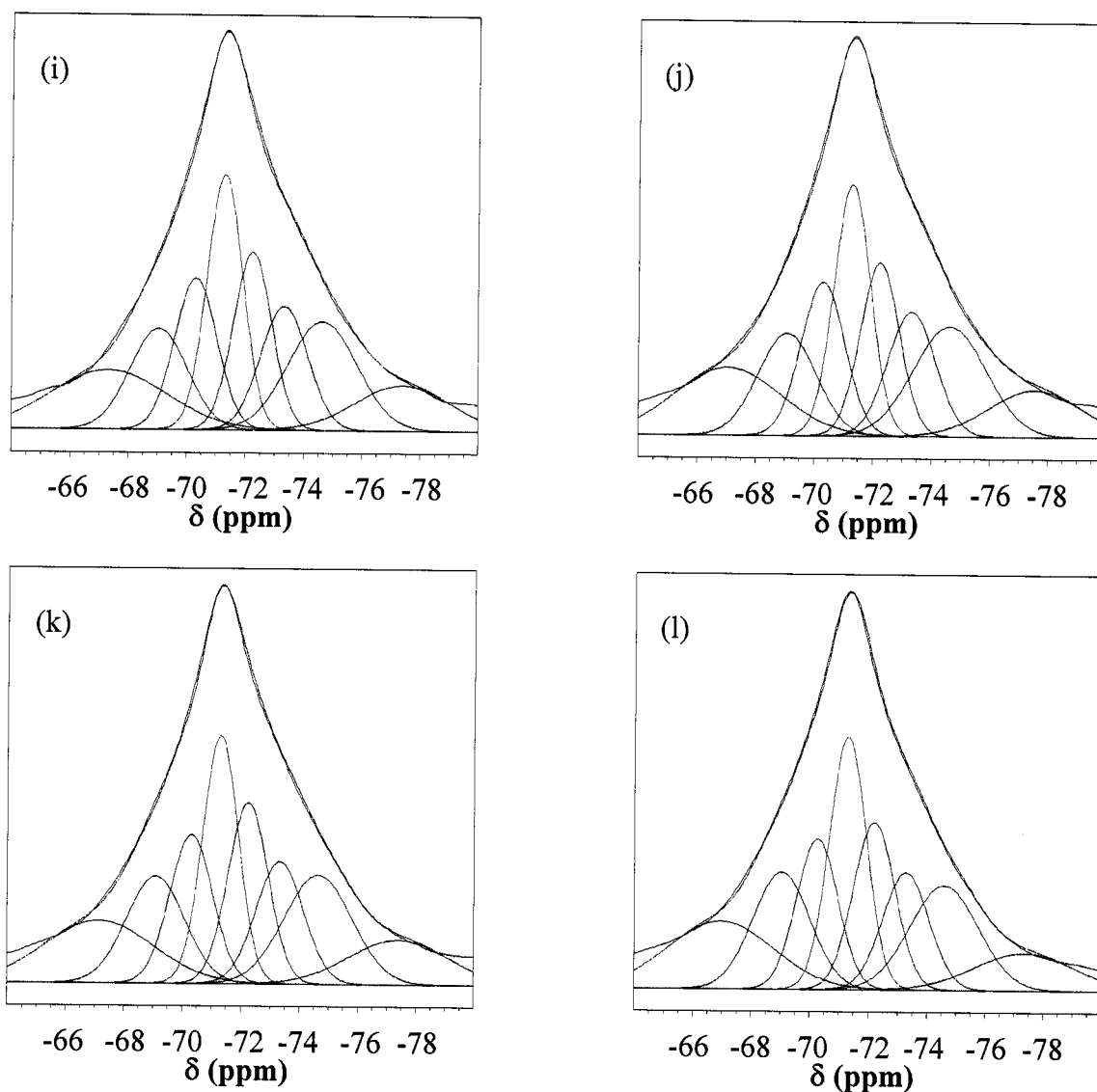
Figure 2.10 cont'd.

Figure 2.10 cont'd.

Having obtained a full saturation recovery curve of cement, deconvolved the signal into individual components, performed derivative analysis on the regions of greatest change in the individual components, and standardized for disparate relative intensities among different acquisition regimes, there now has been found a full characterization of the relaxation behavior.

Table 2.2. Processed deconvolution data from CAP saturation recovery experiments.

τ^a	Aliquot	C ₃ S area ^b	C ₂ S area ^b	C ₃ S/C ₂ S area ratio
100 μ s	1	202290037.4	9265950.67	21.83154698
300 μ s	1	611906609.3	58015759.08	10.54724818
700 μ s	1	1332946612	104992819.6	12.69559782
1 ms	1	1770911561	164778021.7	10.74725588
1 ms	2	10535829174	893374367.6	11.79329692
3 ms	1	4468713517	327496167	13.64508647
3 ms	2	25683154738	2482057772	10.34752496
7 ms	1	9552959170	858812883.4	11.12344651
7 ms	2	47182092925	4443310535	10.61868005
10 ms	1	9552959170	858812883.4	11.12344651
10 ms	2	58114533149	6010770237	9.668400364
30 ms	1	16012957734	1695664777	9.443468989
70 ms	1	20539462783	2634809641	7.795425698
100 ms	1	21930141454	3207932589	6.836222659
300 ms	1	25264567156	4156251695	6.078690371
1 s	1	25708504866	5011852595	5.129541299
1 s	2	2031695637	397032550.5	5.117201688
3 s	1	25731329115	5192454848	4.95552294
3 s	2	1993516859	420325357.5	4.742794656
7 s	2	2005679975	420353390.4	4.771413816
10 s	2	2065699229	420717131.5	4.909947978
30 s	2	2033206930	407086244.9	4.994536061
70 s	2	2007320582	435101172.2	4.613457078

^a First aliquot with central τ values, second aliquot with extreme τ values. ^bArea calculated by multiplying peak intensity (arbitrary units) by peak half-width (Hz) without rescaling to connect intermediate and extreme τ regimes.

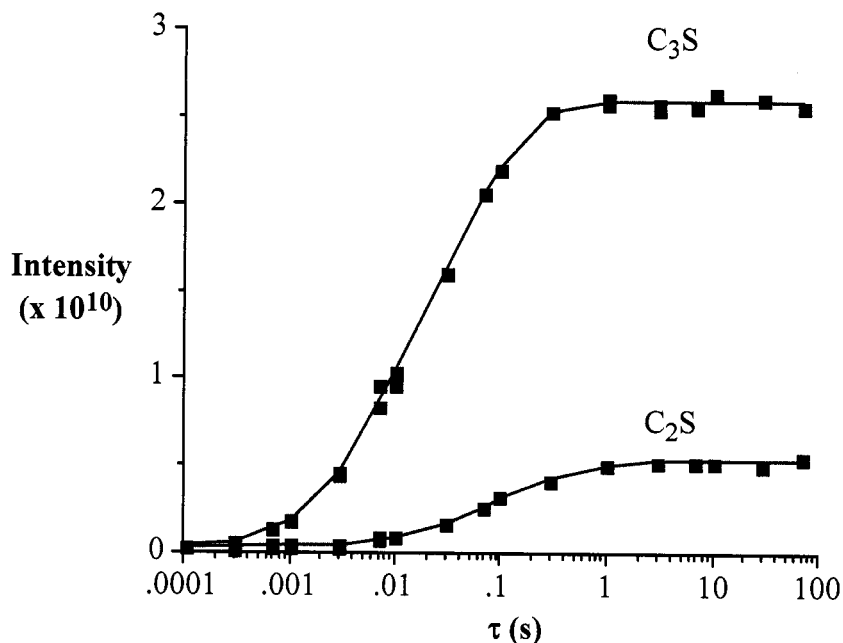


Figure 2.11. Rescaled extreme τ data sets combined with intermediate τ data for CAP. The three series are shape coded for short (\blacksquare), medium (\blacksquare), and long (\blacksquare) τ data for C_3S and C_2S .

Bloch decay experiment. In the interest of finding a simple experiment that can be used readily by a technician to evaluate the properties of a particular sample of cement, the concept of the variable delay Bloch decay experiment is developed as a screening tool to identify simple experiments with useful delays. Figure 2.14 shows the pseudo-2D variable delay Bloch decay spectrum of CAP. It is noteworthy that unlike the saturation recovery spectrum, this data set never fades into the baseline noise. The time required to collect the FID (in this case *ca.* 30 ms) for each sub-spectrum provides a firm limit to the lowest relaxation period able to be observed.

Conclusions

Three methods of NMR relaxation have been examined and compared. Inversion recovery, while desirable for most compounds, has severe limitations when examining

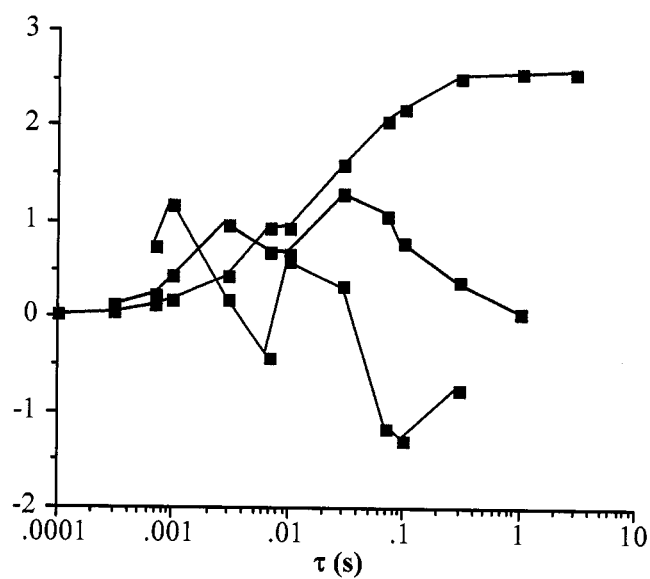


Figure 2.12. Derivative analysis of the C_3S component for the medium- τ regime of sample CAP. The three series are shape coded for the intensities of the base function (■), first derivative (●), and second derivative (▲).

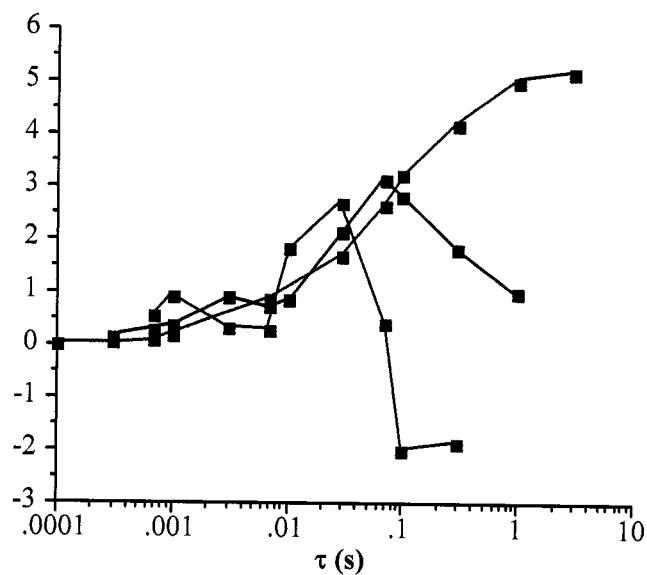


Figure 2.13. Derivative analysis of the C_2S component for the medium- τ regime of sample CAP. The three series are shape coded for the intensities of the base function (■), first derivative (●), and second derivative (▲).

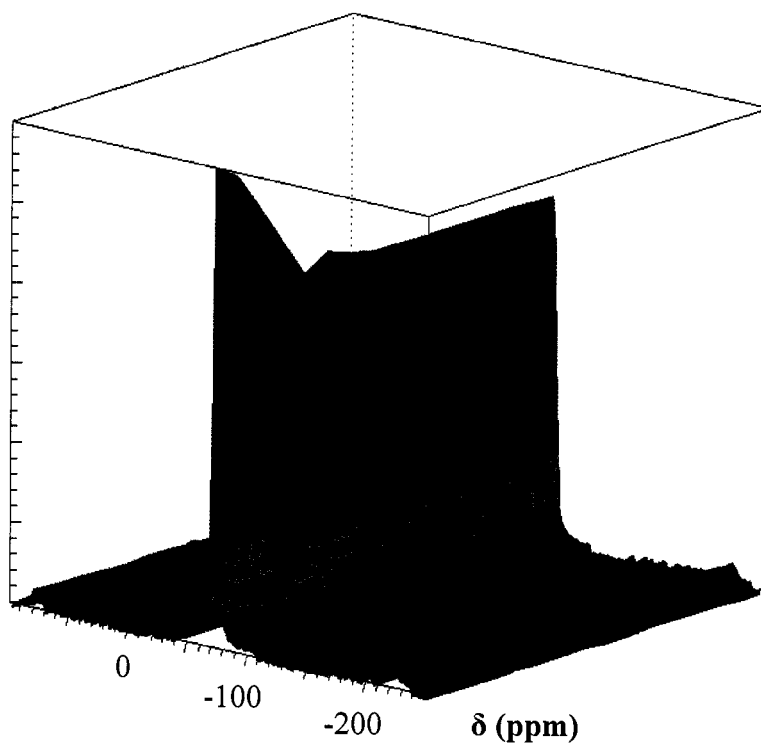


Figure 2.14. Variable delay Bloch decay spectrum of cement sample CAP.

cements. Variable delay Bloch decay experiments offer a simple experimental setup, but obscure behavior most characteristic of surface behavior. Saturation recovery provides the best balance of theoretical simplicity and spectral tractability with minimal disadvantage. Table 2.3 contains a summary of the advantages and disadvantages of the three methodologies. For the purposes of the remainder of this thesis, the focus will remain on the saturation recovery technique.

Experimental

Solid state ^{29}Si MAS NMR spectra were collected on a Bruker Avance 200 spectrometer at 39.76 MHz. Samples were measured using a 7 mm extended VT MAS probe with 7 mm long-barrel ZrO_2 rotors and plugs and Kel-F fluoropolymer caps. Chemical shifts were referenced to hexamethylcyclotrisiloxane ($\delta = -9.66$ ppm) by

sample replacement. All spectra were collected at a magic angle spinning speed of 6.00 kHz without high power ^1H decoupling. Spectra were acquired using a 90° ^{29}Si pulse of 5.75 μs and a spectral width of 14,750 Hz unless otherwise specified. Data was acquired either with Bruker Biospin's XWINNMR v2.6 or TopSpin v1.3.

Variable delay Bloch decay spectra were collected for 20480 scans over a spectral width of 15 kHz. Data was processed using TopSpin version 1.3. Fourier transforms were applied without line broadening, phase corrections were made manually, and a fifth order polynomial was fit to the baselines across the F_2 dimension.

Table 2.3. Summary of data analysis methodologies.

Method	Advantages	Disadvantages
Inversion recovery	Tight control over net magnetization vector, simple pulse sequence	Overlapping positive and negative peaks, spectrum algebra thwarted by too similar T_1 values, very time-intensive
Saturation recovery	No negative signals, simple conceptualization of data, accessible to deconvolution	Optimization of saturation pulse train required, narrower range of signal intensities possible
Variable delay Bloch decay experiments	Simplest experimental setup, translates best into standardized testing	Fundamental lower limit on accessible relaxation regimes

T_1 relaxation times measured *via* the standard inversion recovery method were collected initially over a telescoping range of mixing periods τ primarily varying over a millisecond time regime from 1 μ s (approximating a value of 0 seconds to accommodate pulse program timing considerations) terminating at 1.5 s for 20000 scans at each value of τ with a relaxation delay of 6 seconds. After initial processing of data, the times closest to exhibiting a null-crossing of the C_2S were identified and subsequent inversion recovery runs were carried out over the proper time regime to identify the null-crossing time to the nearest 1 ms. Data was processed with Topspin v1.3. Fourier transforms were applied without line broadening, phase corrections were made manually, and a fifth order polynomial was fit to the baselines across the F_2 dimension.

T_1 relaxation times measured *via* the saturation recovery method were collected initially over a telescoping range of 16 mixing periods τ primarily varying over a microsecond and millisecond time regime from 1 μ s (approximating a value of 0 seconds to accommodate pulse program timing considerations) terminating at 3.0 s for 128 dummy scans and 40000 acquisition scans at each value of τ , with a 400-pulse saturation train with a 2 μ s interstitial period and no relaxation delay. A second aliquot of sample was analyzed under time regimes of 1 to 70 s for 5000 scans and from 70 μ s to 10 ms for 200000 scans. Otherwise, these additional saturation recovery experiments were performed under conditions identical to the first run. Data was processed using TopSpin version 1.3. Fourier transforms were applied without line broadening, phase corrections were made manually, and a fifth order polynomial was fit to the baselines across the F_2 dimension. The data was then split into sub-spectra corresponding to individual values of τ for deconvolution analysis.²

Deconvolutions were carried out using a SIMPLEX routine integrated into the solids lineshape analysis tool in TopSpin v1.3 with eight Gaussian peaks, and at least two optimizations of 1000 iterations each. Linewidths and intensities of all peaks were free to be altered by the optimization independently, but no Lorentzian character was permitted).

The SIMPLEX routine otherwise used default parameters. After the first lineshape was attempted by visual inspection and optimized, the parameters were copied into subsequent data sets to be used as a starting point for optimization after adjustments for peak intensities by visual inspection. Seven of the eight peaks were attributed to C_3S , while the remaining peak at *ca.* -71.4 ppm was attributed to C_2S solely. Skibsted *et al.* used thirteen peaks for their analysis of similar lineshapes, with relative intensities of the twelve C_3S Gaussian and/or Lorentzian peaks fixed,³ but the work presented herein found seven peaks sufficient to fit the C_3S portion of the lineshape in the samples studied.

Areas of fitted peaks are calculated by multiplying the half-widths (in Hz) of the fitted peaks by their respective heights (in self-consistent arbitrary units). The C_3S content is calculated from the sum of the seven peak areas attributed to C_3S . In order to compare data from runs with differing numbers of scans, the areas from sub-spectra with matching values of τ are divided and the average ratio is used as a scaling factor, which is then applied to the data set of more extreme τ values.

References

- ¹ G. B. Furman and S. D. Goren. *J. Phys.: Condens. Matter*, 2002, **14**, 873.
- ² J. A. Chudek, G. Hunter, G. W. McQuire, C. H. Rochester, and T. F. S. Smith, *J. Chem. Soc., Faraday Trans.*, 1996, **92**, 453.
- ³ J. Skibsted, H. Jakobsen, and C. Hall, *J. Chem. Soc., Faraday Trans.*, 1995, **91**, 4423.

Chapter 3

Correlations of NMR Measurements with Cement Performance Property Measurements

Introduction

As noted in the Introduction, cement hydration is a very complex process, not solely dictated by simple solvation and reprecipitation. The prediction of the set kinetics, reaction to inhibitors, and the properties of the set cement, is presently not available. Instead of prediction, a series of experiments must be performed on each sample to obtain the property information required. It would be desirable to have a simple analytical method (or short series of methods) that would allow for the prediction of the chemistry of individual samples of cement from various sources. In this regard an attempt was made to correlate data from a wide range of spectroscopic and analytical techniques with experimental data obtained by traditional methods. The ultimate goal of this project is the development of a tool for the prediction of the hydration chemistry of various cements based upon their chemistry.

Based upon the work in Chapters 1 and 2 it is proposed that solid state ^{29}Si NMR analysis of cement samples will provide a measure of the relative ratio of C_3S and C_2S that is available during the hydration process. This measurement, if oblique is termed the “active concentration”, i.e., the amount of mineral available to reaction as opposed to the bulk concentration, and is related to the critical values of the derivative curves identified by the means outlined in the preceding chapter. Additionally, correlations may be observed with the measured “bulk” silicate content. In the preceding chapter it was demonstrated that the saturation recovery method for analysis of ^{29}Si NMR data offers the best combination of accuracy, speed, and ease of processing.

If there is to be an application of NMR as a tool for guiding downhole applications of cement then it is necessary to demonstrate whether there exist predictive

correlations and for which parameters. In this chapter we will investigate the existence of correlation between the C_3S/C_2S ratio, C_3S and C_2S concentrations, and the characteristic times from derivative analysis, as obtained by the saturation recovery method, with a range of downhole simulation performance parameters typically measured for downhole cements. An additional important issue will be the necessity of comparing the extent of experimentation required for an NMR method versus present analytic methods as well as an analysis of errors and assumptions inherent in the technique. These issues will be discussed in Chapter 4.

Various attempts in the past have been made to correlate engineering performance properties with more conventional spectroscopic analyses. Barnes and co-workers were able to identify several key factors to the role of gypsum in preventing “flash set” by means of time-resolved in situ X-ray diffraction.¹ Parrott and co-workers applied a series of different tests, including quantitative X-ray diffraction and conduction calorimetry, to attempt correlations with degree of hydration.² Vlachou and Piau conducted a study of additive response and its correlations with SEM.³ Ghosh and Handoo reviewed the progress in using infrared and Raman spectroscopies to monitor cement hydration behavior.⁴ Coveney, Fletcher, and co-workers were able to build on the existing infrared knowledge base by applying artificial neural net (ANN) analysis to diffuse reflectance (DRIFTS) spectra of cements.^{5,6}

Results and Discussion

In the present study eight different cements were studied. Each sample was stored in a dry box under argon prior to NMR analysis. Three of the samples are API Class G cements from foreign countries: Brazil (BRZ), Russia (RUS), and Thailand (THA). The remaining five samples are API Class H cements from domestic cement manufacturers: Lafarge (Joppa plant) (JOP), Texas Industries (TXI), El Toro (ELT), Southdown (SDN) and Capitol (CAP). Class G and H cements both use the same specifications for

elemental composition and restrict grinding aids to gypsum, but differ with respect to fineness, with class G cements being the more finely ground of the two. Figure 3.1 shows a world map marked with approximate locations of the origins of cements.

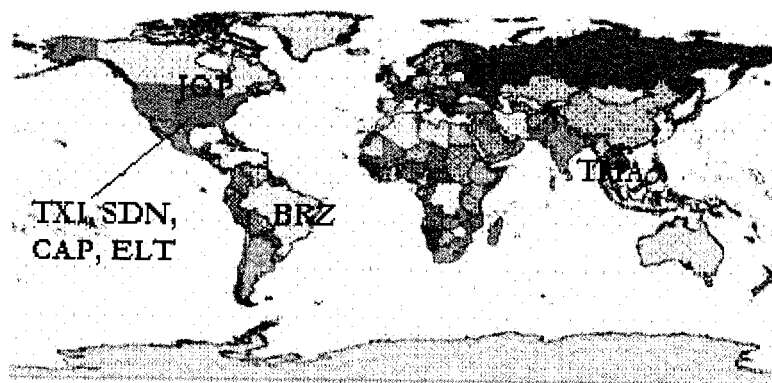


Figure 3.1. World map labeled with approximate locations of origin for cements studied.

Physical measurements. In a typical series of experiments that must be performed on a given cement sample to match it to the specifications of a particular cementing job, there are 4 key measurements: thickening time determination in a consistometer, ultrasonic analysis of compressive strength development, Young's modulus, and crush strength (the latter two obtained from destructive mechanical testing). However, irrespective of the final analytical process, the Portland cement samples must be hydrated and set while measurements are performed.

Cement slurries are mixed by independently weighing each component, dry blending the dry additives into the cement powder, and mixing the water and wet additives in a blender at low shear. The cement is then added to the liquid under low to moderate shear within 10-15 seconds. The mixture is then blended under maximum shear conditions for 35 seconds, with the operator scraping the sides of the blender to incorporate caked cement powder on the sides of the vessel.

For the purpose of evaluating a manageable data set, three different cement formulations were prepared with each cement sample. All cement formulations are based

on a nominal 16.4 lb/gal slurry achieved by mixing cement with 39.4% water by weight of cement (bwoc). The first slurry considered was prepared without additives. The second formulation added a lignosulfonate retarder at a loading of 0.5 % bwoc. The third and final formulation added to the base cement a copolymer of N,N-dimethylformamide and 2-acrylamido-2-methylpropane sulfonic acid, a fluid loss additive used in oilwell cement formulations, at a loading of 0.15 % bwoc.

Thickening time, i.e., the time between initial mixing and an apparent viscosity of 70 Bearden consistency units (Bc) at a given temperature ($<180^{\circ}\text{F}$), is measured on an atmospheric consistometer (Figure 3.2). Approximately 500 mL of slurry is stirred with a special paddle at 150 rpm in a thermostatted canister. The test is designed to simulate pumping conditions to determine the time frame within which the slurry may be pumped before setting. For simulation of hotter wells under high pressure, the high-temperature high-pressure (HTHP) consistometer may be used (Figure 3.3). It operates under analogous conditions to give similar data.

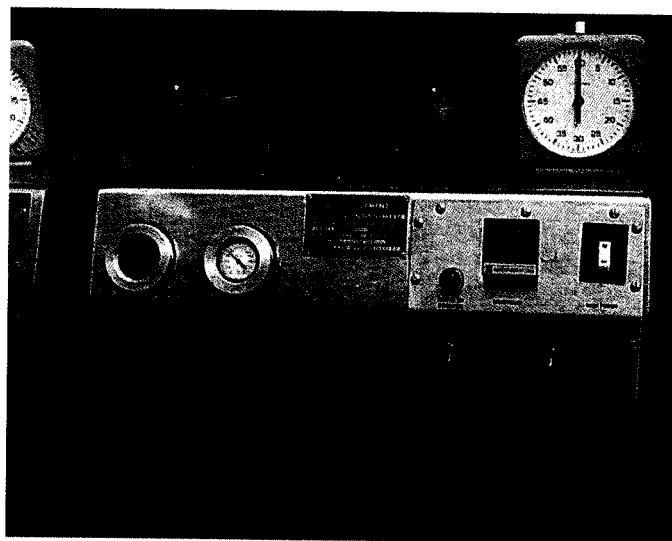


Figure 3.2. Atmospheric consistometer (Halliburton Energy Services).

Compressive strength development is measured directly via conventional destructive mechanical testing, or indirectly and non-destructively in real time with the Ultrasonic Cement Analyzer (UCA) (Figure 3.4). The UCA sends ultrasonic pulses between two transducers through a cylinder of cement setting at a given temperature under a given hydrostatic pressure. At a given time, the velocity of the pulse correlates to the compressive strength of the cement.⁷



Figure 3.3. High temperature high pressure (HTHP) consistometer (Halliburton Energy Services).



Figure 3.4. Ultrasonic cement analyzer (UCA) (Halliburton Energy Services).

NMR measurements. The NMR data that served as the basis for correlations came from the saturation recovery experiments, as described in Chapter 2. Table 2.2 and Tables 3.1-3.7 tabulate the processed peak areas attributed to the C_2S and C_3S content evident in each sample, as well as the derived C_3S/C_2S ratio. Table 3.8 lists the characteristic times for each sample as identified in the derivative analysis. Error analysis for cement relaxation data is described in Chapter 4.

Correlations for cement. Initial studies were attempts to find a correlation between the C_3S/C_2S ratio and the physical measurements on cements in the absence of additives. Though cements are never used downhole without additives, it remains instructive to consider the impact of varying degrees of accessible mineral on unperturbed hydration reactions without the added complication of the action of additives. Once a baseline understanding of the hydration correlations is established, one may evaluate the impact of additive response on the correlations within the context of the simplified system.

It is worth noting that the sample JOP gives data substantially inconsistent with other cement's behavior, whether with or without the presence of additives. This anomalous behavior is always consistent with a more slowly hydrating paste. The expected cause for the erroneous behavior is premature hydration, which can act to moderately passivate the cement particles when exposed to more typical amounts of water. Error analysis of physical testing and the relative impact of premature hydration and aging on samples when analyzed via NMR are addressed in Chapter 4.

Table 3.9 shows the thickening time data for the cements studied without additives, Table 3.10 shows the UCA data for the cements studied without additives, and Table 3.11 shows the destructive mechanical testing data for the cements studied without additives. The data contained in Table 2.2 and Tables 3.1-3.8 may be plotted against the data in Tables 3.9-3.11 to graphically evaluate possible correlations.

Table 3.1. Processed deconvolution data from TXI saturation recovery experiments.

τ^a	Aliquot	C ₃ S area ^b	C ₂ S area ^b	C ₃ S/C ₂ S area ratio
1 ms	2	9593377244	1053406360	9.10700524
3 ms	2	25480134750	2067831458	12.32215259
7 ms	1	5972105050	900959314.7	6.628606811
7 ms	2	47616808858	6800188236	7.002278056
10 ms	1	7273731463	1113303485	6.533466896
10 ms	2	60713041928	7871929203	7.712600096
30 ms	1	12734009876	2301889946	5.531980319
70 ms	1	17450127110	3607119078	4.837690891
100 ms	1	18789523252	4223506575	4.44879697
300 ms	1	24703416705	6563149012	3.76395792
1 s	1	24256303331	7701256535	3.149655283
1 s	2	2567415522	717811273.6	3.576727779
3 s	1	24947024554	8112670181	3.07506949
3 s	2	2595416645	797205558.5	3.255642936
7 s	2	2681297489	722376180.4	3.711774504
10 s	2	2701026343	675202654.4	4.000319497
30 s	2	2691042579	719788831.6	3.738655645
70 s	2	2721050244	702758733.9	3.871955072

^a First aliquot with central τ values, second aliquot with extreme τ values. ^bArea calculated by multiplying peak intensity (arbitrary units) by peak half-width (Hz) without rescaling to connect intermediate and extreme τ regimes.

Table 3.2. Processed deconvolution data from THA saturation recovery experiments.

τ^a	Aliquot	C ₃ S area ^b	C ₂ S area ^b	C ₃ S/C ₂ S area ratio
1 ms	1	1760770941	115087585.6	15.2993994
1 ms	2	12854254373	570317889.4	22.5387536
3 ms	1	4163448065	366667539.7	11.3548313
3 ms	2	28949060289	2741882831	10.5580953
7 ms	1	7290172162	971400342.4	7.50480707
7 ms	2	53373936400	5331137711	10.0117347
10 ms	1	8983451975	1130162832	7.94881208
10 ms	2	64466909028	6257465622	10.3023992
30 ms	1	14834718540	2021235696	7.33943032
70 ms	1	19061159485	2449978281	7.78013407
100 ms	1	20024170464	2720638031	7.36010092
300 ms	1	21617701723	3727505757	5.79950861
1 s	1	22346468089	3950864090	5.65609638
1 s	2	2061699553	355440055	5.80041423
3 s	1	22139151016	4117270048	5.37714329
3 s	2	2066855161	345021364.5	5.99051356
7 s	2	2143670770	318558399.2	6.72928661
10 s	2	2093857090	336844364.6	6.21609654
30 s	2	2095346660	393152524.2	5.32960246
70 s	2	2193951345	402956169.8	5.44464016

^a First aliquot with central τ values, second aliquot with extreme τ values. ^bArea calculated by multiplying peak intensity (arbitrary units) by peak half-width (Hz) without rescaling to connect intermediate and extreme τ regimes.

Table 3.3. Processed deconvolution data from SDN saturation recovery experiments.

τ^a	Aliquot	C ₃ S area ^b	C ₂ S area ^b	C ₃ S/C ₂ S area ratio
1 ms	1	1522028060	352253718.2	4.320828941
1 ms	2	7019115703	942160222.7	7.450023398
3 ms	1	3913182045	763805200.4	5.123272324
3 ms	2	9799473820	1182131030	8.289668044
7 ms	1	7151126064	1236888243	5.781545829
7 ms	2	28672700416	3533999021	8.113386633
10 ms	1	9039019930	1321658626	6.839148741
10 ms	2	52733512692	6471791127	8.148209925
30 ms	1	14534552559	2453629436	5.923695056
70 ms	1	17952746559	3383784791	5.305522564
100 ms	1	19113675718	3786686879	5.047598687
300 ms	1	21395860646	4058763397	5.271522026
1 s	1	22303631419	4511532769	4.943692656
1 s	2	1991385571	401293869.3	4.962412147
3 s	1	22346486839	4462667931	5.007427661
3 s	2	1973427181	398012635.6	4.95820234
7s	2	1956724801	390448547	5.011479275
10 s	2	1930807907	402258152.4	4.799922378
30 s	2	1901487655	377267339.2	5.040159741
70 s	2	1979591848	338516467.2	5.847845053

^a First aliquot with central τ values, second aliquot with extreme τ values. ^bArea calculated by multiplying peak intensity (arbitrary units) by peak half-width (Hz) without rescaling to connect intermediate and extreme τ regimes.

Table 3.4. Processed deconvolution data from RUS saturation recovery experiments.

τ^a	Aliquot	C ₃ S area ^b	C ₂ S area ^b	C ₃ S/C ₂ S area ratio
1 ms	1	1217031466	203281844	5.986916699
1 ms	2	7872536165	805579398.3	9.772514269
3 ms	1	3346245346	406462657.1	8.232602154
3 ms	2	29551958978	3251557042	9.08855622
7 ms	1	6522577476	810687026.9	8.045740537
7 ms	2	50833052890	5463047081	9.304890135
10 ms	1	8266365004	878205029.5	9.412796246
10 ms	2	66109511407	7132484403	9.268791584
30 ms	1	14249640812	1511334575	9.428515068
70 ms	1	18196848312	1982310683	9.179614714
100 ms	1	20160573377	2372017975	8.499334148
300 ms	1	23181408425	3147425731	7.365196325
1 s	1	24061325967	3662932122	6.568870284
1 s	2	2428677883	372495448.4	6.520020293
3 s	1	24190259828	3810073460	6.349027146
3 s	2	2459091132	408261364.4	6.02332561
7 s	2	2447985517	394160577.6	6.210630023
10 s	2	2432246798	399737008	6.08461751
30 s	2	2422714988	383122870.2	6.323597926

^a First aliquot with central τ values, second aliquot with extreme τ values. ^bArea calculated by multiplying peak intensity (arbitrary units) by peak half-width (Hz) without rescaling to connect intermediate and extreme τ regimes.

Table 3.5. Processed deconvolution data from JOP saturation recovery experiments.

τ^a	Aliquot	C ₃ S area ^b	C ₂ S area ^b	C ₃ S/C ₂ S area ratio
300 μ s	1	302739092.6	10509227.51	28.80697866
300 μ s	2	760575939.8	32446664.7	23.44080499
700 μ s	1	899906157.8	79394781.75	11.33457562
700 μ s	2	3657387998	528046867.2	6.926256409
1 ms	1	1278906502	129222018.4	9.896970479
1 ms	2	6029025812	638766195.5	9.43854865
3 ms	1	3056409474	301445972.3	10.13916176
3 ms	2	18475297414	2178678171	8.480048894
7 ms	2	36484381457	4643263548	7.857486676
7 ms	1	5875735314	645399902	9.10402263
10 ms	1	7329658094	807908018.7	9.072391812
10 ms	2	47680986798	5796285086	8.226128648
30 ms	1	13433536865	1554972365	8.639083993
70 ms	1	18218155754	2200941051	8.27743921
100 ms	1	20796775148	2530595184	8.218135908
300 ms	1	25323853717	3197606353	7.919628285
1 s	1	27811426207	3841346508	7.240020173
1 s	2	2320147133	311595088.8	7.446032419
3 s	1	28448935935	3902824750	7.28931934
3 s	2	2319360364	317620692.2	7.302296168
7 s	2	2396311558	332788115.4	7.200712546
10 s	2	2390099138	336433917.5	7.104215756
30 s	2	2347104221	328337302.2	7.148454367
70 s	2	2288973366	315790193.1	7.248399145

^a First aliquot with central τ values, second aliquot with extreme τ values. ^bArea calculated by multiplying peak intensity (arbitrary units) by peak half-width (Hz) without rescaling to connect intermediate and extreme τ regimes.

Table 3.6. Processed deconvolution data from ELT saturation recovery experiments.

τ^a	Aliquot	C ₃ S area ^b	C ₂ S area ^b	C ₃ S/C ₂ S area ratio
300 μ s	1	277427948.1	3732507.341	74.32750232
300 μ s	2	4336136371	75272026.62	57.60621264
700 μ s	1	970213555.6	74995050.14	12.93703456
700 μ s	2	10294523606	647879895	15.88955559
1 ms	1	1400499201	106858980.7	13.10605053
1 ms	2	14697401014	1055194487	13.92861809
3 ms	1	3769041703	256924920.8	14.66981752
3 ms	2	36312418929	2895386078	12.54147735
7 ms	1	6717303905	462372573	14.52790303
7 ms	2	64188409382	5221254945	12.29367462
10 ms	1	8407801991	687539825.4	12.22882178
10 ms	2	79072397166	6619454408	11.94545536
30 ms	1	13459293633	1372340042	9.807550037
70 ms	1	16795668669	2067379462	8.124134433
100 ms	1	18030281847	2309542696	7.80686232
300 ms	1	19997407286	2836874597	7.049098084
1 s	1	20264210192	3356697082	6.036949328
1 s	2	2395258863	385755171.1	6.209272207
3 s	1	20594050996	3518909855	5.852395158
3 s	2	2388943844	430322307.7	5.551522198
7 s	2	2450843012	413394230.6	5.92858543
10 s	2	2403079865	426675983.4	5.632095451
30 s	2	2417933279	432721235.9	5.587738891
70 s	2	2427642161	431492497.4	5.626151499

^a First aliquot with central τ values, second aliquot with extreme τ values. ^bArea calculated by multiplying peak intensity (arbitrary units) by peak half-width (Hz) without rescaling to connect intermediate and extreme τ regimes.

Table 3.7. Processed deconvolution data from BRZ saturation recovery experiments.

τ^a	Aliquot	C ₃ S area ^b	C ₂ S area ^b	C ₃ S/C ₂ S area ratio
300 μ s	1	307233934.5	20085965.38	15.29595062
700 μ s	1	827774190.5	51286225.81	16.14028284
700 μ s	2	4421665493	979328685.2	4.514996405
1 ms	1	1269692417	103701393.8	12.2437353
1 ms	2	6986014080	568179270.9	12.2954399
3 ms	1	2981313319	237926952.9	12.53037238
3 ms	2	18766012084	2801917178	6.697561309
7 ms	1	5384913877	574563608.8	9.372180547
7 ms	2	37132204907	4930750757	7.530740598
10 ms	1	6806549942	653295701	10.41878882
10 ms	2	49529427385	5628982694	8.799001539
30 ms	1	12106608421	1195566591	10.12625186
70 ms	1	16252998231	1638427393	9.919877014
100 ms	1	18018586353	1824485898	9.875980065
300 ms	1	21805820315	2301266338	9.475574362
1 s	1	24141665779	2662072342	9.068748959
1 s	2	2317798481	286750669.8	8.082974952
3 s	1	24774644566	2808135515	8.822453344
3 s	2	2334575361	316998473.4	7.364626512
7 s	2	2354375187	306388876.6	7.684271089
10 s	2	2343411843	312161240.5	7.507055774
30 s	2	2348358926	336692278.7	6.974792933
70 s	2	2363194752	306671128.1	7.705957736

^a First aliquot with central τ values, second aliquot with extreme τ values. ^bArea calculated by multiplying peak intensity (arbitrary units) by peak half-width (Hz) without rescaling to connect intermediate and extreme τ regimes.

Table 3.8. Characteristic relaxation times^a from derivative analysis.

Sample	C ₃ S τ_{char} (ms)	C ₂ S τ_{char} (ms)
BRZ	35.5	49.4
CAP	36.2	74.4
ELT	18.0	35.9
JOP	49.7	58.8
RUS	29.0	94.7
SDN	15.6	38.2
THA	19.9	147.2
TXI	33.7	139.4

^a τ_{char} : x-intercept of second derivative curve closest to global maximum of first derivative curve of the base intensity function.

A plot of thickening time measurements of slurries without additives versus the saturation recovery-derived silicate ratio shows essentially no correlation. This suggests that there is no significant relationship between thickening time measurements and the saturation recovery-derived silicate ratio. In contrast, as seen in Figure 3.5 there is a good agreement between compressive strength development as a function of C₃S/C₂S ratio, i.e., the time to achieve a given compressive strength of slurries, and the saturation recovery-derived silicate ratio. In agreement with conventional cement chemistry wisdom, higher C₃S content available to produce C-S-H on a short time scale results in faster strength development.

It is interesting to note that if the intensity of the individual mineral peaks is plotted against the time for strength development it is the C₂S that appears to dominate

the correlation observed in Figure 3.6. This dominance is not completely counterintuitive, however, in the sense that higher C_2S content means potentially less C_3S to readily percolate the cement slurry with C-S-H to solidify the material.

Table 3.9. Consistometry data for cements without additives.

Sample	Time to 50 Bc ^a (min.)	Time to 70 Bc (min.)	Time to 100 Bc (min.)
BRZ	53	56	63
CAP	78	95	108
ELT	90	120	134
JOP	105	123	144
RUS	69	71	79
SDN	80	96	110
THA	54	65	73
TXI	78	87	98

^a Bearden consistency units, proportional to the torque on the paddle in the rotating cup of the consistometer.

Figure 3.7 shows a plot of compressive strength development in terms of compressive strength attained by a given time of cements without additives, versus the saturation recovery-derived silicate ratio. This correlation is especially useful for field engineers at the well site trying to schedule the time after cement placement when the next phase of drilling may continue. It is interesting to note that as with strength development the correlation with compressive strength is better for earlier times.

A plot of the 72-hour crush strength measured from destructive mechanical testing versus the C_3S/C_2S ratio shows a poor correlation (Figure 3.8), but a trend of increasing crush strength with increasing C_3S/C_2S ratio is apparent. However, the large and asymmetric errors associated with measurements of crush strength makes any predictive correlation difficult at this time.

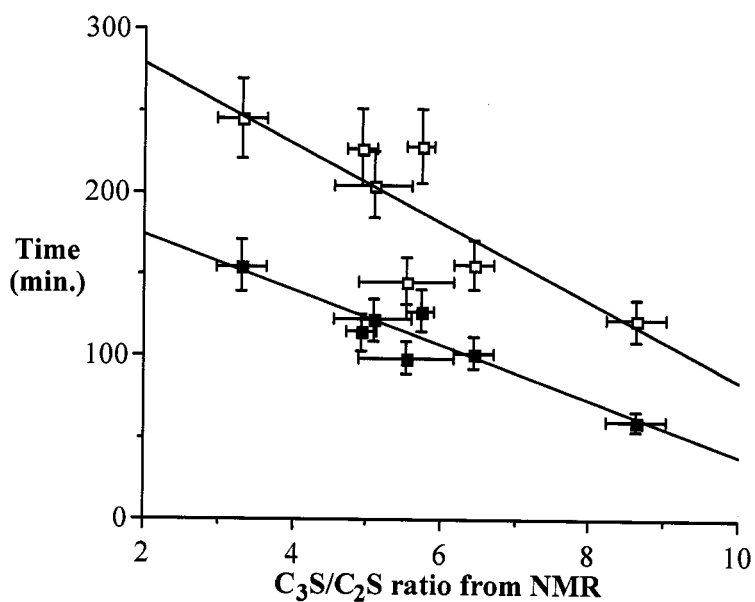
Table 3.10. Ultrasonic data for cements without additives.

Sample	Time to 50 psi (min.)	Time to 500 psi (min.)	Strength at 24 hours (psi)	Strength at 48 hours (psi)	Strength at 72 hours (psi)
BRZ	60	122	4897	5300	5428
CAP	115	228	2330	3039	3450
ELT	128	229	2877	3410	3775
JOP	129	220	2843	3556	3925
RUS	102	156	3764	4314	4610
SDN	122	205	3335	3920	4225
THA	99	146	3557	4331	4725
TXI	155	245	2258	3210	3420

In contrast to the data for strength development, the 72-hour crush strength appears to be controlled by the C_3S rather than C_2S , see Figures 3.9 and 3.10. This is not surprising, since C_3S is the mineral that reacts on a timescale of minutes or hours, rather than days, months and years, as is the case for C_2S . It is also noteworthy that the

Table 3.11. Destructive mechanical testing data for cements without additives.

Sample	72 Hour Crush Strength (psi)	Young's Modulus (psi)
BRZ	5690	799204
CAP	4872	843047
ELT	4909	714051
JOP	3220	508941
RUS	5730	876969
SDN	5850	1266380
THA	5680	728749
TXI	4080	649242

**Figure 3.5.** Plot of time for strength development (min.) as a function of C_3S/C_2S ratio as determined from MAS ^{29}Si NMR for 50 psi (■, $R = 0.878$) and 500 psi (□, $R = 0.673$).

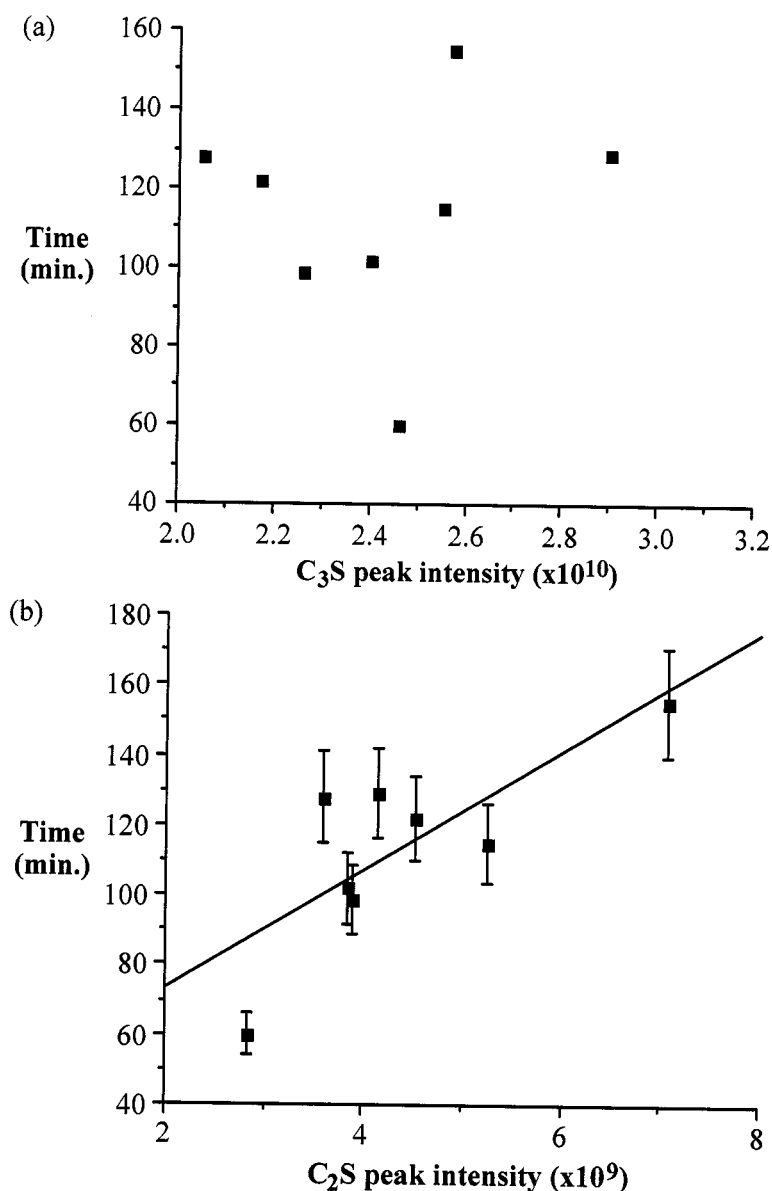


Figure 3.6. Plot of time for strength development (min.) as a function of (a) C_3S and (b) C_2S ($R = 0.603$) peak intensity as determined from MAS ^{29}Si NMR for 50 psi.

correlation is stronger with the characteristic time than with the “bulk” content. This suggests that the characteristic time is indeed correlating with active surface content.

A plot of Young’s modulus measured from destructive mechanical testing versus the characteristic time for C_3S shows a relatively strong correlation (Figure 3.11), in the form of a trend of increasing modulus with decreasing characteristic time. However, the

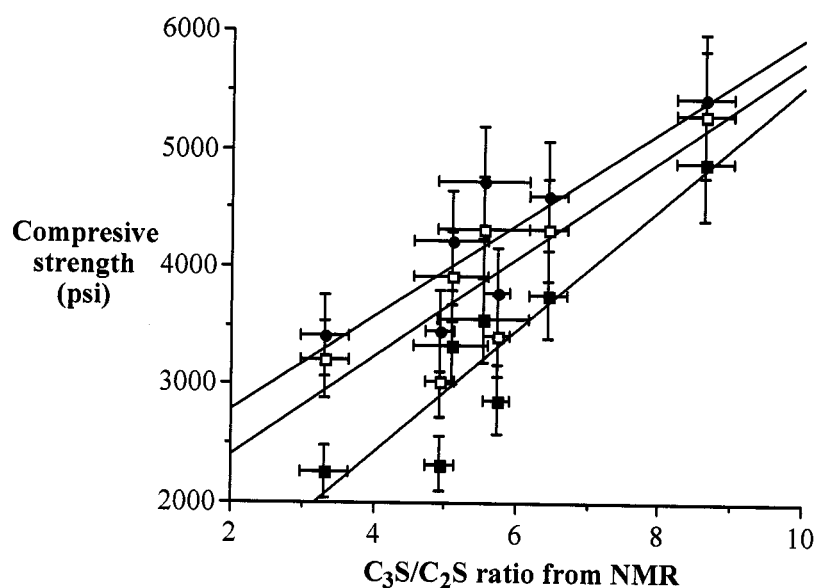


Figure 3.7. Plot of compressive strength (psi) development as a function of C₃S/C₂S ratio as determined from MAS ²⁹Si NMR at 24 h (■, R = 0.837), 48 h (□, R = 0.734), and 72 h (●, R = 0.743).

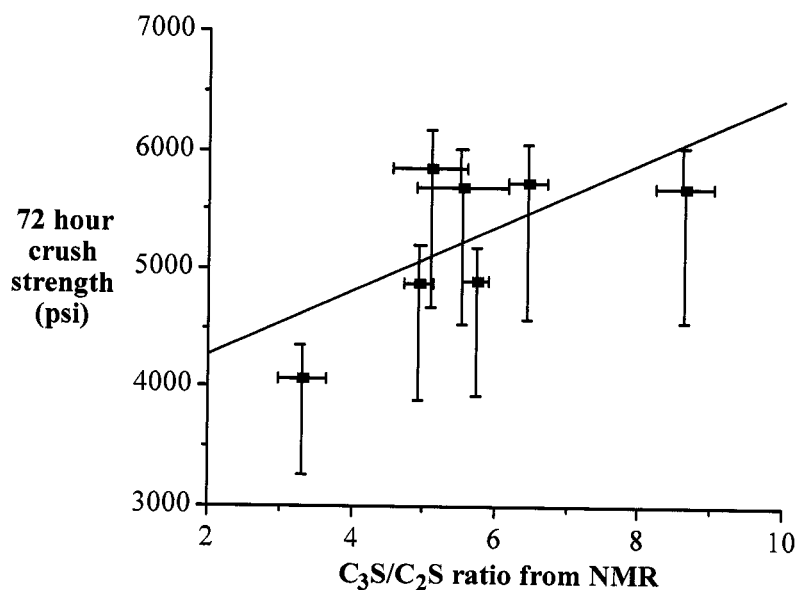


Figure 3.8. Plot of time for 72 hour crush strength (psi) as a function of C₃S/C₂S ratio as determined from MAS ²⁹Si NMR (R = 0.445).

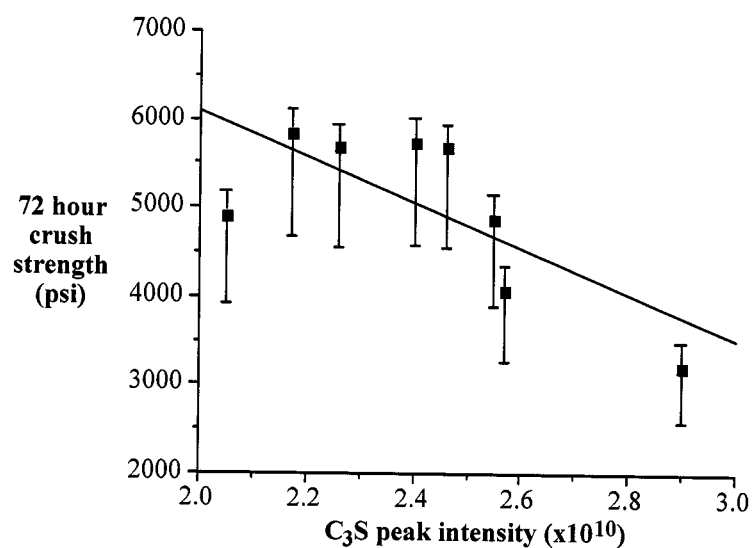


Figure 3.9. Plot of time for 72 hour crush strength (psi) as a function of C₃S peak intensity as determined from MAS ²⁹Si NMR ($R = 0.532$).

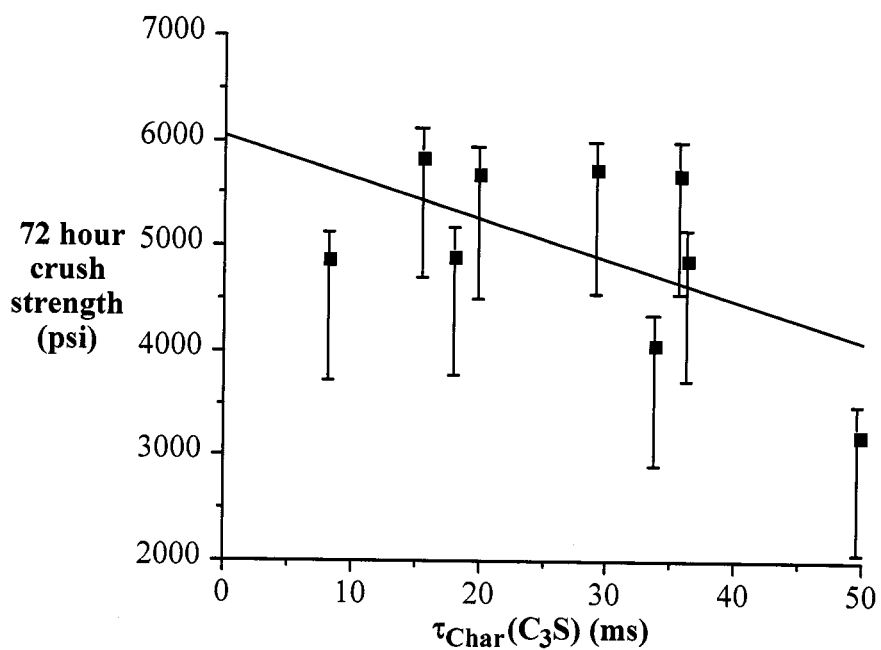


Figure 3.10. Plot of time for 72 hour crush strength (psi) as a function of C₃S characteristic relaxation time as determined from MAS ²⁹Si NMR ($R = 0.714$).

large and asymmetric errors associated with measurements of crush strength makes any predictive correlation questionable at this time.

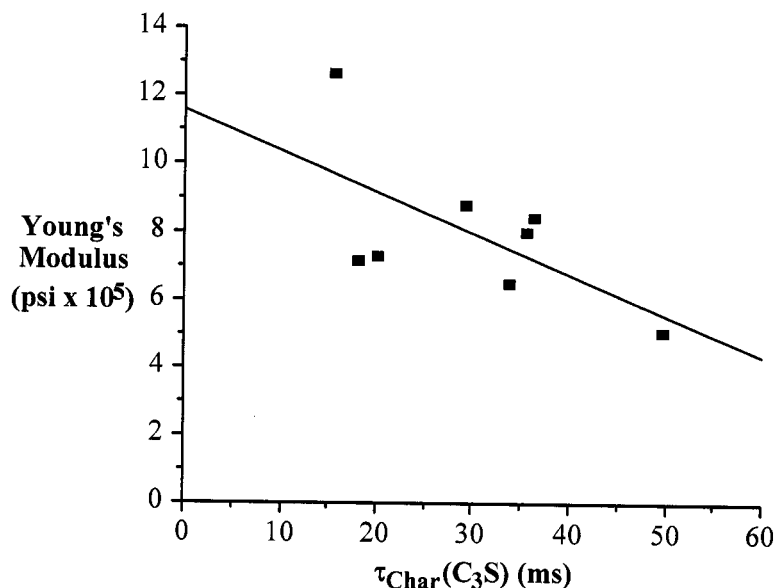


Figure 3.11. Plot of Young's modulus (psi) as a function of C_3S characteristic time as determined from MAS ^{29}Si NMR ($R = 0.621$).

Correlations for cement and retarder. Given that it is typical for cements to be used in concert with a retarder, there is interest in whether the correlations demonstrated for the cements (above) are also maintained for experiments in the presence of retarder. The retarder investigated is lignosulfonate.

Lignosulfonates are large, anionic polymers that have been used as oil well cement retarders for many years. Although the exact mechanism of lignosulfonates retarding the set of Portland cement is not well understood, it has been postulated that the mechanism is a combination of adsorption and nucleation.^{8,9} Studies have shown sulfonate and hydroxyl groups adsorb onto the C-S-H gel layer of the hydrating cement. This fact has lead to the hypothesis that the sulfonate and hydroxyl groups present in lignosulfonates allow them to adsorb onto and, consequently, incorporate into the C-S-H

gel layer, causing a change in the morphology of the C-S-H gel and leading to a more impermeable structure. This causes a type of waterproofing effect slowing further hydration. Barron and co-workers recently used ^{27}Al and ^{29}Si solid state NMR spectroscopy to confirm this model.¹⁰ The results also show that while the effect of lignosulfonates on the C_3A hydration should not be discounted, lignosulfonates predominantly affects the hydration kinetics of the C_3S .¹¹

Table 3.12. Consistometry data for cements with retarder.

Sample	Time to 50 Bc ^a (min.)	Time to 70 Bc (min.)	Time to 100 Bc (min.)
BRZ	66	72	78
CAP	90	98	107
ELT	155	168	180
JOP	230	247	250
RUS	78	87	93
SDN	105	128	139
THA	78	83	92
TXI	124	137	147

^aBearden consistency units, proportional to the torque on the paddle in the rotating cup of the consistometer.

Table 3.12 shows the thickening time data for the cements studied with retarder, Table 3.13 shows the UCA data for the cements studied with retarder, and Table 3.14 shows the destructive mechanical testing data for the cements studied with retarder. The

Table 3.13. Ultrasonic data for cements with retarder.

Sample	Time to 50 psi (min.)	Time to 500 psi (min.)	Strength at 24 hours (psi)	Strength at 48 hours (psi)	Strength at 72 hours (psi)
BRZ	115	152	3774	4360	5280
CAP	177	281	2385	3138	3581
ELT	220	317	2901	3486	3825
JOP	424	513	2973	3793	4222
RUS	169	228	3839	4297	4544
SDN	183	273	3469	4152	4385
THA	152	206	3780	4516	4970
TXI	246	351	2324	3061	3259

data contained in Table 2.2 and Tables 3.1-3.8 may be plotted against the data in Tables 3.12-3.14 to graphically evaluate possible correlations.

Again, as evidenced by the low correlation coefficients, there is no observable correlation between thickening time measurements and the silicate ratio. This is unfortunate, since a correlation of retarder response would have proven very valuable to petroleum engineers wishing to better predict pumpability windows.

Figure 3.12 shows a plot of compressive strength development in terms of time to achieve a given compressive strength of slurries with retarder versus the saturation recovery-derived silicate ratio; Figure 3.13 shows a plot of compressive strength development in terms of time to achieve a given compressive strength of slurries with retarder versus the characteristic time for C_3S . As expected, the correlation indicates that

Table 3.14. Destructive mechanical testing data for cements with retarder.

Sample	72 Hour Crush Strength (psi)	Young's Modulus (psi)
BRZ	3980	526104
CAP	4028	738779
ELT	5160	722237
JOP	6200	820678
RUS	5740	932170
SDN	5260	726191
THA	5170	811219
TXI	4050	688539

shorter times to achieve target strengths are required when more of the C-S-H-producing C_3S is present.

Figure 3.14 shows a plot of compressive strength development for cements in the presence of 0.5% lignosulfonate retarder bwoc in terms of compressive strength attained by a given time, versus the saturation recovery-derived silicate ratio. It should be noted that while a general trend remains, the correlation is significantly worse than the data without the retarder present. This is unfortunate, since it indicates that predictive power with respect to retarder response is weaker than it is for the properties of the cement alone. It should also be noted that the data for BRZ is lower than expected given the remaining data. Given the high C_3S content of BRZ, the data seem to indicate that while lignosulfonate is proposed to be an indiscriminant retarder, that it actually has a greater affinity for C_3S than C_2S . However, it could also be that some aspect of the BRZ sample

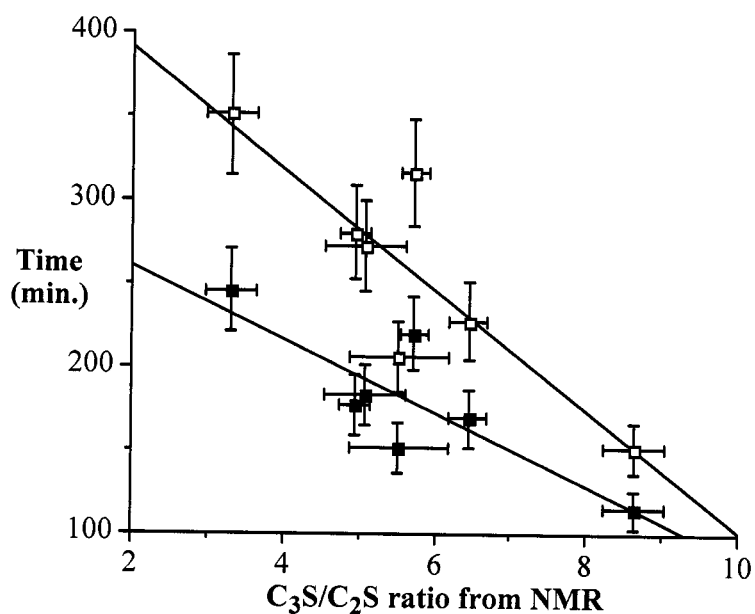


Figure 3.12. Plot of time for strength development (min.) in the presence of 0.5% lignosulfonate retarder bwoc as a function of C_3S/C_2S ratio as determined from MAS ^{29}Si NMR for 50 psi (■, $R = 0.697$) and 500 psi (□, $R = 0.743$).

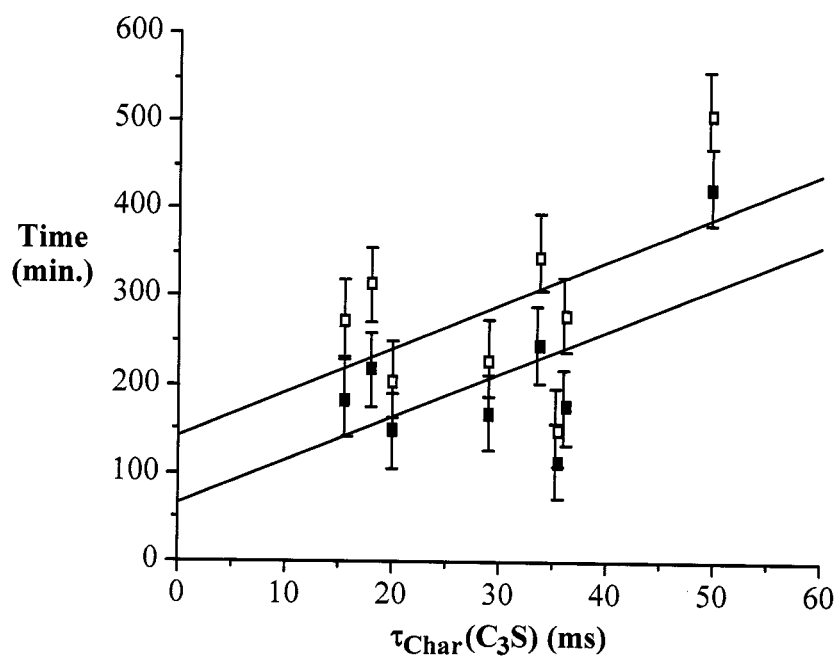


Figure 3.13. Plot of time for strength development (min.) in the presence of 0.5% lignosulfonate retarder bwoc as a function of C_3S/C_2S ratio as determined from MAS ^{29}Si NMR for 50 psi (■, $R = 0.524$) and 500 psi (□, $R = 0.592$).

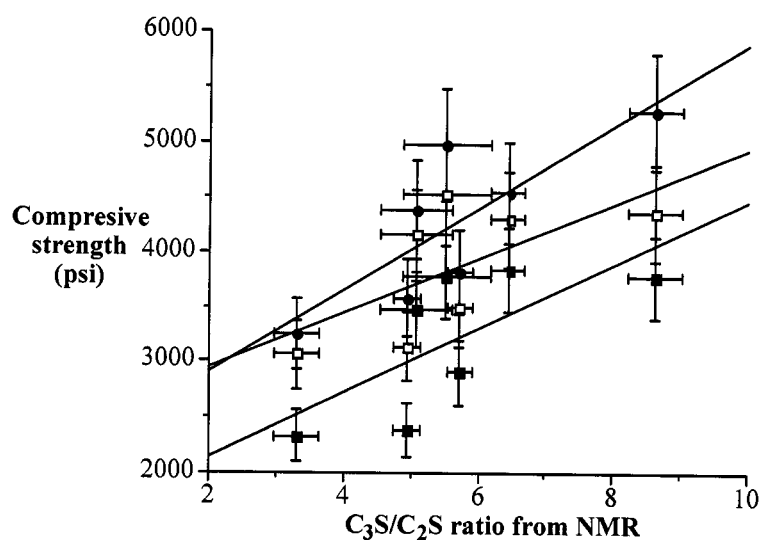


Figure 3.14. Plot of compressive strength development (psi) in the presence of 0.5% lignosulfonate retarder bwoc as a function of C_3S/C_2S ratio as determined from MAS ^{29}Si NMR at 24 h (■, $R = 0.501$), 48 h (□, $R = 0.436$), and 72 h (●, $R = 0.667$).

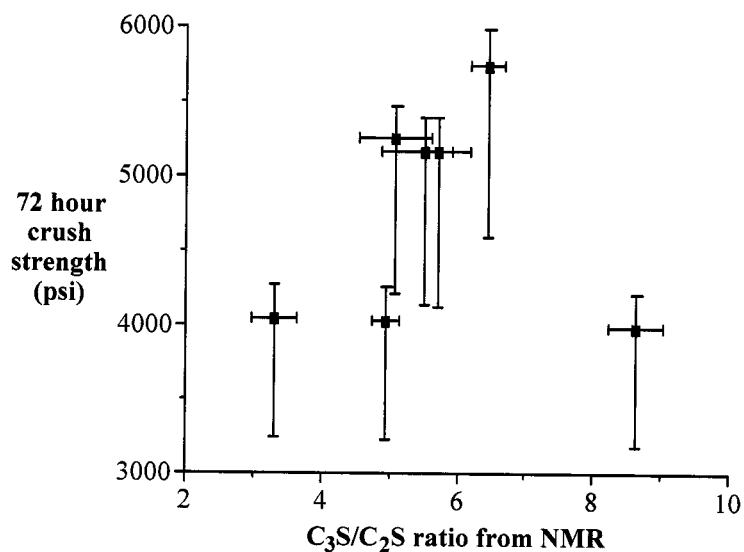


Figure 3.15. Plot of time for 72-hour crush strength (psi) in the presence of 0.5% lignosulfonate retarder bwoc as a function of C_3S/C_2S ratio as determined from MAS ^{29}Si NMR.

is unique and is acting to enhance its strength development by means outside the scope of this analysis.

Whereas a plot of the 72-hour crush strength measured from destructive mechanical testing versus the C_3S/C_2S ratio showed a trend without additives, (see Figure 3.9), the presence of a lignosulfonate retarder appears to show deviation from a trend. As shown by the data in Figure 3.15, the value for BRZ is significantly lower than expected considering the remainder of the data. Additional 72-hour crush strength measurements would have to be performed in order to ascertain if any significant trend was viable. It is likely that the BRZ sample crushed had an uneven surface making contact with the testing bracket, which would have applied higher stress for a given amount of force, resulting in an anomalously low value.

A plot of Young's Modulus for cements set with retarder versus either the saturation recovery-derived silicate ratio or a characteristic relaxation time shows no correlation or trend. That a trend is observable for cement without additives, but not for retarded formulations suggests that the retarder may be interfering with the mechanism for the generation of stiffness in cement formulations without additives.

Correlations for cement and fluid loss additive. Fluid loss additives prevent the loss of water from the cement slurry to porous rock formations downhole. These additives often have the added effect of either retarding or viscosifying the cement slurry. The additive in question for this portion of the study is a copolymer of N,N-dimethylformamide and 2-acrylamido-2-methylpropane sulfonic acid, a viscosifying and non-retarding variety of fluid loss additive. Polymers of this nature are polyelectrolytes that act as flocculants that tie up free water in a slurry until the water can be consumed by the cement hydration reactions. The ramifications of the addition of these polymers to cements are not fully understood.

Table 3.15 shows the thickening time data for the cements studied with fluid loss additive, Table 3.16 shows the UCA data for the cements studied with fluid loss additive, and Table 3.17 shows the destructive mechanical testing data for the cements studied with fluid loss additive. The data contained in Table 2.2 and Tables 3.1-3.8 may be plotted against the data in Tables 3.15-3.17 to graphically evaluate possible correlations.

Table 3.15. Consistometry data for cements with fluid loss additive.

Sample	Time to 50 Bc ^a (min.)	Time to 70 Bc (min.)	Time to 100 Bc (min.)
BRZ	51	61	70
CAP	73	74	75
ELT	94	98	102
JOP	135	137	140
RUS	75	81	85
SDN	78	82	84
THA	45	70	78
TXI	91	92	94

^a Bearden consistency units, proportional to the torque on the paddle in the rotating cup of the consistometer.

There appears to be no distinctive trend for the 72-hour crush strength measured from destructive mechanical testing versus the C_3S/C_2S ratio in the presence of a fluid loss additive. A plot of Young's Modulus for cements set without additives versus the

Table 3.16. Ultrasonic data for cements with fluid loss additive.

Sample	Time to 50 psi (min.)	Time to 500 psi (min.)	Strength at 24 hours (psi)	Strength at 48 hours (psi)	Strength at 72 hours (psi)
BRZ	78	113	4308	4600	4801
CAP	180	247	2400	3160	3622
ELT	181	247	3013	3577	3550
JOP	215	276	3154	3778	4080
RUS	125	167	3873	4234	4400
SDN	158	211	3646	4191	4294
THA	129	164	4196	5046	5200
TXI	180	249	2676	3092	3328

saturation recovery-derived silicate ratio shows no correlation or trend. Variations in contact surfaces for the samples could have accounted for the lack of a correlation.

As evidenced by the low correlation coefficients, there is no observable correlation between thickening time measurements and the silicate ratio. In this particular case, however, a trend is not necessarily expected, as it is impossible for the slurry to lose water in the HPHT consistometer and this particular additive is non-retarding. A weak trend is observed with characteristic relaxation time for C_3S , however; Figure 3.16 shows the plot of this correlation. It is unclear why the presence of fluid loss additive manifests a correlation where none was found without additives or with retarder instead.

Like the previous series, a plot of compressive strength development in terms of time to achieve a given compressive strength of slurries with a fluid loss additive versus

the saturation recovery-derived silicate ratio shows a trend (Figure 3.17). The same line of reasoning for the cements without additives applies to the trend with respect to variations in cements.

Table 3.17. Destructive mechanical testing data for cements with fluid loss additive.

Sample	72 Hour Crush Strength (psi)	Young's Modulus (psi)
BRZ	5360	922284
CAP	5623	1049038
ELT	a	a
JOP	5660	876809
RUS	a	a
SDN	6540	981463
THA	7860	1095458
TXI	5030	781451

^a Data unavailable.

Figure 3.18 shows a plot of compressive strength development for cements (in the presence of fluid loss additive) in terms of compressive strength attained by a given time of cements with fluid loss additive versus the saturation recovery-derived silicate ratio. We note that, like the effect of retarder, the fluid loss additive lowers the correlation observed.

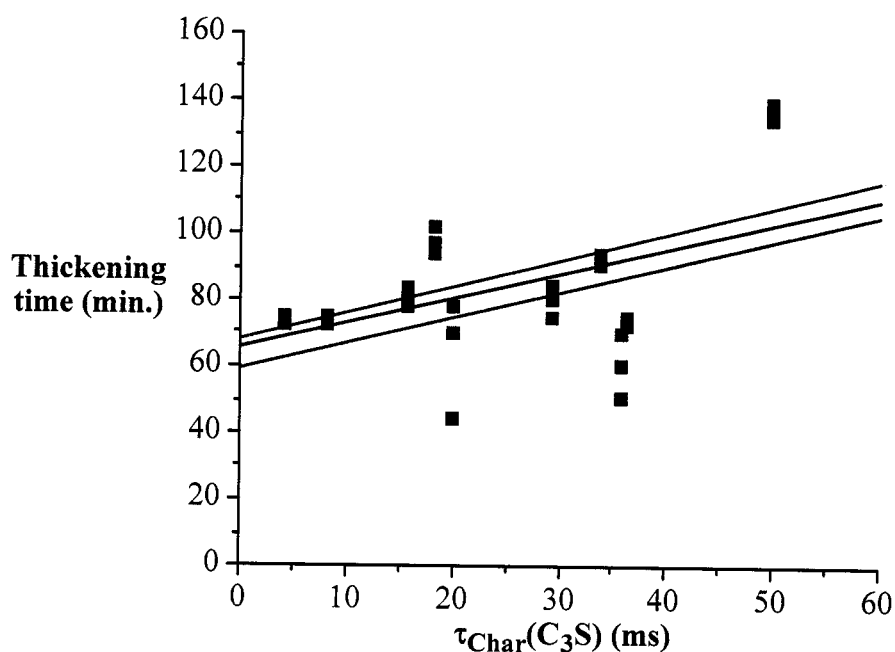


Figure 3.16. Plot of thickening time (min.) in the presence of 0.5% fluid loss additive bwoc as a function of C_3S characteristic relaxation time for 50 Bc (\blacksquare , $R = 0.507$), 70 Bc (\square , $R = 0.476$), and 100 Bc (\blacksquare , $R = 0.484$).

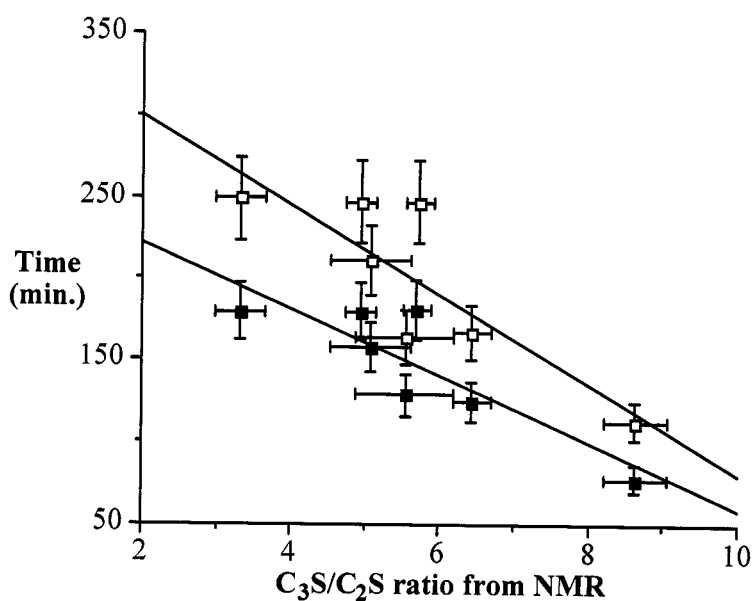


Figure 3.17. Plot of time for strength development (min.) in the presence of 0.15 % fluid loss additive bwoc as a function of $\text{C}_3\text{S}/\text{C}_2\text{S}$ ratio as determined from MAS ^{29}Si NMR for 50 psi (\blacksquare , $R = 0.740$) and 500 psi (\square , $R = 0.696$).

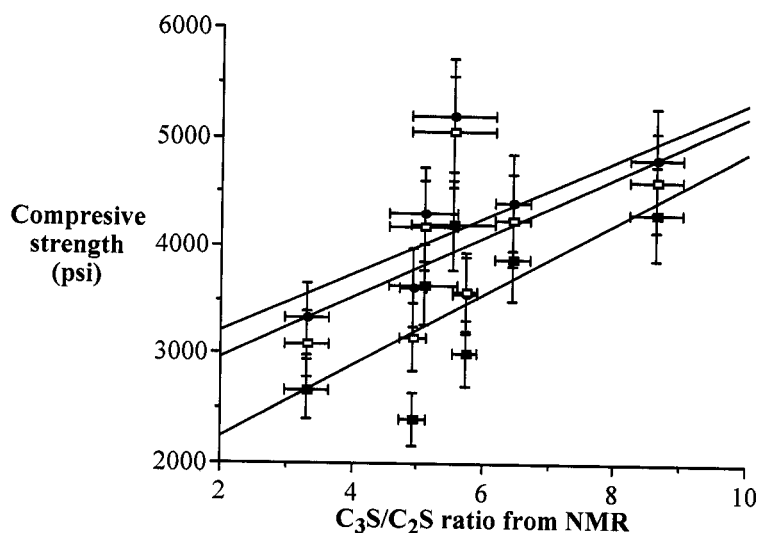


Figure 3.18. Plot of time for compressive strength (psi) in the presence of 0.15% fluid loss additive bwoc as a function of C_3S/C_2S ratio as determined from MAS ^{29}Si NMR for 24 h (■, $R = 0.505$), 48 h (□, $R = 0.381$), and 72 h (●, $R = 0.378$).

Conclusions

Determination of C_3S/C_2S ratios by NMR provides an effective method of analysis for cements, owing to NMR's direct measurement of the minerals in question; determination of characteristic relaxation times also proves useful in some situations. NMR ratios demonstrate predictive ability for the determination of engineering performance properties. This is especially the case for prediction of strength development; in keeping with generally accepted understanding of cement hydration behavior, the strength development correlates with increasing C_3S content, decreasing C_2S content, C_3S/C_2S ratio, and/or the characteristic C_3S relaxation time.

Experimental

Data from consistometry, ultrasonic testing, and mechanical testing were provided by Halliburton Energy Services. Thickening times were measured according to API Schedule 5, which operates the run at 125 °F and a pressure ramped from 1000 to 5160

psi over 28 minutes and maintained at 5160 psi until a consistency of 100 Bc is achieved. Ultrasonic cement analysis for measuring compressive strength was obtained at 140 °F and ramped pressure from ambient to 3000 psi over 30 minutes and maintained at 3000 psi for the duration of the experiment (72 hours total). The resulting cement cylinder was crushed in a mechanical tester after three days to determine compressive strength and Young's modulus. Analysis of NMR data was conducted as described in the Experimental in Chapter 2.

References

- 1 P. Barnes, X. Turrilas, A. C. Jupe, S. L. Colston, D. O'Connor, R. J. Cernik, P. Livesey, C. Hall, D. Bates and R. Denis, *J. Chem. Soc., Faraday Trans.*, 1996, **92**(12), 2187.
- 2 L. Parrott, M. Geiker, W. A. Gutteridge, and D. Killoh, *Cem. Conc. Res.*, 1990, **20**, 919.
- 3 P.-V. Vlachou, and J.-M. Piau, *Cem. Conc. Res.*, 1999, **29**, 27.
- 4 S. N. Ghosh and S. K. Handoo. *Cem. Conc. Res.*, 1980, **10**, 771.
- 5 P. Fletcher, P. V. Coveney, T. L. Hughes, and C. M. Methven, *J. Petrol. Tech.*, 1995, **47**(2), 129.
- 6 P. Coveney, P. Fletcher, and T. Hughes, *AI Magazine*, 1996, **17**, 41.
- 7 J. Keating, D. Hannant, and A. Hibbert. *Cem. Conc. Res.*, 1989, **19**, 715.
- 8 G. V. Chilingarian, E. B. Nelson, *Developments in Petroleum Science: Well Cementing*, vol. 28, Elsevier Science Publishers B.V., Amsterdam, Netherlands, 1990.
- 9 M. Y. A. Mollah, W. H. Yu, R. Schennach, and D. L. Cocke, *Polymer-Plastics Technol. Eng.*, 1999, **38**, 849.

- 10 M. Bishop and A. R. Barron, *Ind. Eng. Chem. Res.*, 2006, **45**, 702.
- 11 F. Skvara, *Mat. Res. Soc., Symp. Proc.*, 1995, **370**, 153.

Chapter 4

Error Analysis of Methods and Proposed Best Practice

Introduction

The ultimate goal of this project is the development of a tool for the prediction of the hydration chemistry of various cements based upon their chemistry. In part this work is motivated in large part by the lack of utility of conventional XRF-based oxide analyses in predicting cement performance properties. Given the heterogeneity of cement particles, this lack of predictive power is not surprising. Instead of prediction, a series of experiments must be performed on each sample to required. In this regard the present work attempts to correlate data from simple spectroscopic techniques with experimental data obtained by Halliburton Energy Services.

Based upon the results described in Chapter 3 it is proposed that two important parameters may be predicted by ^{29}Si NMR spectroscopy. First, the time during which the cement may be pumped as a slurry prior to setting, and secondly the rate at which strength is developed in the solidified cement paste. Although these are not exclusively important in allowing prediction of cement usage for downhole applications, they would be useful in allowing petroleum engineers in the field to predict the window of pumpability for slurries, as well as the drill-ahead time, when the cement around the casing is sufficiently strong to keep a seal with the casing and formation during subsequent stages of drilling. In contrast to the problems associated with XRF-based oxide analyses, the predictive ability of the NMR analysis is surprisingly powerful, given the chemical complexity and heterogeneity of cement particles.

As noted in Chapter 3, while error bars are readily calculated for the $\text{C}_3\text{S}/\text{C}_2\text{S}$ ratio determined by the NMR method, the errors for the physical measurements are less readily estimated. Furthermore, the data for one of the cement samples (JOP) appears to show anomalous behavior. In this Chapter the relative errors associated with each method

are discussed and a new approach for prediction of the hydration reaction of cements is proposed.

Discussion

Error analysis. This work was motivated in large part by the lack of utility of conventional XRF-based oxide analyses in predicting cement performance properties. Figure 4.1 shows the plot of “active” C_3S/C_2S ratio determined by NMR versus the calculated “classical” C_3S/C_2S ratio based on oxide analysis from X-ray fluorescence and application of the Bogue equations.¹ It is clear that the two parameters show little relationship. Furthermore, as seen in Figure 4.2, a plot of the relationship of the C_3S/C_2S ratio determined by either method with time to achieve a compressive strength of 50 psi shows that the ratio determined by NMR shows a very viable trend, while that from traditional analytical methods shows no relationship. This result is repeated for all the trends discussed in Chapter 3. Thus, it would appear this validates the assessment that the hydration reaction is controlled by either the directly measured silicate content or the availability of “active” or “available” silicate within the cement grains rather than the “classical” bulk concentration (Chapters 2 and 3).

As noted in Chapter 3, the physical measurements for strength development of the JOP sample appear to be anomalous; a graphical example is given in Figure 4.3. In each case the cement appears to be less far along in the hydration reaction than would be expected from its calculated C_3S/C_2S ratio, i.e., reaction times are longer, strength measured is lower, etc. However, the anomalous data can be readily explained by attributing the lag in behavior to partial premature hydration. Given that the initial C-S-H gel layer may form and age under irregular ion gradient conditions,¹ partial hydration will have a significant effect on the strength development, but have an imperceptible effect on the C_3S/C_2S ratio measured by ^{29}Si NMR. If partial premature hydration occurs then the cement will have either “flash set,” owing to insufficient gypsum content to

mitigate the aluminate hydration, hydrated the aluminates and gypsum along the conventional hydration reaction scheme prior to the or developed a poorly formed C-S-H layer, weakly percolating the cement powder, resulting in an impediment to further hydration by conventional mechanisms. Additionally, the cement setting is slowed without the additional heat provided by initial rapid C_3S , aluminate, and/or free lime hydration at the beginning of a standard hydration run. Further hydration under standard conditions of a prematurely hydrated cement powder will take longer to reach the same strength by a given point in time referenced from the beginning of “whole-hearted” intentional hydration. This is as seen in Figure 4.3 suggesting that the physical strength measurements are highly dependent on how dry the cement sample is kept prior to analysis.

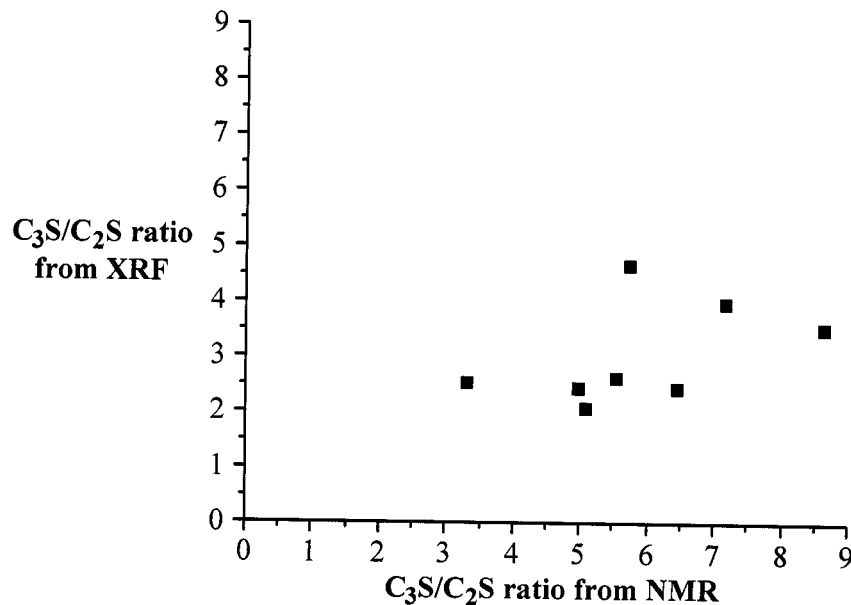


Figure 4.1. Plot of “active” C_3S/C_2S ratio (as determined by MAS ^{29}Si NMR) versus “classical” C_3S/C_2S ratio (as determined by XRF).

Figure 4.4 shows a conceptual graph of estimated error in measurement of a given performance property via both NMR and direct measurement of the given property by its

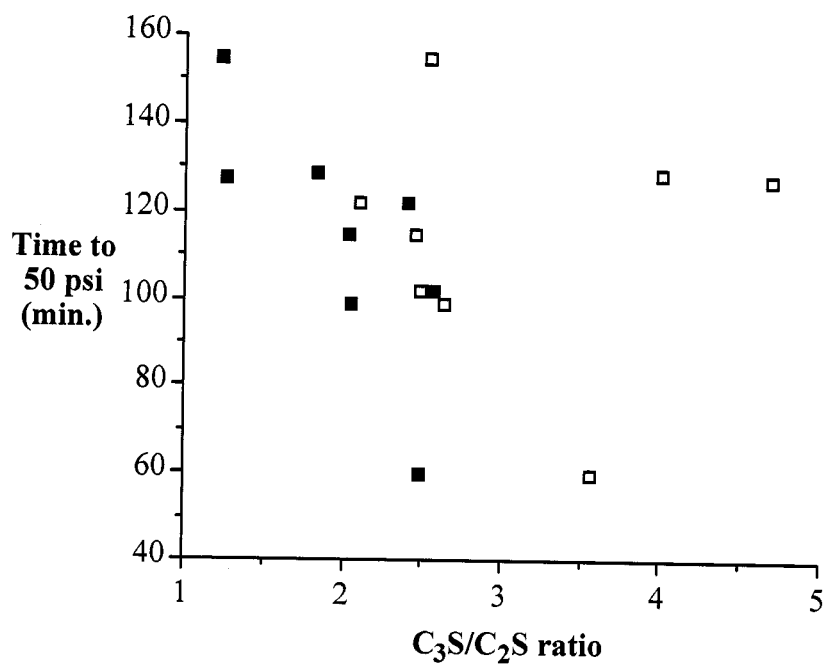


Figure 4.2. Plot of time to 50 psi (min.) versus C_3S/C_2S ratio from NMR (■) and C_3S/C_2S ratio from XRF (□).

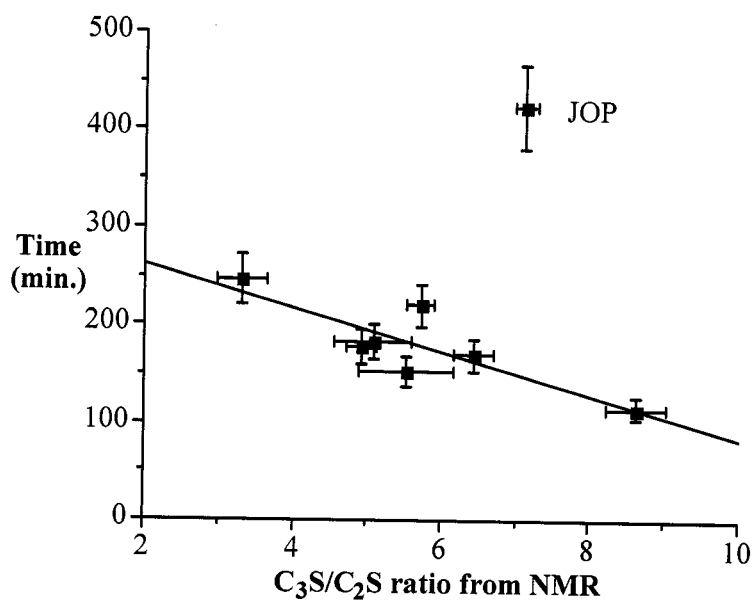


Figure 4.3. Plot of time for strength development (min.) in the presence of 0.5% lignosulfonate retarder bwoc as a function of C_3S/C_2S ratio as determined from MAS ^{29}Si NMR for 50 psi ($R = 0.697$) showing the anomalously large value for the JOP sample.

standard performance test versus relative extent of hydration progress. The potential for error in measuring the performance properties directly is substantially higher than the prediction via NMR due to the fact that the NMR predictions are unaffected by initial hydration of the more reactive aluminate phases; the measurement of the silicate

ratio will not significantly deviate from the “fresh from the plant” ratio prior to any hydration when formation of C-S-H begins to occur. Any initial hydration of cement pastes can lead to longer time scales for the property measurements, shifting all the measured time values upward and measured strength values at a given time downward. This seems to be the cause of the largely aberrant behavior of one of the samples.

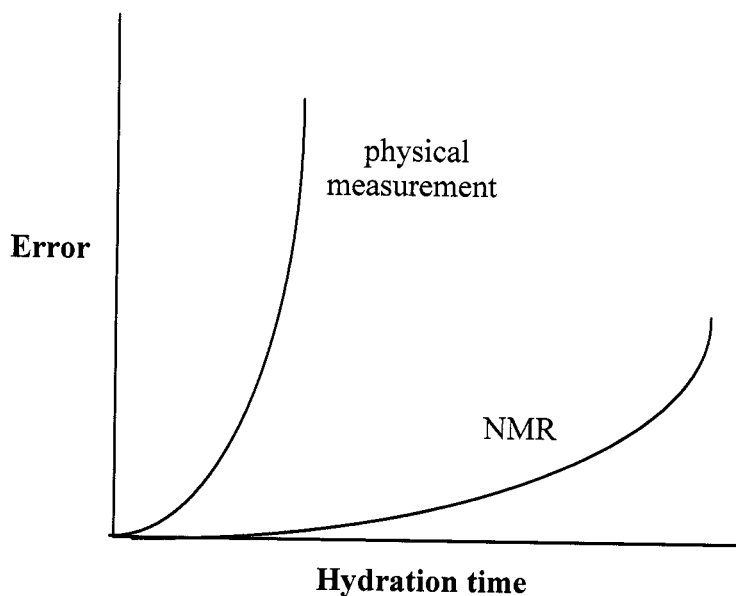


Figure 4.4. Conceptual plot of error in measurement of a given performance property via both NMR and direct physical strength/consistometry measurements.

We propose that the errors associated with our NMR method are limited to measurement errors and variability of the sample as taken for NMR spectroscopy. As described in Chapters 2 and 3, the saturation recovery data were measured on at least two samples taken at random from the cement batch. The two samples were chosen on

different days (often 60-120 days apart). The overlap of the low and central data, and high and central data shown in Figure 2.11 suggest that variability between samples is low. From Table 2.2 and Tables 3.1-3.6 a variation due to sample choice of ca. 2-3% can be calculated.

An estimate of the error inherent in the NMR measurement can be determined by a consideration of the C_3S/C_2S ratio calculated for a particular sample at τ values above which the slope in the plot of intensity of the various saturation recovery parameters plotted versus τ is essentially 0 (see e.g. Figure 2.11). In most of the cases this involved τ above 1 second. Using the data from Tables 2.2 and Tables 3.1-3.7, an error of 4% is calculated. Thus, the overall error in our NMR method for the C_3S/C_2S ratio can be estimated. It is believed that this is far lower than the errors associated with the physical strength development measurements.

It is difficult to determine the errors associated with the physical measurements, however, some of the errors can be estimated based upon prior experience.² Thickening times tend to manifest a relative error of ± 10 minutes, while UCA data tends to be less reproducible with a relative error of 10%. Reproducibility of compressive strength measurements by direct destructive analysis often have an error of ± 5 to ± 20 %, and the Young's modulus obtained from these destructive tests can manifest an error of approximately ± 15 %. Finally, as discussed above, the greatest pitfall for the traditional physical measurements is their susceptibility to premature hydration.

Proposed best practice. In light of the above, it makes more sense in the general case to use predicted values from an NMR-based analysis than to use the direct measurement of the cement performance properties in question. The following is a proposed experimental procedure for the measurement of the silicate ratio for use in cement performance property prediction.

1. Fill to capacity a solid state NMR rotor with the cement analyte. To minimize shifting of particles in the rotor and aid in the ease of spinning, use a flat-bottomed rotor cap or upper plug.
2. Apply MAS rotation to the analyte-filled rotor in an appropriately equipped NMR spectrometer at the maximum safe and prudent speed available for the rotor geometry, ideally at or exceeding 6.00 kHz to minimize the intensity of spinning sidebands. Perform pre-acquisition preparations (tuning, shimming, etc.).
3. To determine τ_{char} , collect a saturation recovery spectrum based on a 90° ^{29}Si pulse at the maximum amplifier power permitted for safe operation of the spectrometer centered at -50 ppm, a spectral width of at least 2.5 times the spinning speed, a pulse train of at least 256 pulses with an interstitial delay of 2.0 μs , a smoothly telescoping logarithmic series τ delays with at least 12 values from 1 to 1000 ms, a relaxation delay of 0.0 ms, a minimum of 128 dummy scans, and a number of acquisition scans sufficient to achieve a signal to noise ratio of at least 30. The number of dummy scans may need to be increased for cements with higher iron content. It is probable that time constraints will make splitting the τ series a prudent course of action. Ensure that the number of scans used in each partial series is sufficient to achieve a signal to noise ratio of at least thirty for the longest value of τ to be used, and ensure that at least one value overlaps in each partial series for rescaling.
4. To determine the $\text{C}_3\text{S}/\text{C}_2\text{S}$ ratio, obtain a simple 1-dimensional spectrum with the same applicable parameters as above, but with a relaxation delay of at least 3.0 seconds until a signal to noise ratio of at least 50 is obtained.
5. Process the data (Fourier transform, phasing, shift calibration, baseline correction) to obtain a spectrum of the cement analyte with a flat baseline leading away from the silicate lineshape for several ppm.

6. Rescale the data (if applicable) and apply a deconvolution to each spectrum or subspectrum as described in Chapter 2 of this work to obtain the desired characteristic relaxation times and ratios.
7. Apply the appropriate correlation to the obtained ratios or values of τ_{char} to predict the desired properties.

Conclusions

Determination of $\text{C}_3\text{S}/\text{C}_2\text{S}$ ratios by NMR provides a superior method of analysis for cements relative to calculated ratios from oxide analysis owing to NMR's direct measurement of the minerals in question. Determination of characteristic relaxation times by NMR relaxation analysis also provides useful data otherwise unavailable. Additionally, NMR data demonstrate far greater predictive power than the oxide analysis for the determination of engineering performance properties. However, in order for this proposal to be useful there needs to be a significant statistical study of the variability of the engineering property measurements. This will allow for a prediction of the strength development for an ideal cement sample (i.e., dry and unaged), as well as under partial hydration conditions. Once statistically meaningful strength development data are obtained, it is proposed that future determinations of cement behavior with respect to downhole performance properties may be made in a predictive manner using ^{29}Si MAS NMR spectroscopy.

References

- ¹ H. F. W. Taylor, *Cement Chemistry*, Thomas Telford Publishing, London, 1997.
- ² Gary Funkhouser and Dennis Gray, Halliburton Energy Services. Personal communication.

Chapter 5¹

Solid State ^{13}C NMR of F-SWNTs: Using MAS alone to attenuate ^{13}C - ^{19}F dipole-dipole interactions, obtain narrow and unusually shielded fluoromethine ^{13}C signals, and assess extent of fluorination

Introduction

Fluorinated single walled carbon nanotubes (F-SWNTs)^{2,3,4} offer advantages as a synthon for sidewall functionalized SWNTs with a wide range of functional groups by the reaction with organolithium and Grignard reagents or primary amines.^{5,6,7,8} Fluorination is accomplished by the direct reaction of purified SWNTs with F_2 gas diluted in argon, along with HF (proposed to act as a catalyst).^{2,3} A saturation stoichiometry is reached of *ca.* C_2F without destruction of the tube structure. F-SWNTs are shown to form meta-stable solutions of individual tubes (as opposed to bundles) in DMF, THF and alcohols. Computational and experimental results are ambiguous as to whether 1,2-addition⁹ or 1,4-addition¹⁰ of F_2 to the sidewall predominates.¹¹ STM images indicate that fluorination occurs in bands along the length of the tube;¹⁰ however, calculations suggest that addition along the SWNT axis should be preferred over that around the circumference.¹¹ Irrespective of the arrangement of the F substituents, thermolysis of F-SWNTs results in their cleavage into shorter lengths. For example, fluorination to a formula of C_5F followed by pyrolysis results in the cutting of SWNTs into short 20–100 nm lengths.^{12,13}

Unlike typical organic molecules, the characterization of functionalized SWNTs has been accomplished *via* Raman and IR spectroscopy, TGA, AFM, and STM. Unfortunately, AFM and TGA do not unambiguously determine whether functional groups are covalently bound rather than absorbed onto the SWNT's surface. The presence of a significant D (disorder) mode at *ca.* 1300 cm^{-1} is consistent with sidewall functionalization,¹⁴ and the relative intensity of D mode versus the tangential G mode

(1550 – 1600 cm^{-1}) is often used as a measure of the level of substitution. However, it is shown that Raman is an unreliable method for determination of the extent of functionalization since the relative intensity of the D band is also a function of the substituents distribution as well as concentration. It is shown that while Raman is useful in demonstrating the presence of sp^3 carbon atoms within the SWNT sidewall, its use for quantitative analysis is dubious.⁷ Thus, it is often difficult to definitively characterize functionalized SWNTs. This state of affairs stands in contrast to other organic or inorganic molecules (even polymers) where NMR has been successfully used as a primary tool for both compositional and structural characterization.

As would be expected, the low solubility and large size (and hence slow tumbling in solution) of the functionalized SWNTs limited useful solution NMR studies.¹⁵ Prior solid state NMR studies have proved useful for the observation of substituents^{15b,16,17,18,19} but, unfortunately, often less so with regard to the observation of the important quaternary sp^3 sidewall carbon atoms that would provide definitive evidence for covalent attachment. In one report, the quaternary sidewall carbon atoms were clearly detected by obtaining CPMAS spectra with and without a dephasing delay before FID acquisition.¹⁹ As part of ongoing studies on the NMR characterization of functionalized SWNTs, there was an interest in the study of one of the simplest examples of substituted SWNTs. The results are presented herein.

Results and Discussion

HiPCo SWNTs produced at Rice University were purified to remove iron and other impurities²⁰ and subsequently fluorinated to a C:F ratio of approximately 2.1:1 by direct fluorination at 150 °C by a previously reported procedure.³ The Raman spectra using 780 nm (red laser) excitation for F-SWNTs show, in addition to the tangential G mode (*ca.* 1587 cm^{-1}), an intense broad D (disorder) mode at *ca.* 1295 cm^{-1} , consistent with sidewall functionalization.¹⁴

The 50.3 MHz ^{13}C MAS NMR spectrum of a sample of F-SWNTs is shown in Figure 5.1. Chemical shifts are relative to glycine carbonyl defined as 176.46 ppm.²¹ The peak at δ 128 ppm is typical of the sp^2 carbon of the sidewall of a SWNT.^{18,19,22} The relative areas of the downfield and upfield signals are close to that expected given the C:F ratio determined from XPS, suggesting an assignment for the upfield signal of sp^3 carbon atoms attached to fluorine (i.e., C-F). Strong support for such an assignment is provided by ^{13}C chemical shift data in the literature for relatively simple tertiary alkyl fluorides and fluorinated derivatives of C_{60} . With a peak maximum of 83.5 ppm, this signal from the F-SWNTs is about 7-15 ppm upfield of that exhibited by C-F in tertiary alkyl fluorides containing 1-fluoroadamantyl,²³ 1-fluorobicyclo[2.2.2]octyl,²⁴ and 1-

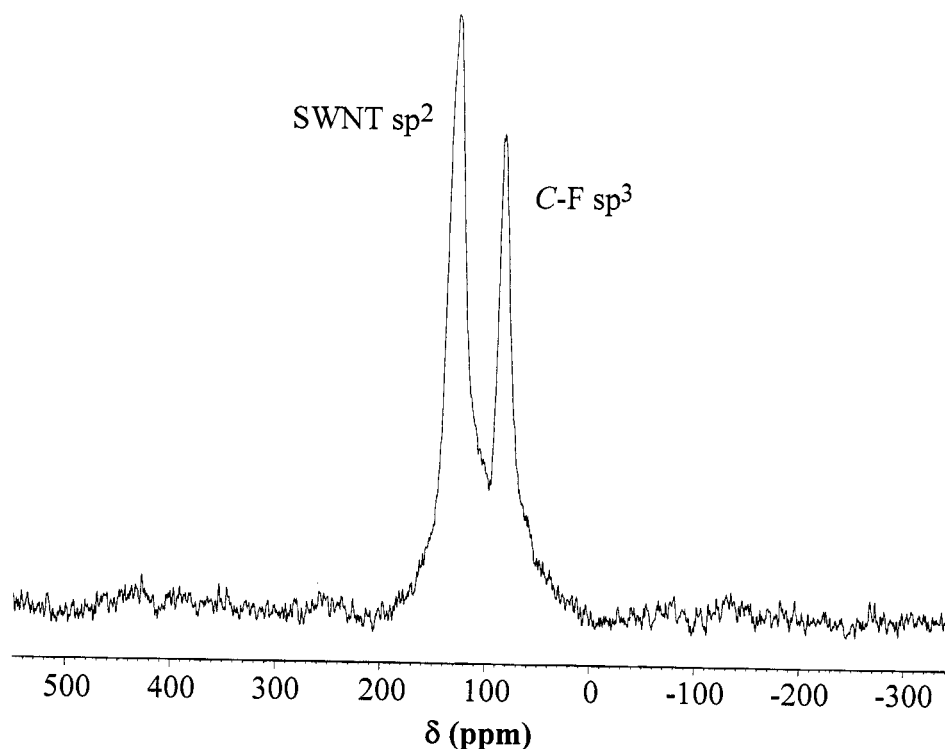


Figure 5.1. ^{13}C MAS NMR spectrum of F-SWNTs obtained at 50.3 MHz ^{13}C (4.7 T) and 15 kHz spinning. 4.5- μs 90° ^{13}C pulse, 20.5-ms FID (^1H decoupling not used), 10-s relaxation delay, 8600 scans. FID processed with 50 Hz (1 ppm) of line broadening. Spinning sidebands would be ± 298 ppm from a centerband and are clearly negligible.

fluorobicyclo[3.3.1]nonyl²⁵ groups and as much as 20 ppm upfield of the signal exhibited by C-F in more strained 1-fluorobicyclo[2.2.1]heptyl groups.²⁶ However, a peak maximum of 83.5 ppm for the F-SWNTs is identical to that reported in the $^{13}\text{C}\{^{19}\text{F}\}$ spectrum of $T_{\text{h}}\text{-C}_{60}\text{F}_{24}$, which has 24 equivalent, isolated CF groups.²⁷

Pairs of fluorine atoms would be expected to add to the SWNTs in a 1,2- or 1,4-fashion. Unfortunately, compounds with two or more aliphatic C-F groups appear to be rare, thus making it difficult to assess the effect of multiple fluorine atoms on the F-SWNTs' C-F ^{13}C chemical shifts. ^{13}C NMR data are available for two 1,4-difluoro aliphatic compounds. Replacing the bridgehead H in 1-fluorobicyclo[2.2.2]octane with F (to form 1,4-difluorobicyclo[2.2.2]octane) shields the C-F by 3.0 ppm and gives a signal at δ 91.6.^{25a} Replacing the bridgehead H in 9-fluorotriptycene with F (to form 9,10-difluorotriptycene) shields the C-F by 1.6 ppm and gives a signal at δ 97.2.²⁸ The only 1,2-difluoro compounds found with fluorine atoms on adjacent tertiary-alkyl carbons are *cis*-15,16-difluoro-15,16-dihydropyrene²⁹ and $\text{C}_{2v}\text{-C}_{60}\text{F}_2$,³⁰ both of which would be desirable models for 1,2-fluorine addition to a SWNT. Unfortunately, ^{13}C NMR data were not reported for the pyrene derivative, and the ^{19}F -coupled ^{13}C signals for the sp^3 carbon in $1,2\text{-C}_{60}\text{F}_2$ were not detected.³¹ Multiple fluorination of fullerenes clearly compounds the difficulty of detecting ^{13}C signals in the absence of fluorine decoupling. For example, no ^{13}C NMR data were reported for $D_{5d}\text{-C}_{60}\text{F}_{20}$, which has a single type of CF group in a $(\text{CF})_{20}$ loop.³¹ However, ^{13}C signals ranging from δ 84.0 to δ 91.2 were tentatively reported for the four different types of CF groups in $\text{C}_{3v}\text{-C}_{60}\text{F}_{18}$;³² and ^{13}C signals ranging from δ 86.5 to δ 91.3 were reported for the three different types of CF groups in the $(\text{CF})_{15}$ loop of $\text{C}_{3v}\text{-C}_{60}\text{F}_{15}\{\text{C}[\text{C}(\text{O})\text{OCH}_2\text{CH}_3]_3\}_3$;³³ and ^{13}C signals ranging from δ 86-90 were reported for the CF groups in a mixture of materials analyzing as $\text{C}_{60}\text{F}_{46}$.³⁴ Lacking ^{13}C NMR data for simple 1,2-difluoro compounds with fluorines on adjacent tertiary-alkyl carbons, it is noted that a fluorine atom usually has a modest deshielding effect on the adjacent β -carbon, i.e., F-C-C-, compared to the corresponding

carbon in an H-C-C- environment.³⁵ Thus, the unusually shielded C-F ^{13}C NMR signals observed in the F-SWNTs (Figure 5.1) may result from the nanotube environment exerting a significant shielding effect. Calculations are consistent with 1,2-addition to the SWNTs predominating.

The unusually shielded ^{13}C NMR signals observed for the F-SWNTs are not the only interesting anomaly observed for this spectrum. Fluorine-substituted carbons exhibiting different chemical shifts are to be expected because the starting material is a complex mixture of SWNTs differing in diameter and chirality and because fluorination, like alkylation,¹⁹ is expected to occur at different nanotube sites and with the possibility of different addition patterns. Given this expectation, the C-F signal is somewhat narrower than expected in comparison with the nanotube sp^2 carbon signal (Figure 5.1).

MAS can much more effectively eliminate ^{13}C - ^{19}F dipole-dipole broadening than ^{13}C - ^1H dipole-dipole broadening because the dipolar coupling constant has an inverse cube dependence on the C-X bond length (i.e., $D_{\text{CF}} \propto 1/r_{\text{CF}}^3$) and r_{CF} is 0.3 Å longer than r_{CH} [e.g., $r_{\text{CF}} = 1.383$ Å and $r_{\text{CH}} = 1.087$ Å in CH_3F ; $r_{\text{CF}} = 1.43$ Å in $(\text{CH}_3)_3\text{C-F}$ and $r_{\text{CH}} = 1.122$ Å in $(\text{CH}_3)_3\text{C-H}$].³⁶ Furthermore, these data show that r_{CF} in a tertiary alkyl fluoride is slightly longer than in less highly substituted fluorides. As a result, compared to D_{CH} , D_{CF} is reduced by slightly more than a factor of two, which significantly aids line narrowing by MAS alone. The large influence of bond length on line narrowing has also been demonstrated with the 4.7 T ^{119}Sn MAS NMR spectrum of trimesityltin fluoride, $[2,4,6-(\text{CH}_3)_3\text{C}_6\text{H}_2]_3\text{SnF}$. This compound has $r_{\text{SnF}} = 1.96$ Å for each molecule in the asymmetric unit, and MAS at just 3.1 kHz clearly gives a pair of $^1J_{\text{SnF}}$ doublets for the two molecules.³⁷ In order to further understand the narrow line width of the C-F signal, the effect of spinning speed on the spectral resolution was investigated.

^{13}C spectra obtained on the F-SWNTs with 6, 9, 12, and 15 kHz MAS (the maximum possible with the available probe using rotors with an outer diameter of 4mm)

show (Figure 5.2, left) that increasing the spinning speed from 6 to 9 to 12 kHz causes a steady, significant increase in signal intensity for the upfield C-F signal relative to the downfield nanotube sp^2 carbon signal, but that only a relatively modest further increase is achieved with 15 kHz MAS. To be sure, the faster spinning also increases the intensity of each centerband relative to the intensity of the various spinning sidebands, but it is clear that reducing ^{13}C - ^{19}F dipole-dipole interactions is much more important than reducing chemical shift anisotropy effects in generating centerband signals. Thus, 15 kHz MAS appeared to be rather effective at eliminating the ^{13}C - ^{19}F dipole-dipole broadening in this sample of highly fluorinated SWNTs, an observation that is particularly encouraging as relatively few laboratories have solid state ^{19}F capability.

The observation of signals from C-F groups was confirmed by obtaining spectra at 6, 9, 12, 15, 20, 25, and 30 kHz using a probe on a 500 MHz spectrometer (125.8 MHz ^{13}C) designed for 2.5 mm rotors (Figure 5.2, right). It is clear that increasing the spinning speed from 15 to 30 kHz has relatively little effect, even though chemical shift anisotropy effects are 2.5 times larger on the 500 MHz spectrometer and the signal-to-noise ratio is much lower on the 500 MHz spectrometer due to the smaller rotor containing ten times less material than the 4 mm o.d. rotor used on the 200 MHz spectrometer. Thus, using 15 kHz MAS with the larger rotor on the 200 MHz spectrometer is taken to be adequate for obtaining useful ^{13}C spectra of F-SWNTs. The spinning sidebands are negligible and the signal-to-noise is much higher in the 200 MHz spectra compared to the corresponding spectrum obtained on the 500 MHz spectrometer, although the centerband nanotube sp^2 signal and centerband C-F signal are not as well resolved at the lower field. In studies of polymers, others have also observed the beneficial effect of fast MAS for generating ^{13}C signals by attenuating strong ^{13}C - ^{19}F dipole-dipole interactions.³⁸

Intramolecular dipole-dipole interactions can also be effectively averaged by rapid molecular tumbling in nearly spherical molecules possessing high symmetry. Adamantane is perhaps the best known example of such. Relatively slow (2.2 kHz) MAS

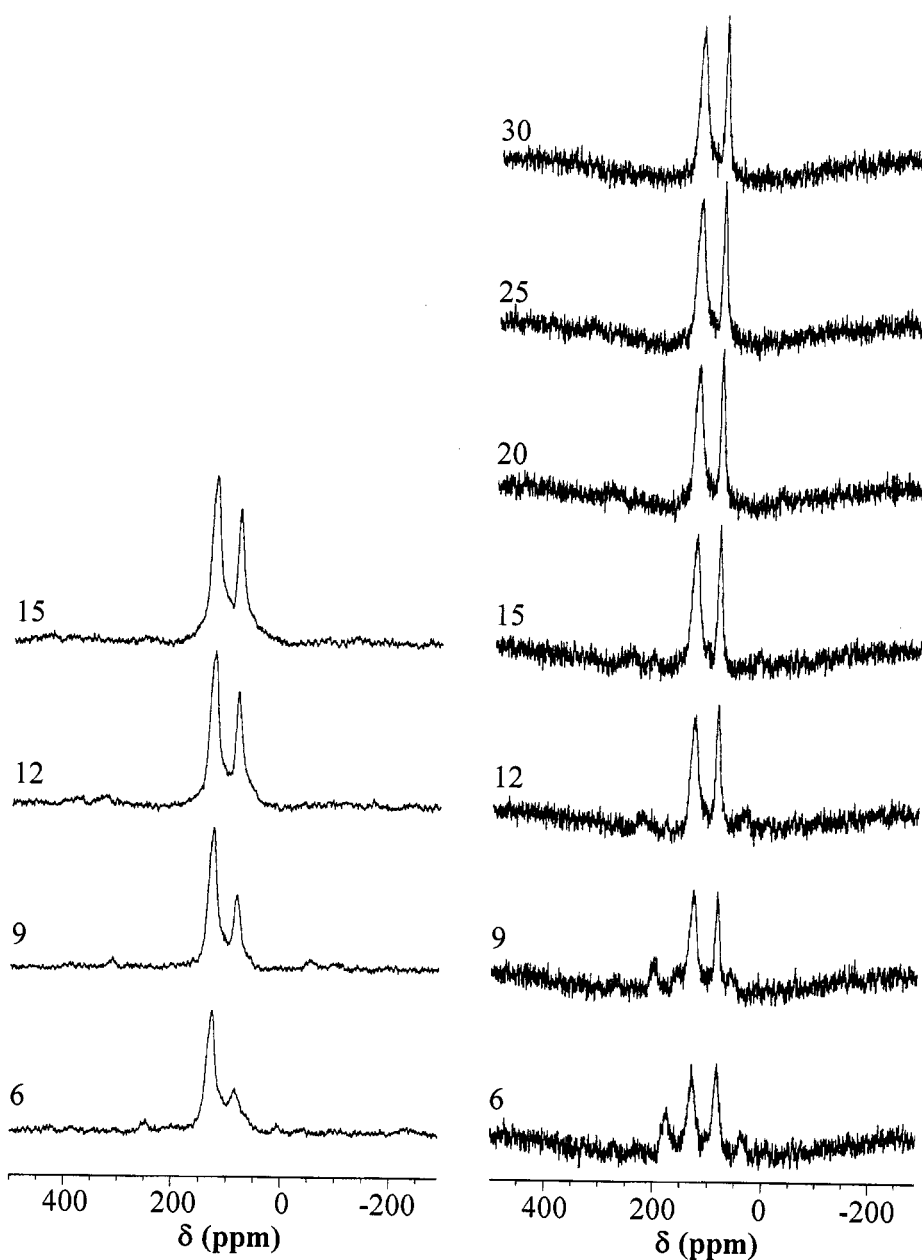


Figure 5.2. ^{13}C MAS NMR spectra of F-SWNTs obtained at 50.3 MHz ^{13}C with a 4mm OD rotor (left, 56.9 mg) and at 125.8 MHz ^{13}C with a 2.5mm OD rotor (right, 5.4 mg) at the spinning speeds indicated (in kHz). 90° ^{13}C pulse ($4.5\ \mu\text{s}$ at 50.3 MHz; $2.0\ \mu\text{s}$ at 125.8 MHz), 20.5-ms FID (^1H decoupling not used), 10-s relaxation delay, 8600 scans. FID processed with 50 Hz (1 ppm at 50.3 MHz; 0.4 ppm at 125.8 MHz) of line broadening. Spinning sidebands are clearly evident in the spectra obtained at slower spinning speeds and at the higher field strength.

without proton decoupling significantly narrows its ^{13}C signals.³⁹ In this context, it is worth noting that D_3 - and S_6 - $\text{C}_{60}\text{F}_{48}$, which are nearly spherical isomers,⁴⁰ give a 75.5 MHz ^{13}C MAS spectrum with at least six partially resolved CF signals ranging from 83-96 ppm with MAS at just 2.84 kHz.⁴¹ With respect to shape, the long, highly anisotropic F-SWNTs are the opposite of the nearly spherical $\text{C}_{60}\text{F}_{48}$, and faster MAS is required for generating relatively sharp CF signals from F-SWNTs accordingly.

We should note that the observed ^{13}C NMR signals in the spectra of the F-SWNTs result entirely from the F-SWNTs, as no ^{13}C signal is detected on the 200 MHz spectrometer under the same conditions when an empty rotor (zirconia rotor barrel and Kel-F cap) is spun at 15 kHz. Kel-F, which is poly(chlorotrifluoroethylene), under suitable spectroscopic conditions gives ^{13}C signals at 115 and 104 ppm for the CF_2 and CFCl groups.^{39,42} Similarly, the ^{13}C signals observed on the 500 MHz spectrometer result entirely from the F-SWNTs.

With the peak at 83.5 ppm confidently assigned to the sp^3 C-F carbon atoms, two questions arise. Firstly, can it be assigned to either 1,2- or 1,4-addition of the fluorine to the SWNT sidewall? Secondly, with the peak due to C-F, then why is there no scalar ^{13}C - ^{19}F coupling observed?

To determine whether the observed peaks could be assigned to either 1,2- or 1,4-addition, the theoretical ^{13}C NMR shifts have been calculated for a series of substituted F-SWNT fragments. In order to simplify calculations, a $\text{C}_{80}\text{H}_{20}$ fragment of the 5,5 (armchair) conformation was used. The calculated shifts for the sp^3 (C-F) and sp^2 carbons are shown in Figure 5.3 for single and double 1,2- and 1,4-addition to the SWNT sidewall. As may be seen from Figure 5.3, the experimentally observed spectrum of F-SWNTs (84 ppm) is consistent with multiple 1,2-additions (*ca.* 82 ppm). Given the line width for the spectrum (Figure 5.1), the calculations do not preclude the presence of a minor component of 1,4-addition products; however, this work proposes that F-SWNTs are predominantly that of 1,2-addition products as proposed by Scuseria and co-workers.⁹

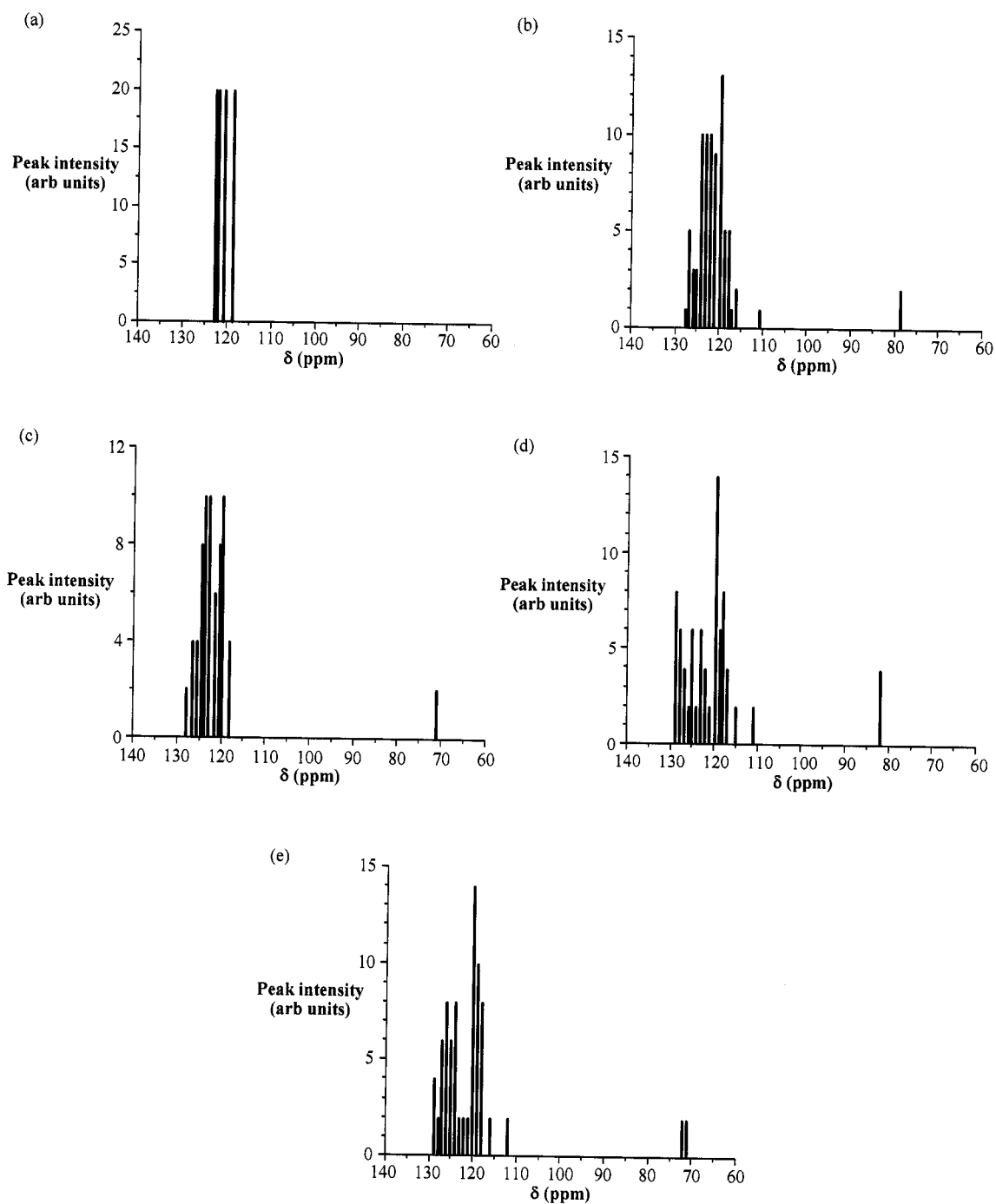


Figure 5.3. Calculated ^{13}C NMR shifts for (a) $\text{C}_{80}\text{H}_{20}$ fragment of the 5,5 (armchair) conformation, and as a result of (b) 1,2-addition by 2 fluorine atoms, (c) 1,4-addition by 2 fluorine atoms, (d) 1,2-addition by 4 fluorine atoms, and (e) 1,4-addition by 4 fluorine atoms.

Based upon the model compound data and the calculated ^{13}C NMR shifts, the peak at 84 ppm is undoubtedly due to the sp^3 carbon atoms; however, this begs a second question as to why no scalar ^{13}C - ^{19}F coupling is observed. Isotropic J couplings are unaffected by MAS;⁴³ thus one might at first expect to observe ^{13}C - ^{19}F J couplings, which are typically about 180-210 Hz in tertiary alkyl fluorides.^{24a,25,27-29} However, such couplings are not observed in the ^{13}C spectra of the F-SWNTs. Three explanations, all of which probably apply, can be proposed. First, with fluorine-substituted ^{13}C nuclei present in different environments, numerous $^1J_{\text{CF}}$ doublets could overlap, thus obscuring any fine structure. $^1J_{\text{CF}}$ values in F-SWNTs generated by multiple 1,2-additions may also be larger than $^1J_{\text{CF}}$ values in monofluoro tertiary alkyl fluorides. $\text{C}_{60}\text{F}_{15}\{\text{C}[\text{C}(\text{O})\text{OCH}_2\text{CH}_3]_3\}_3$ contains a $(\text{CF})_{15}$ loop with three different types of CF groups that exhibit $^1J_{\text{CF}}$ values of *ca.* 240 Hz.³⁴ In addition, two-, three-, and four-bond J_{CF} couplings expected to range from approximately 25 to 1 Hz would further broaden the observed ^{13}C signal.^{24a,25,27,29,34}

A likely more significant reason for not observing ^{13}C - ^{19}F J couplings is that at finite MAS speeds, the cross term in the first-order average Hamiltonian between the homonuclear ^{19}F - ^{19}F dipolar coupling and the heteronuclear ^{13}C - ^{19}F dipolar coupling leads to a direct broadening of the ^{13}C resonances.⁴⁴ In addition, magnetization exchange between the doublet components caused by the fluorine spin diffusion process manifests itself in the ^{13}C spectrum like a chemical exchange process, *i.e.*, the two ^{13}C signals of a ^{13}C - ^{19}F doublet can collapse into a singlet (a self-decoupling of the J -interaction) whose linewidth depends on the MAS speed.^{44,44} If the fluorine spin diffusion rate is much smaller than J , a well-resolved doublet may be observed.⁴⁵ $(\text{CD}_3)_3^{15}\text{NHCl}$ provides an analogous situation with ^{15}N and ^1H instead of ^{13}C and ^{19}F ; in the ^{15}N spectrum obtained with 30 kHz MAS and no ^1H decoupling, a sharp doublet resulting from $^1J_{\text{NH}} \approx 100$ Hz is clearly detected.⁴⁵

Thermal decomposition of F-SWNTs. The ability to quantify the presence of sidewall functionalization by ^{13}C MAS NMR provides the potential for studying subsequent reactivity of F-SWNTs. One of the simplest reactions of F-SWNTs is their thermal decomposition and the re-formation of pristine SWNTs, albeit with the reduction in the length of the SWNTs. F-SWNTs studied in this work decompose between 250 and 600 °C with the loss of F_2 and fluorine-containing products. F-SWNTs heated to 400, 450 and 550 °C (see Experimental) have been analyzed by ^{13}C MAS NMR, Raman, and IR spectroscopy, and XPS.¹

Table 5.1. Analysis of F-SWNTs as a function of thermolysis temperature.

Temperature (°C)	XPS C:F ratio	Raman G:D ratio	NMR $\text{sp}^2\text{:sp}^3$ ratio ^b
150 ^a	2.1	0.51	2.3
400	2.4	0.53	4.9
450	4.24	0.54	16
550	14.1	1.50	c

^aAs prepared F-SWNTs, see Experimental. ^bThe NMR ratios are only approximate in light of the substantial overlap of the sp^2 carbon and C-F signals and the absence of information on the relative relaxation rates of these two types of carbons. ^cNot measurable.

Figure 5.4 shows the ^{13}C MAS NMR spectra of F-SWNTs at various stages of thermolysis. It is clear that as thermolysis continues the C-F groups are removed. In

particular the spectra are significantly altered between 400 and 450 °C with a decrease in the size of the peak due to the C-F sp^3 carbons (Table 5.1).

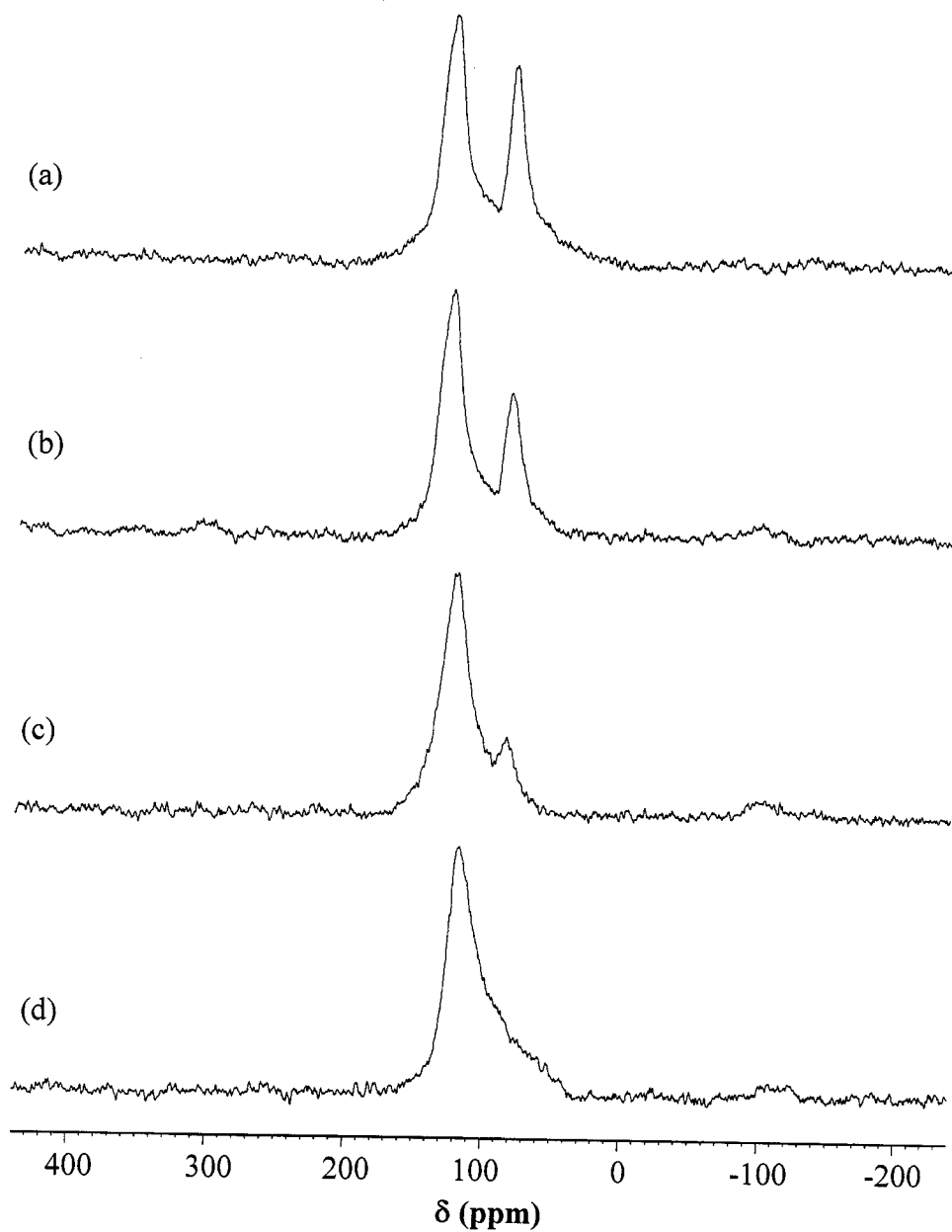


Figure 5.4. ^{13}C MAS NMR spectra of F-SWNTs obtained at 50.3 MHz ^{13}C (a) as prepared at 150 °C (parameters as in Figure 5.1), after heating to (b) 400, (c) 450, and (d) 550 °C, with 11 kHz MAS used for the heated samples (other parameters as in Figure 5.1).

After thermolysis at 550 °C the ^{13}C MAS NMR spectrum is essentially identical to that of pristine SWNTs, although XPS indicates the presence of a formula of $\text{C}_{14.1}\text{F}$ (Table 5.1), suggesting that the detection of the sidewall functionalized sp^3 carbon is difficult at low levels of functionalization. As fluorine is removed, the peak maximum for the downfield signal shifts upfield, slightly at first (from δ 128.2 to δ 126.8 upon heating to 400 °C), and then more noticeably as larger amounts of fluorine are removed (to δ 123.4 upon heating to 450 °C and to δ 117.3 upon heating to 550 °C). Thus, fluorine appears to exert the usual β -deshielding effect on nanotube sp^2 carbons.

The intensity of the Raman D band decreases as the thermolysis temperature increases. This is consistent with the loss of sidewall functionalization. The G band shows a concomitant sharpening and increase in intensity. As expected XPS analysis shows a decrease in F content with increased temperature (Table 5.1). In addition to the observation of multiple fluorine species (where ^{13}C NMR can only distinguish the C-F unit), the high-resolution C1s spectra allow for two types of SWNT sp^2 carbon. A peak at 284.3 – 284.8 eV is due to a “normal” SWNT sidewall sp^2 carbon, while a peak at 285.5 eV can be assigned as being a next-nearest neighbor sp^2 carbon (i.e., C-C-F).³⁵ Unfortunately, quantification is complicated by the presence of a component in the peak at 285.5 eV due to oxidation defects in the SWNT.⁴⁶ Taking these defects into account a qualitative measurement can be obtained for the relative abundance of C-F, C-C-F and “normal” sp^2 carbon atoms as a function of thermolysis temperature. F-SWNTs have been reported to have a band-like structure and the concurrent loss of C-F and C-C-F is in agreement with the retention of bands during de-fluorination.

NMR versus Raman for functional group quantification. As noted in the introduction, the presence of a significant D mode has been the primary method for determining the presence of sidewall functionalization. It has been commonly accepted that the relative intensity of D mode versus the tangential G mode is a measure of the

level of substitution. However, this work demonstrates that the G:D ratio is also dependent on the distribution of the substituents. NMR spectroscopy should not show a dependence on the distribution of substituents if the peaks due to the sidewall sp^2 and sp^3 carbons can be differentiated.

F-SWNTs offer a near ideal system for the study of different spectroscopic techniques for both the confirmation and quantification of sidewall functional groups on SWNTs. Firstly, covalent functionalization is well accepted and has been demonstrated by STM. Secondly, the substituent contains no carbon allowing for easy quantification by XPS in order to provide a reference analytical methodology. Finally, an individual sample of SWNTs can be prepared with a range of substituent concentrations by de-fluorinating the same batch of F-SWNTs at different temperatures.

Table 5.1 summarizes the changes in the C:F ratio (XPS), the G:D ratio (Raman), and the ratio of $sp^2:sp^3$ carbon atoms (NMR). The XPS, Raman, and NMR data demonstrate the same trend consistent with decreasing substituent (F) content as the thermolysis temperature is increased. Figure 5.5 shows a plot of NMR and Raman analysis as a function of the C:F ratio in order to ascertain the validity of using these techniques for quantification. The extent of functionalization as measured by ^{13}C MAS NMR spectroscopy ($sp^2:sp^3$ ratio) shows a direct linear correlation with the F concentration. Unfortunately, in the present case problems in peak integration at low levels of functionalization limit the correlation to high levels of functionalization. In contrast, the use of Raman spectroscopy to quantify the presence of fluorine substituents is clearly suspect. From Figure 5.5 it appears that there is essentially no change in the G-band:D-band ratio despite a doubling of the amount of functional group.

Based upon the data above this work proposes that ^{13}C NMR spectroscopy is best applied when looking at small changes in functionalization at high levels of functionalization. In contrast, Raman spectroscopy and the relative intensity of the G- and D-bands does not provide an accurate quantification of small differences at high levels of

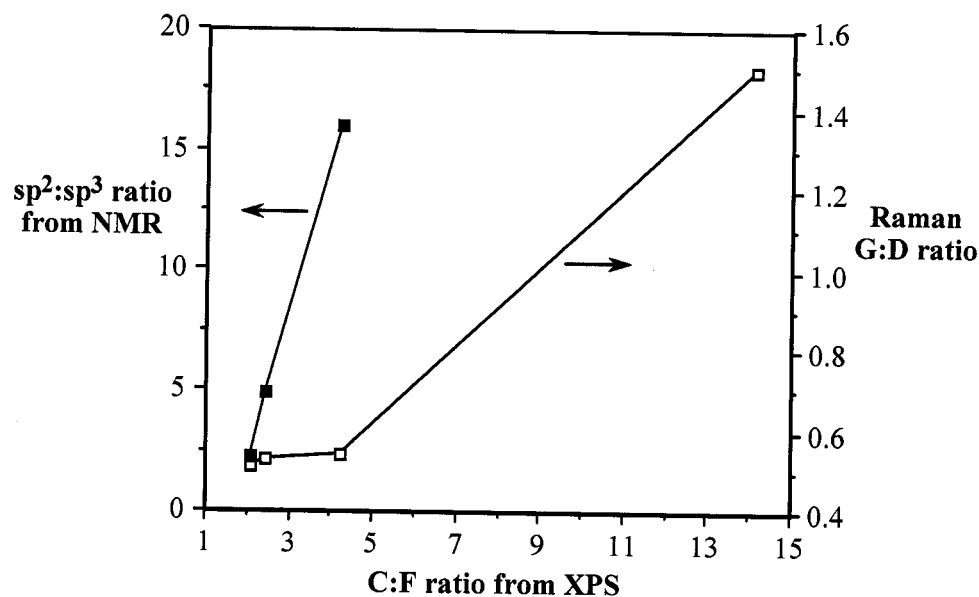


Figure 5.5. Plot of C(sp²):C-F(sp³) ratio (■) and Raman G-band:D-band ratio (□) as a function of the C:F ratio from XPS.

functionalization. This is in agreement with previous studies that Raman gave misleading results with regard to quantification because of the importance of substituent distribution in determining the intensity of the D-band. Due to problems in peak integration at low levels of functionalization, NMR is limited more than Raman at low functionalization levels. Such problems may be overcome to a degree by the use of larger samples. It is proposed, therefore, that where a comparison of samples with a high degree of functionalization is required, NMR provides a much better quantification than Raman. However, where a comparison between samples with low levels of functionalization or large differences in degree of functionalization is required, Raman provides a much better quantification than NMR.

Conclusions

The ¹³C NMR shift for the sp³ fluorine substituted (C-F) carbon atoms of the SWNT sidewall provides the first experimental evidence for the predominance of 1,2

addition rather than 1,4 addition of fluorine. NMR clearly provides a suitable method for demonstrating covalent sidewall functionalization of SWNTs. With regard to the quantification of substituents, it can be concluded that ^{13}C NMR spectroscopy is best applied when looking at small changes in functionalization at high levels of functionalization. It has also been shown that, in agreement with prior results, Raman spectroscopy would be advisable for the *quantification* of the number of sidewall substituents.

Experimental

HiPCo SWNTs produced at Rice University were fluorinated, to a C:F ratio of 2.1:1, by direct fluorination at 150 °C by a previously reported procedure.² The preparation of F-SWNTs after 400 °C heating proceeded as follows: Before heating, the reaction vessel holding 100 mg F-SWNTs was purged by argon for 30 min at room temperature. Then, under argon atmosphere, the F-SWNT sample was heated to 400 °C and held at 400 °C for 30 min. The sample was then cooled to room temperature. The preparations of F-SWNTs after 450 °C and 550 °C were performed in an analogous manner. ^{13}C MAS NMR spectra were obtained on Bruker Avance 200 and Avance 500 MHz spectrometers.^{18,19} All applicable collection data are given in figure legends.

References

- ¹ L. Zhang, J. Yang, C. L. Edwards, L. B. Alemany, V. N. Khabashesku, and A. R. Barron, *Chem. Commun.*, 2005, 3265.
- ² J. L. Margrave, E. T. Mickelson, R. H. Hauge, P. J. Boul, C. B. Huffman, J. Liu, R. E. Smalley, K. Smith, and D. T. Colbert, US Patent 6,835,366 (2004).

- 3 E. T. Mickelson, C. B. Huffman, A. G. Rinzler, R. E. Smalley, R. H. Hauge, and J. L. Margrave, *Chem. Phys. Lett.*, 1998, **296**, 188.
- 4 V. N. Khabashesku, W. E. Billups, and J. L. Margrave, *Acc. Chem. Res.*, 2002, **35**, 1087.
- 5 P. J. Boul, J. Liu, E. T. Mickelson, C. B. Huffman, L. M. Ericson, I. W. Chiang, K. A. Smith, D. T. Colbert, R. H. Hauge, J. L. Margrave, and R. E. Smalley, *Chem. Phys. Lett.*, 1999, **310**, 367.
- 6 J. L. Stevens, A. Y. Huang, H. Peng, I. W. Chiang, V. N. Khabashesku, and J. L. Margrave, *Nano Lett.*, 2003, **3**, 331.
- 7 L. Zhang, J. Zhang, N. Schmandt, J. Cratty, V. N. Khabashesku, K. F. Kelly, and A. R. Barron, *Chem. Commun.*, 2005, 5429.
- 8 L. Yang, L. Zhang, and A. R. Barron, *Nano Lett.*, 2005, **5**, 2001.
- 9 DFT (PBE/3 and LSDA/3-21G) calculations suggest that the 1,2-isomer is more stable by 16.7 kJ.mol⁻¹. K. N. Kudin, H. F. Bettinger, and G. E. Scuseria, *Phys. Rev. B*, 2001, **63**, 45413.
- 10 Molecular mechanics (MM+) and semiempirical (AM1 and CNDO) calculations suggest that the 1,4-isomer is more stable by 4.1 kJ.mol⁻¹. K. F. Kelly, I. W. Chiang, E. T. Mickelson, R. H. Hauge, J. L. Margrave, X. Wang, G. E. Scuseria, C. Radloff, and N. J. Halas, *Chem. Phys. Lett.*, 1999, **313**, 445.
- 11 (a) K. A. Park, Y. S. Choi, Y. H. Lee, and C. Kim, *Phys. Rev. B*, 2003, **68**, 045429/1. (b) P. E. Pehrsson, W. Zhao, J. W. Baldwin, C. Song, J. Liu, S. Kooi, and B. Zheng, *J. Phys. Chem. B*, 2003, **107**, 5690. (c) R. L. Jaffe, *J. Phys. Chem. B*, 2003, **107**, 10378. (d) G. Van Lier, C. P. Ewels, F. Zuliani, A. De Vita, and J.-C. Charlier, *J. Phys. Chem. B*, 2005, **109**, 6153.

- 12 Z. Gu, H. Peng, R. H. Hauge, R. E. Smalley, and J. L. Margrave, *Nano Lett.* 2002, **2**, 1009.
- 13 H. F. Bettinger and H. Peng, *J. Phys. Chem. B*, 2005, **109**, 23218.
- 14 M. S. Dresselhaus, M. A. Pimenta, P. C. Ecklund, and G. Dresselhaus, *Raman Scattering in Materials Science*, ed. W. H. Webber and R. Merlin, Springer-Verlag, Berlin, 2000.
- 15 (a) E. T. Mickelson, I. W. Chiang, J. L. Zimmerman, P. J. Boul, J. Lozano, J. Liu, R. E. Smalley, R. H. Hauge, and J. L. Margrave, *J. Phys. Chem. B*, 1999, **103**, 4318. (b) A. Kitaygorodskiy, W. Wang, S.-Y. Xie, Y. Lin, K. A. S. Fernando, X. Wang, L. Qu, B. Chen, Y.-P. Sun, *J. Am. Chem. Soc.*, 2005, **127**, 7517.
- 16 L. S. Cahill, Z. Yao, A. Adronov, J. Penner, K. R. Moonosawmy, P. Kruse, and G. R. Goward, *J. Phys. Chem. B*, 2004, **108**, 11412.
- 17 C. G. Bac, P. Bernier, S. Latil, V. Jourdain, A. Rubio, S. H. Jhang, S. W. Lee, Y. W. Park, M. Holzinger, and A. Hirsch, *Curr. Appl. Phys.*, 2001, **1**, 149.
- 18 H. Peng, L. B. Alemany, J. L. Margrave, V. N. Khabashesku, *J. Am. Chem. Soc.*, 2003, **125**, 15174.
- 19 F. Liang, L. B. Alemany, J. M. Beach, W. E. Billups, *J. Am. Chem. Soc.*, 2005, **127**, 13941.
- 20 I. W. Chiang, B. E. Brinson, A. Y. Huang, P. A. Willis, M. J. Bronikowski, J. L. Margrave, R. E. Smalley, and R. H. Hauge, *J. Phys. Chem. B*, 2001, **105**, 8297.
- 21 S. Hayashi, K. Hayamizu, *Bull. Chem. Soc. Jpn.*, 1991, **64**, 685.
- 22 S. Hayashi, F. Hoshi, T. Ishikura, M. Yumura, and S. Ohshima, *Carbon*, 2003, **41**, 3047.

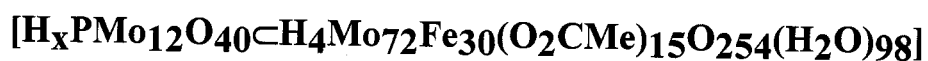
- 23 (a) G. E. Maciel, H. C. Dorn, R. L. Greene, W. A. Kleschick, M. R. Peterson, Jr., and G. H. Wahl, Jr., *Org. Magn. Reson.*, 1974, **6**, 178. (b) G. A. Olah, J. G. Shih, B. P. Singh, and B. G. B. Gupta, *J. Org. Chem.*, 1983, **48**, 3356.
- 24 (a) W. Adcock, A. N. Abeywickrema, *J. Org. Chem.*, 1982, **47**, 2957. (b) W. Adcock and V. S. Iyer, *J. Org. Chem.*, 1985, **50**, 1538.
- 25 H.-O. Kalinowski, S. Berger, and S. Braun, *Carbon-13 NMR Spectroscopy*, John Wiley & Sons, Chichester, 1988.
- 26 W. Adcock, A. N. Abeywickrema, and G. B. Kok, *J. Org. Chem.*, 1984, **49**, 1387.
- 27 N. I. Denisenko, S. I. Troyanov, A. A. Popov, I. V. Kuvychko, B. Zemva, E. Kemnitz, S. H. Strauss, and O. V. Boltalina, *J. Am. Chem. Soc.*, 2004, **126**, 1618.
- 28 W. Adcock, and V. S. Iyer, *J. Org. Chem.*, 1988, **53**, 5259.
- 29 (a) R. H. Mitchell, T. K. Vinod, G. J. Bodwell, K. S. Weerawarna, W. Anker, R. V. Williams, and G. W. Bushnell, *Pure Appl. Chem.*, 1986, **58**, 15. (b) R. H. Mitchell, G. J. Bodwell, T. K. Vinod, and K. S. Weerawarna, *Tetrahedron Lett.*, 1988, **29**, 3287.
- 30 O. V. Boltalina, A. Y. Lukonin, J. M. Street, and R. Taylor, *Chem. Commun.*, 2000, 1601.
- 31 (a) O. V. Boltalina, V. Y. Markov, P. A. Troshin, A. D. Darwish, J. M. Street and R. Taylor, *Angew. Chem., Intl. Ed.*, 2001, **40**, 787. (b) A. A. Popov, A. A. Goryunkov, I. V. Goldt, I. E. Kareev, I. V. Kuvychko, W.-D. Hunnius, K. Seppelt, S. H. Strauss, and O. V. Boltalina, *J. Phys. Chem. A*, 2004, **108**, 11449.
- 32 A. G. Avent, O. V. Boltalina, P. W. Fowler, A. Y. Lukonin, V. K. Pavlovich, J. P. B. Sandall, J. M. Street, and T. J. Taylor, *Chem. Soc., Perkin Trans. 2*, 1998, 1319.

- 33 G. A. Burley, A. G. Avent, I. V. Goldt, P. B. Hitchcock, H. Al-Matar, D. Paolucci, F. Paolucci, P. W. Fowler, A. Soncini, J. M. Street, and R. Taylor, *Org. Biomol. Chem.*, 2004, **2**, 319.
- 34 D. M. Cox, S. D. Cameron, A. Tuinman, A. Gakh, J. L. Adcock, R. N. Compton, E. W. Hagaman, K. Kniaz, J. E. Fischer, R. M. Strongin, M. A. Cichy, and A. B. Smith, *J. Am. Chem. Soc.*, 1994, **116**, 1115.
- 35 Relevant data demonstrating the β -deshielding effect: C-2 in adamantane at δ 38.4 vs. C-2 in 1-fluoroadamantane at δ 43.4; C-2 in bicyclo[2.2.1]heptane at δ 29.6 vs. C-2 in 1-fluorobicyclo[2.2.1]heptane at δ 32.03; (c) C-2 in bicyclo[3.3.1]nonane at δ 32.0 vs. C-2 in 1-fluorobicyclo[3.3.1]nonane at δ 37.3; (d) C-2 in bicyclo[2.2.2]octane at δ 25.9 vs. C-2 in 1-fluorobicyclo[2.2.2]octane at δ 31.0. The only example that we know of a β -shielding effect: C-8a in triptycene at δ 144.73 vs. C-8a in 9-fluorotriptycene at δ 143.36. See (a) Ref. 26. (b) Ref 27. (c) Ref 29. (d) Z. W. Qiu, D. M. Grant, and R. J. Pugmire, *J. Am. Chem. Soc.*, 1982, **104**, 2747.
- 36 (a) L. Margulès, J. Demaison, and J. E. Boggs. *J. Phys. Chem. A*, 1999, **103**, 7632. (b) D. R. Lide, Jr. and D. E. Mann, *J. Chem. Phys.*, 1958, **29**, 914. (c) R. L. Hilderbrandt and J. D. Wieser, *J. Mol. Struct.*, 1973, **15**, 27.
- 37 H. Bai, R. K. Harris, and H. Reuter. *J. Organomet. Chem.*, 1991, **408**, 167.
- 38 S.-F. Liu and K. Schmidt-Rohr, *Macromolecules*, 2001, **34**, 8416.
- 39 E. O. Stejskal, J. Schaefer, and J. S. Waugh. *J. Magn. Reson.*, 1977, **28**, 105.
- 40 S. L. Troyanov, P. A. Troshin, O. V. Boltalina, I. N. Ioffe, L. N. Sidorov, and E. Kemnitz. *Angew. Chem. Int. Ed.*, 2001, **40**, 2285.
- 41 V. I. Privalov, O. V. Boltalina, N. A. Galeva, and R. Taylor. *Dokl. Phys. Chem.*, 1998, **360**, 182.

- 42 W. W. Fleming, C. A. Fyfe, J. R. Lyerla, H. Vanni, and C. S. Yannoni, *Macromolecules*, 1980, **13**, 460.
- 43 M. Ernst, A. Samoson, and B. H. Meier, *Chem. Phys. Lett.*, 2001, **348**, 293.
- 44 M. Ernst, A. Verhoeven, and B. H. Meier, *J. Magn. Reson.*, 1998, **130**, 176.
- 45 M. Ernst, H. Zimmermann, and B. H. Meier, *Chem. Phys. Lett.*, 2000, **317**, 581.
- 46 Y. S. Lee, T. H. Cho, B. K. Lee, J. S. Rho, K. H. An, and Y. H. Lee, *J. Fluorine Chem.*, 2003, **120**, 99.

Chapter 6

³¹P NMR Characterization of the Nanocluster



Introduction

The vapor growth of SWNTs from catalyst particles occurs by a general vapor-liquid-solid (VLS) growth mechanism.¹ The growth of SWNTs by VLS is believed to occur via two mechanistic steps: nucleation and growth.^{2,3} Nucleation involves both the formation of a catalyst particle and the initial construction of the carbon framework on which the tube is later grown. At growth temperatures (800 - 1000 °C) the catalyst metal atoms aggregate to form a liquid metal nanoparticle. For the growth of SWNTs, it is proposed that the nanoparticle needs to be *ca.* 50 - 200 metal atoms (1 - 100 nm).⁴ The metals most commonly used for SWNT growth are iron, cobalt, nickel, molybdenum, and various bimetallic alloys of these metals.⁵ Iron species, such as iron oxides,⁶ iron nitrates,⁷ Fe(CO)₅,⁸ and ferrocene,⁹ have been reported as active catalysts. Irrespective of the iron source, the overall goal has been to form a nanoparticle less than 100 nm. In a recent publication, Liu and co-workers¹⁰ have reported the growth of SWNTs using the iron-molybdenum nanocluster $[\text{H}_x\text{PMo}_{12}\text{O}_{40}\text{cH}_4\text{Mo}_{72}\text{Fe}_{30}(\text{O}_2\text{CMe})_{15}\text{O}_{254}(\text{H}_2\text{O})_{98}]$ (FeMoC), originally reported by Müller and co-workers.¹¹ The structure of FeMoC (Figure 6.1) consists of a tetrahedral reduced Keggin $[\text{H}_x\text{PMo}_{12}\text{O}_{40}]^{3-}$ ion inside a spherical icosahedral giant (Keplerate) cage of the $\{(\text{Mo}^{\text{VI}})\text{Mo}^{\text{VI}}_5\}_{12}\text{Fe}^{\text{III}}_{30}$ type. It was proposed that the individual FeMoC molecules, rather than aggregates, behave as catalyst precursors for the growth of SWNTs. If this is true, then this result offers hope of designing particular molecular precursors to SWNT catalysts.

The as-published synthesis of FeMoC has a low yield (4%)¹¹ and there appears uncertainty as to the color as well as its solubility and/or stability in water.^{10,11} Initial studies in this work confirmed the variability in the color and analytical purity, prompting

a detailed study of the synthesis and the development of appropriate purification procedures and a study of the ^{31}P NMR spectra to better understand the magnetic environment of the central P atom in the FeMoC structure.

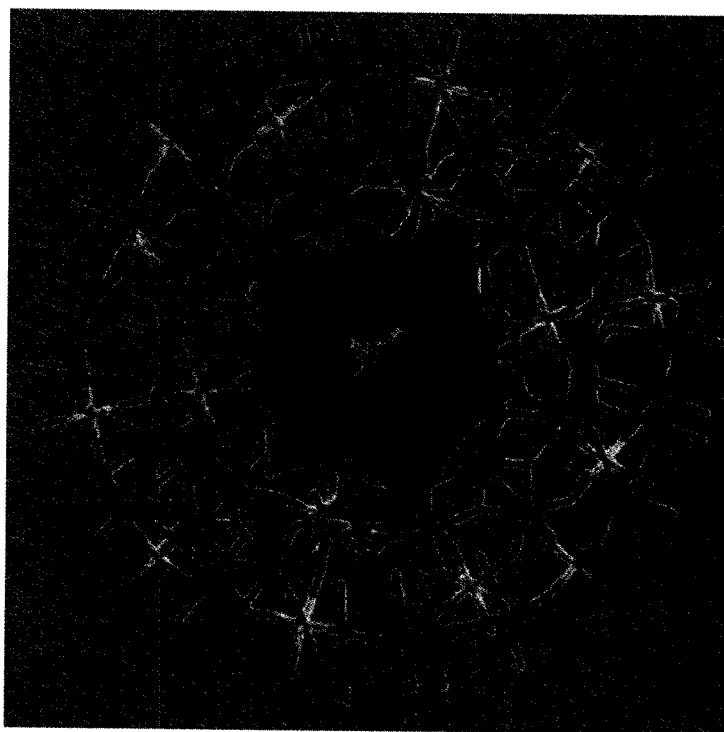


Figure 6.1. Computer representation of FeMoC based upon single crystal data showing the ‘cluster-within-a-cage’ structure. The central Keggin ion is shown in green, the molybdenum atoms of the Keplerate cage are shown in blue, iron atoms are in yellow and oxygen atoms in red.

Results and Discussion

The reported synthesis of FeMoC involves the addition of $\text{H}_3[\text{P}(\text{Mo}_3\text{O}_{10})_4]$ to a pre-made aqueous mixture of FeCl_2 , Na_2MoO_4 , and MeCO_2H . The reaction mixture is acidified and allowed to react for 45 minutes, after which time any insoluble material is removed by filtration. The filtrate is allowed to evaporate to yield crystals of FeMoC.¹¹ Following this procedure does indeed yield a dark crystalline material; however, it was found to have inconsistent and irreproducible analysis and spectroscopy suggesting that a

mixture of materials co-crystallizes.¹² Furthermore, addition of cold H₂O yields a blue solution and a yellow-green insoluble material. UV-visible spectroscopy of the H₂O soluble blue fraction does not show any of the characteristic nucleus shell charge transfer bands between the host and the Keggin guest (550 nm) observed previously for the FeMoC structure.¹¹ Instead it shows a broad band at 723 nm. The ATR spectrum of the blue product does not show any of the peaks associated with FeMoC or the Keplerate cage.¹¹

The yellow-green solid is only slightly soluble in H₂O but does give the required band at 550 nm in the UV-visible spectrum, albeit weakly.¹² Investigation of the solubility of the yellow-green solid in a variety of solvents shows that a dark green solution is formed in EtOH with a pale yellow residue remaining. Analysis of each of these fractions indicates that the dark green product formed after washing with cold H₂O and extraction with EtOH is consistent with the spectroscopy associated with the single crystal molecular structure previously reported for FeMoC.¹¹

Based upon XPS, UV-visible, and ATR spectroscopic analysis, the residual yellow solid remaining in the filter appears to be the Keplerate cage without the Keggin template as indicated by the lack of ³¹P NMR signal.¹² The UV-visible spectrum of a genuine sample of the Keplerate¹³ is very similar to the spectrum of the yellow solid from the filter. The XPS analysis of the yellow residue from the synthesis shows a Fe:Mo:C ratio is 30:69:25 that is similar to an authentic sample of the Keplerate cage (30:72:24).¹²

The apparently low solubility of FeMoC, and insolubility of the yellow product (Keplerate cage), allows for the reactive-purification of FeMoC by washing the crude product with cold H₂O followed by the Soxhlet extraction of the residue with EtOH resulting in ligand exchange.¹² This route produces a saturated solution of FeMoC in EtOH; that may be evaporated to yield a dark green solid. Although spectroscopically identical to the previous reports, the TGA and MS of the green product show the presence of coordinated EtOH. Thus, the green material obtained from Soxhlet extraction has the

formula $[H_xPMo_{12}O_{40}\subset H_4Mo_{72}Fe_{30}(O_2CMe)_{15}O_{254}(H_2O)_{98-x}(EtOH)_x]$ where x is calculated to be *ca.* 30.¹² The AFM of FeMoC-EtOH spin-coated onto mica shows individual nanoparticles with a height of 2 nm. The theoretical diameter of FeMoC (based upon the X-ray crystal structure) is 2.1 nm. The UV-visible spectrum of purified FeMoC-EtOH shows bands reported previously to be characteristic of an intervalence $[Mo(V) \rightarrow Mo(VI)]$ charge transfer in the Keggin cluster (880 and 1045 nm) and the nucleus shell charge transfer between the host and the Keggin guest (550 nm).¹²

The XPS analysis of FeMoC-EtOH (Table 6.1) shows a Fe:Mo ratio (1:2.7) consistent with the formulation of the encapsulated molybdate ion in the supramolecular cage (calculated = 1:2.8). The calculated concentration of phosphorus is slightly high, however, the low intensity of the P 2p peak (and hence the poor signal to noise) makes quantification difficult. There are signals within the C1s and O1s that correspond to the C-O portion of the acetates with an O:C ratio of *ca.* 1.5 (as compared to the theoretical value of 2.0). Furthermore, the carbon content is consistent with the substitution of coordinated water for EtOH ligands.

Table 6.1. XPS elemental ratio analysis for the products from FeMoC synthesis.¹²

Elemental Ratio	Fe	Mo	P	O	C
FeMoC (Calcd.)	30	84	1	422	30
FeMoC-EtOH (Exp.)	30	79.5	<3 ^a	316	68.0
FeMoC(EtOH) ₃₀ (Calcd.)	30	84	1	422	60
Yellow residue (Exp.)	30	68.5	0	222	24.6
Keplerate (Calcd.)	30	72	0	382	24

^a Exact atomic ratio difficult to determine due to low signal to noise.

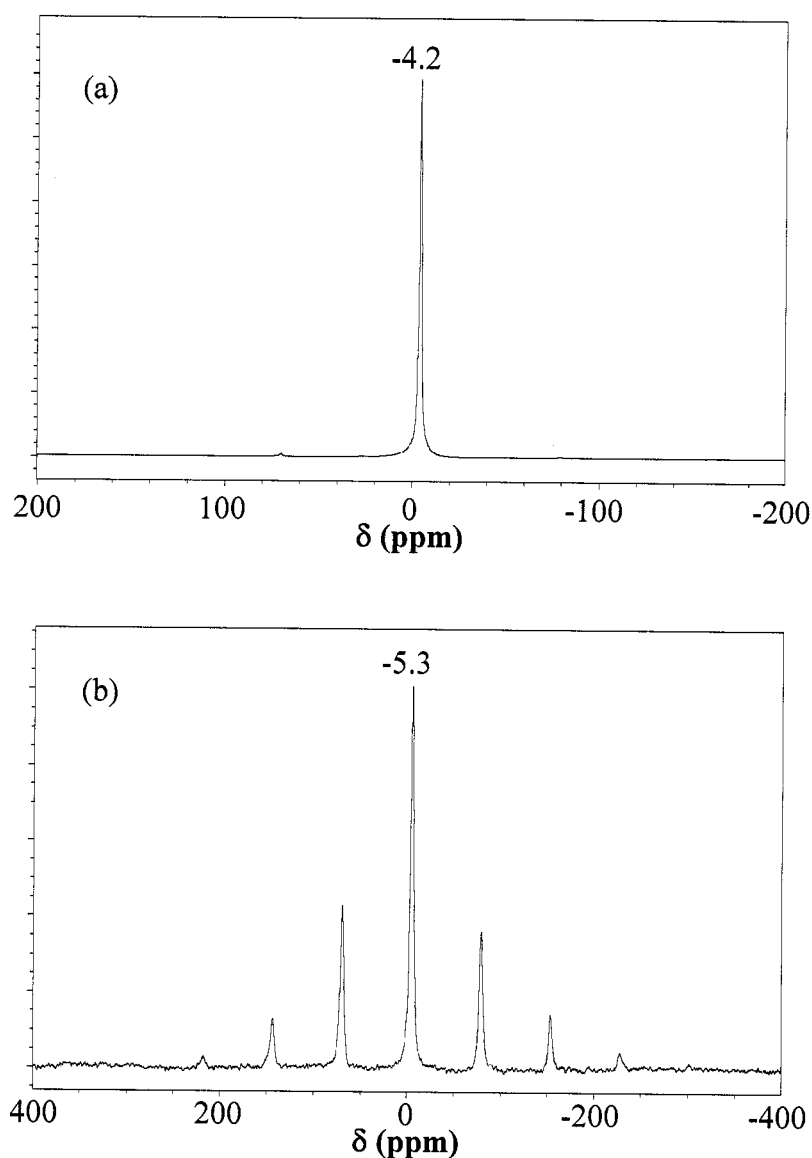


Figure 6.2. ^{31}P NMR spectra of (a) $\text{H}_3[\text{P}(\text{Mo}_3\text{O}_{10})_4]$ and (b) FeMoC-EtOH .

Müller and co-workers have previously reported¹¹ that FeMoC is a highly paramagnetic cluster containing 150 unpaired electrons associated with 30 octahedral high-spin d^5 Fe^{3+} centers. Our ability to prepare purified samples of FeMoC (albeit with EtOH associated with the Fe^{3+} centers instead of H_2O) prompted an investigation of the

^{31}P NMR spectrum of FeMoC-EtOH since the shift and relaxation of the ^{31}P nucleus can be uniquely influenced by the 30 paramagnetic centers positioned in a spherical manner at

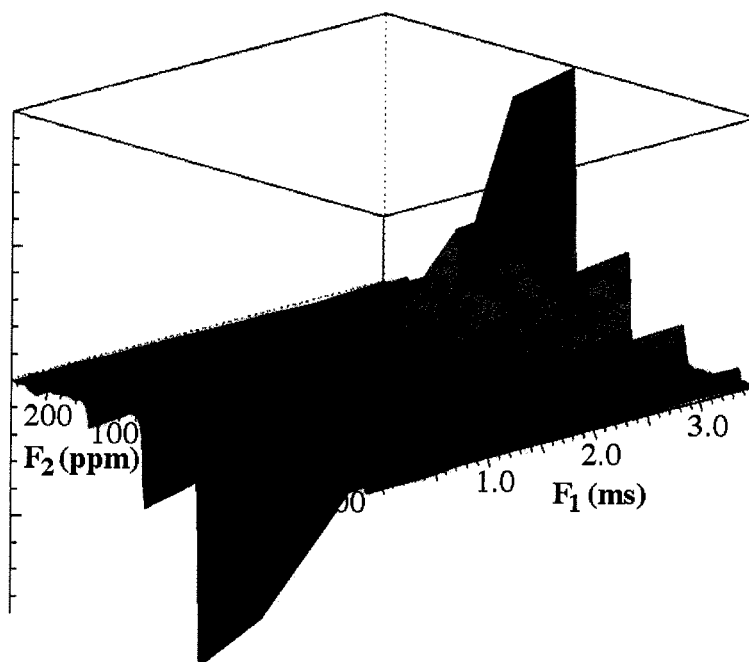


Figure 6.3. Pseudo-2D inversion recovery data set for ^{31}P NMR of FeMoC-EtOH.

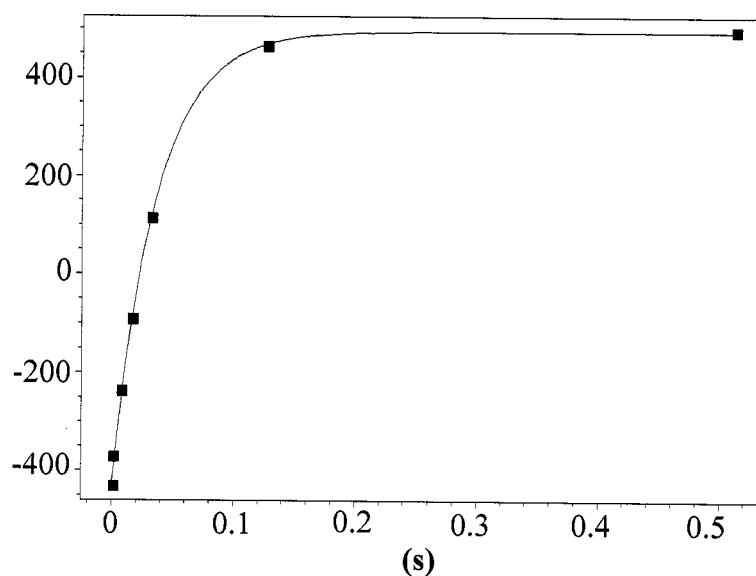


Figure 6.4. The height of the center band ($\delta = -5.5$ ppm) for the ^{31}P NMR spectrum of FeMoC-EtOH versus τ ($T_1 = 35$ ms).

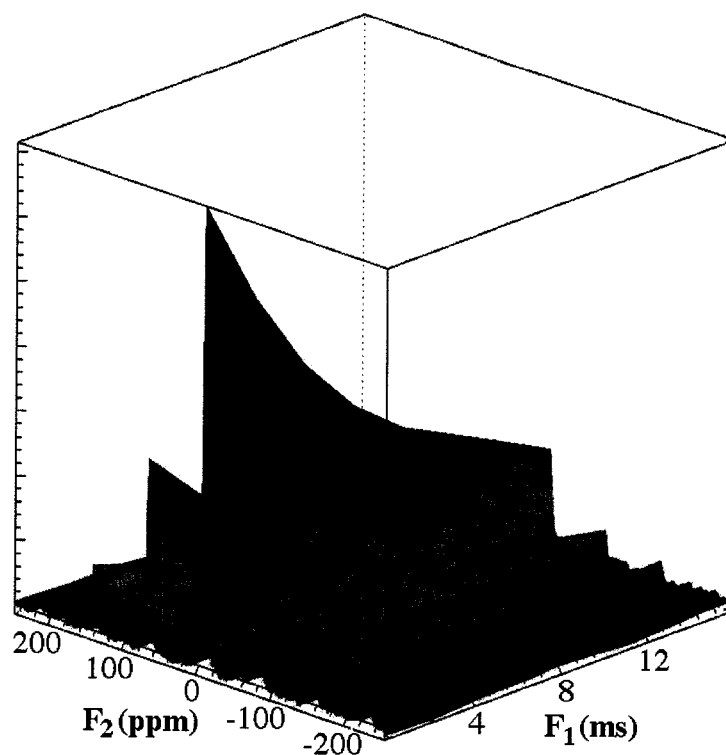


Figure 6.5. Pseudo 2D CPMG data set (T_2 isolation by spin echo) for FeMoC-EtOH.

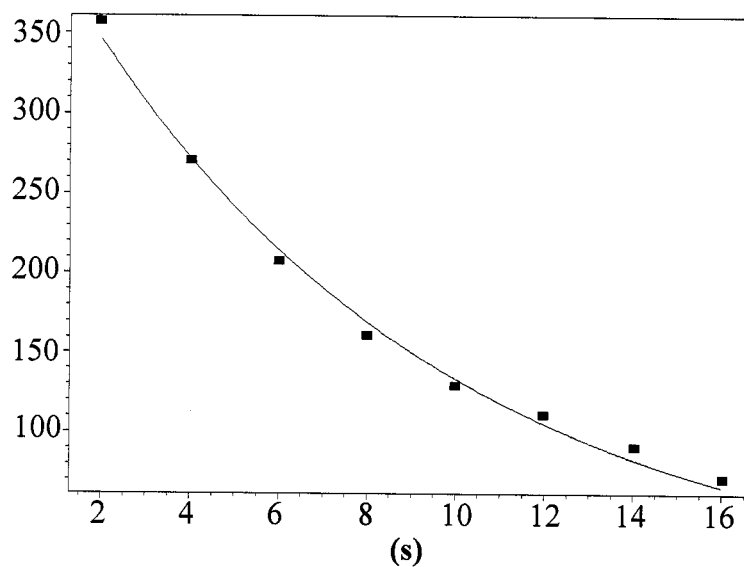


Figure 6.6. The height of the center band ($\delta = -5.5$ ppm) for the ^{31}P NMR spectrum of FeMoC-EtOH versus τ ($T_2 = 8$ ms).

a distance of *ca.* 10 Å. The solid state ^{31}P NMR spectrum for FeMoC-EtOH is shown in Figure 6.2 along with the spectrum of $\text{H}_3[\text{P}(\text{Mo}_3\text{O}_{10})_4]$ for comparison. The spectrum of $\text{H}_3[\text{P}(\text{Mo}_3\text{O}_{10})_4]$ (Figure 6.2a) shows a single resonance at $\delta = -4.2$ ppm typical of PO_4 coordination environment.^{14,15,16} The chemical shift for FeMoC-EtOH ($\delta = -5.3$ ppm) is close to that of $\text{H}_3[\text{P}(\text{Mo}_3\text{O}_{10})_4]$ suggesting little effect of the paramagnetic Fe^{3+} centers in the Keplerate cage on the Keggin ion's phosphorous. However, we note that the spectrum for FeMoC-EtOH (Figure 6.2b) shows a higher chemical shift anisotropy (the asymmetry parameter is near 1 indicating an extremely symmetric environment), which suggests that the Keggin ion is located centrally within the Keplerate cage.

Figure 6.3 shows a pseudo 2D data set resulting from the application of the inversion recovery sequence. From this data we obtain the plot in Figure 6.4, which is the intensity of the center band versus τ , and subsequently the T_1 (35 ms). Phosphates generally have T_1 in the range of 0.1 – 10 seconds.¹⁷ We propose the major contribution to the shorter T_1 in FeMoC-EtOH is the paramagnetism of the Fe^{3+} centers in the Keplerate cage. But the fact that we can see one at all suggests that their influence is not overwhelming. The T_2 for FeMoC-EtOH is obtained from a pseudo 2D CPMG data set (T_2 isolation by spin echo), shown in Figures 6.5 and 6.6. The calculated T_2 (8 ms) is within the normal range for phosphates in the solid state.¹⁸ The solid state ^{31}P NMR data is consistent with a weak interaction between the central phosphorus and the surrounding Keplerate cage.

Experimental

Solvents were purchased from Fisher Scientific and used as received. FeCl_2 , Na_2MoO_4 , and $\text{HPMo}_{12}\text{O}_{40}$ were obtained from commercial vendors (Sigma-Aldrich) and stored in a desiccator prior to use. All organic reagents (Aldrich, TCI America, Alfa Aesar) and solvents (Fisher Scientific) were used as received. Keplerate synthesis was

accomplished using a modification of the literature method.^{14,19} The synthesis of FeMoC was carried out by a modification of the literature reported method.¹²

Solid state ^{31}P CPMAS NMR spectra were collected on a Bruker Avance 200 spectrometer at 81 MHz. Samples were measured using a 7 mm extended VT MAS probe with 7 mm long-barrel ZrO_2 rotors and plugs and Kel-F fluoropolymer caps. Chemical shifts were referred to the $\text{NH}_4[\text{H}_2\text{PO}_4]$ ($\delta = 0.8$ ppm) by sample replacement. All the spectra were collected with high power ^1H decoupling. Spectra were acquired using a 90° pulse of $3.5\ \mu\text{s}$ and a spectral width of 149,253 Hz. Bloch decay spectra were collected at a spinning speed of 6.00 kHz for 20480 scans with power-gated high-power ^1H decoupling over a spectral width of 150 kHz. Measurement conditions for FeMoC as follows: spinning frequency, 6 kHz; pulse repetition time, 150 ms; number of points, 4,462 (1D), 14,910 (T_1 IR), 2,970 (T_2 CPMG); number of scans, 20k. Measurement conditions for $\text{H}_3[\text{P}(\text{Mo}_3\text{O}_{10})_4]$ as follows: spinning frequency, 6 kHz; pulse repetition time, 30 s; number of points, 14,910; number of scans, 1992. T_1 relaxation times were measured via the standard inversion recovery method with power-gated high-power ^1H decoupling where appropriate for 8000 scans. Values of τ were selected initially by a telescoping series of values ranging from 1 ms to 1 s. T_2 relaxation times were measured via the Carr-Purcell-Meiboom-Gill (CPMG) spin-echo decay method with power-gated high-power ^1H decoupling and an echo decay time 2τ of 1 ms per echo iteration for 8000 scans.

References

- ¹ E. F. Kukovitsky, S. G. L'vov, and N. A. Sainov, *Chem. Phys. Lett.*, 2000, **317**, 65.

- 2 J. Gavillet, A. Loiseau, F. Ducastelle, S. Thair, P. Bernier, O. Stéphan, J. Thibault, and J. -C., Charlier, *Carbon*, 2002, **40**, 1649.
- 3 A. Gorbunov, O. Jost, W. Pompe, and A. Graff, *Carbon*, 2002, **40**, 113.
- 4 F. Ding, A. Rosén, and K. Bolton, *J. Chem. Phys.*, 2004, **121**, 2775.
- 5 F. Banhart, N. Grobert, M. Terrones, J. -C. Charlier, and P. M. Ajayan, *Int. J. Mod. Phys. B*, 2001, **15**, 4037.
- 6 H. Ago, K. Nakamura, N. Uehara, and M. Tsuji, *J. Phys. Chem. B*, 2004, **108**, 18908.
- 7 S. C. Lyu, B. C. Liu, S. H. Lee, C. Y. Park, H. K. Kang, C. W. Yang, and C. J. Lee, *J. Phys. Chem. B*, 2004, **108**, 1613.
- 8 P. Nikolaev, M. J. Bronikowski, R. K. Bradley, F. Rohmund, D. T. Colbert, K. A. Smith, and R. E. Smalley, *Chem. Phys. Lett.*, 1999, **313**, 91.
- 9 H. M. Cheng, F. Li, G. Su, H. Y. Pan, L. L. He, X. Sun, and M. S. Dresselhaus, *Appl. Phys. Lett.*, 1998, **72**, 3282.
- 10 L. An, J. M. Owens, L. E. McNeil, and J. Liu, *J. Am. Chem. Soc.*, 2002, **124**, 13688.
- 11 A. Müller, S. K. Das, P. Kögerler, H. Bögge, M. Schmidtman, A. X. Trautwein, V. Schünemann, E. Krickemeyer, and W. Preetz, *Angew. Chem. Int. Ed.*, 2000, **39**, 3414.
- 12 R. E. Anderson, R. Colorado, Jr., C. Crouse, D. Ogrin, B. Maruyama, M. J. Pender, C. L. Edwards, E. Whitsitt, V. C. Moore, D. Koveal, C. Lupu M. Stewart, J. M. Tour, R. E. Smalley, and A. R. Barron, *Dalton Trans.*, 2006, 3097.
- 13 A. Müller, S. Sakar, S. Q. N. Shah, H. Bögge, M. Schmidtman, S. Sakar, P. Kögerler, B. Hauptfleisch, A. X. Trautwein, and V. Schünemann, *Angew. Chem. Int. Ed.*, 1999, **38**, 3238.

- 14 B. C. Tischendorf, D. J. Harris, J. U. Otaigbe, and T. M. Alam, *Chem. Mater.*, 2002, **14**, 341.
- 15 M. Witschas and H. Eckert, *J. Phys. Chem. A*, 1999, **103**, 10764.
- 16 L. B. Moran, J. K. Berkowitz, and J. P. Yesinowski, *Phys. Rev. B*, 1992, **45**, 5347.
- 17 W. T. Beaudry, G. W. Wagner, and J. R. Ward, *J. Mol. Catal.*, 1994, **93**, 221.
- 18 C. Mercier, L. Montagne, H. Sfihi, G. Palavit, J. C. Boivin, and A. P. Legrand, *J. Non-Cryst. Solids*, 1998, **224**, 163.
- 19 A. Müller, E. Krickemeyer, H. Bögge, M. Schmidtman, and F. Peters, *Angew. Chem. Int. Ed.*, 1998, **37**, 3360.